ISTANBUL TECHNICAL UNIVERSITY ★ GRADUATE SCHOOL OF SCIENCE ENGINEERING AND TECHNOLOGY

A NUMERICAL SIMULATION STUDY OF THE PRESSURE BEHAVIOR OF A VERTICAL WELL IN A DRY GAS RESERVOIR

M.Sc. THESIS

Cihan ALAN

Department of Petroleum and Natural Gas Engineering

Petroleum and Natural Gas Engineering Programme

JANUARY 2012

ISTANBUL TECHNICAL UNIVERSITY ★ GRADUATE SCHOOL OF SCIENCE ENGINEERING AND TECHNOLOGY

A NUMERICAL SIMULATION STUDY OF THE PRESSURE BEHAVIOR OF A VERTICAL WELL IN A DRY GAS RESERVOIR

M.Sc. THESIS

Cihan ALAN
(505101502)

Department of Petroleum and Natural Gas Engineering

Petroleum and Natural Gas Engineering Programme

Thesis Advisors: Prof. Dr. Mustafa ONUR and Yrd. Doç. Dr. Ö. İnanç TÜREYEN

JANUARY 2012

İSTANBUL TEKNİK ÜNİVERSİTESİ ★ FEN BİLİMLERİ ENSTİTÜSÜ

KURU BİR GAZ REZERVUARLARINDAKİ DİK BİR KUYUNUN BASINÇ DAVRANIŞININ SAYISAL SİMÜLASYON ÇALIŞMASI

YÜKSEK LİSANS TEZİ

Cihan ALAN
(505101502)

Petrol ve Doğal Gaz Mühendisliği Anabilim Dalı

Petrol ve Doğal Gaz Mühendisliği Programı

Tez Danışmanları: Prof. Dr. Mustafa ONUR ve Yrd. Doç. Dr. Ö. İnanç TÜREYEN

OCAK 2012

Cihan Alan, a **M.Sc.** student of ITU **Graduate School of Science Engineering and Technology** student ID **505101502**, successfully defended the thesis entitled "A NUMERICAL SIMULATION STUDY OF THE PRESSURE BEHAVIOR OF A VERTICAL WELL IN A DRY GAS RESERVOIR", which he prepared after fulfilling the requirements specified in the associated legislations, before the jury whose signatures are below.

Thesis Advisor :	**Prof. Dr. Mustafa ONUR** İstanbul Technical University	.....
Co-advisor :	**Assist. Prof. Dr. Ö. İnanç TÜREYEN** İstanbul Technical University	.....
Jury Members :	**Assoc. Prof. Dr. Ahmet SİRKECİOĞLU** İstanbul Technical University	.....
	Assist. Prof. Dr. Şenol YAMANLAR İstanbul Technical University	.....

Date of Submission : 19 December 2011
Date of Defense : 24 January 2012

To my fiancée,

FOREWORD

I am greatly thankful to my advisors Prof. Dr. Mustafa Onur and Yrd. Doç. Dr. Ö. İnanç Türeyen for their guidance, encouragement, patience and endless supports.

January 2012

Cihan ALAN
Research Asistant, İTÜ

TABLE OF CONTENTS

Page

ABBREVIATIONS

FIT	**:** Functional Iteration Technique
NW	**:** Newton's Method
DST	**:** Drill Stem Testing
WBS	**:** Wellbore Storage
DD	**:** Drawdown Period
BU	**:** Buildup Period
IPTT	**:** Interval Pressure Transient Test
GUI	**:** Graphical User Interface
PDE	**:** Partial Differential Equation

LIST OF SYMBOLS (NOMENCLATURE)

A	: Surface area, ft^2
B	**:** Formation volume factor, RB/STB
D	**:** Non-Darcy Flow Coefficient, $MSCF/D^{-1}$
c_g	**:** Compressibility of gas, psi^{-1}
c_r	**:** Compressibility of rock, psi^{-1}
f	**:** Given function
f'	**:** Derivative of given function
J	**:** Jacobian matrix
k	**:** Permeability, md
p	**:** Pressure, psi
q	**:** Flow rate, STB/D
r	**:** Radial direction
z	**:** Vertical direction
Z	**:** *Z*-factor
S	**:** Skin factor
S_t	**:** Total skin
T	**:** Transmissibility, $md \times ft/cp$
V	**:** Constant related to fluid volume of a grid block.
t	**:** Time, day
Vp	**:** Bulk volume, ft^3

Greek Symbols

Δ	**:** Difference operator
δ	**:** Non-Darcy correction factor
ε	**:** Tolerence limit
ϕ	**:** Porosity
θ	**:** Theta direction
μ	**:** Viscosity, cp
v	**:** Velocity, ft/s
γ_g	**:** Specific gravity
γ	**:** A term in non-Darcy correction factor gravity
ρ	**:** Density, lbm/ft^3
h_s	**:** Perturbation
∂	**:** Derivative operator

Subscripts

r	**:** radial direction
z	**:** vertical direction
i	**:** Index for radial direction
j	**:** Index for vertical direction
wf	**:** Wellbore flowing

Superscripts

n	**:** Old time level
$n+1$	**:** Present time level

LIST OF TABLES

Page

LIST OF FIGURES

Page

A NUMERICAL STUDY OF THE PRESSURE BEHAVIOR OF A VERTICAL WELL IN A DRY GAS RESERVOIR

SUMMARY

Predicting production performance of a dry gas reservoir for reservoir management acquires understanding the behavior of pressure transients and fluid distribution over both space and time. In recent years, reservoir simulators have been extensively used to build various reservoir and well models to investigate and visualize the process under a series of potential scenarios, such as drilling new wells and injecting fluids.

The objective of this project is to develop and present applications of a two-dimensional (2-D) *r-z*, fully implicit, single-phase, real gas simulation model with a single well located at the center of a cylindrical reservoir. The mathematical formulation is described in detail with wellbore storage, skin and non-Darcy flow effects firstly, and then it is followed by an extensive verification of the simulator developed in this project with a well-known well test analysis software in order to perform a number of real field applications such as standard and routine tests of natural gas industry (i.e., flow-after-flow, isochronal and modified isochronal tests) for both partially and fully penetrated wells either in a single or multilayered systems. The simulator is also capable of conducting a packer-probe test called as Mini-Drill Stem Test (MiniDST) for estimation of reservoir properties such as permeability, skin, etc. The effect of non-Darcy flow on pressure solutions at the tested well as well as throughout the reservoir for the entire flow rate history is also investigated in a different manner than described in mathematical formulation such that the a non-Darcy flow area in radial direction is introduced and restricted to a region of a specific radius which is concentric with wellbore.

As the problem is non-linear, solving pressures at each gridblock at a specific time may require more than one iteration. Since two different methods called as functional iteration and Newton's methods are applicable to solve such systems, they are analyzed, verified using at least two different solvers with respect to accuracy and speed.

With the great help of user friendly interface in windows, numerous useful tips are available such as graphical outputs for pressure responses or well test analysis purposes, creating non-uniform grids on vertical axis, viewing heterogeneous porosity and permeability distributions after putting heterogeneous distributions of permeability, porosity as well as skin and non-Darcy flow coefficient in the radial direction (at the gridblocks adjacent to the wellbore) manually as input. It is also very easy to generate and investigate the consequences of various injection and production scenarios. Using such a simulation tool proves useful to have a better insight into how pressure transients move around in a reservoir due to production and/or injection of a single well located at the center of the cylindrical reservoir. In addition to logarithmically sampled time step selection algorithm, an automatic time step selection algorithm has also been implemented so that the simulator can accurately simulate fast changes in pressure by allowing shorter time steps automatically to be

taken in simulation. The simulator is coded in Visual Basic .NET which allows object oriented programming and working on a windows friendly interface. The interface is also capable of visualizing pressure distributions over space and time. Several example reservoirs are considered for demonstrating the utility of the developed simulator and the interface coupled with GUI which may enable one to conduct visual studies of well pressure transients in homogeneous reservoirs as well as heterogeneous reservoirs.

KURU BİR GAZ REZERVUARINDAKİ DİK BİR KUYUNUN BASINÇ DAVRANIŞININ SAYISAL SİMÜLASYON ÇALIŞMASI

ÖZET

Bir petrol rezervuarının, rezervuar yönetimi için üretim performansı tahmini, basınç ve akışkan dağılımlarının zaman ve pozisyona bağlı olarak davranışlarını anlamayı gerektirir. Son yıllarda rezervuar simülatörleri kapsamlı kullanılmasıyla, çok sayıda rezervuar modelleri oluşturularak bu süreç değişik koşullarda incelenmek ve görsel olarak canlandırılmaktadır.

Rezervuar simulasyonu, fizik, matematik, rezervuar mühendisliği ve bilgisayar programlama branşlarını birleştirerek, çok çeşitli çalışma koşulları altında rezervuar performansını tahmin edebilecek bir araç geliştirmeyi esas alır. Sayısal rezervuar simulatörleri yaygın ve öncelikli olarak kullanılır, çünkü herhangi başka bir yol ile çözülemeyecek problemleri çözebilirler. Daha hızlı ucuz ve güvenilir sonuçlar elde edebildiğimiz için basit problemleri bile sayısal rezervuar simülatörleri yardımıyla çözmek çoğu zaman en iyi yol olarak görülebilir.

Günümüzde, gelişmiş rezervuar simülatörleri, üretim planlaması tahmini ve çeşitli kararların vermesi gibi amaçlar için endüstride önde gelen petrol şirketleri tarafından kullanılıyor. Modern simülatörlerin güvenilirliği ve bilgisayarların her zaman her yerde mevcut ve kullanıma hazır olması, rezervuarların büyüklüğüne bakılmaksızın günlük planlama ve karar verme amaçları için rezervuar simülasyonu kullanımını pratik yapmaktadır. Hem olgun ve hem de geliştirme aşamasında olan sahalar için uygulanan çok çeşitli senaryolar, simülatörlerin kullanımını rezervuar mühendisliğinin kaçınılmaz bir parçası haline getirmiştir. Şu anda, tüm dünyada rezervuar mühendisleri güvenle rezervuar yönetimi, saha tanımı, rezervuar karakterizasyonu ve fiziksel yorumlama amaçları için sayısal simülatörleri kullanmaktadır.

Bu çalışmanın amacı, iki boyutlu (*r*-*z*), sayısal, tamamıyle implicit, tek fazda, gerçek gaz ve silindir bir rezervuarın merkezinde tek kuyuya sahip modeller geliştirmektir. Öncelikle kuyu içi depolaması, zar faktörü ve Darcy olmayan akışı içeren

matematiksel formülasyon detaylı bir şekilde tanımlanmıştır. Daha sonra bu projede geliştirilen simulatör sonuçlarının endüstride çok iyi bilinen bir kuyu testi analiz yazılımı ile kıyaslanması ve doğruluğununun kapsamlı bir şekilde teyit edilmesi amacıyla doğal gaz endüstrisinin standart ve rutin testleri (akış üstüne akış, isochronal ve düzeltilmiş isochronal gibi) kısmi ve tamamen tamanlanmış bir kuyu için tek ya da tabakalı rezervuar sistemlerinde uygulanmıştır. Ayrıca simulator geçirgenlik, zar faktörü gibi rezervuar parametlerinin tahminini sağlayan packer-probe (MiniDST) testlerinin modellenmesi ve uygulanması kapasitesine de sahiptir. Tüm akış boyunca kuyu dibindeki ve ayrıca rezervuarın tüm noktalarındaki basınç çözümleri üzerinde Darcy olmayan akışın etkisi matematik formülasyonda tanımlanandan farklı bir yöntemle araştırılmıştır. Bu yöntem Radyal eksende Darcy olmayan bir akış alanı oluşturularak, bu alanın kuyuyla ortak merkezli belirli bir yarıçapa kadar sınırlandığı varsayılmıştır.

Her bir hücredeki basıncı belirli bir zamanda çözümlemek, lineer olmayan bu problem için birden fazla yineleme (iterasyon) gerektirebilir. Bu tür sistemlerin çözümünü sağlayabilen foksiyonel iterasyon yöntemi ve Newton yöntemi analiz edilerek sonuçların en az iki farklı matriks çözücü yardımıyla duyarlılık ve hız özellikleri dikkate alınarak teyit edilmesi gerçekleştirilmiştir.

Grafiksel arayüz, basınç dağılımlarının görsel olarak çalışılmasını sağlayarak, davranışlara klavuzluk eder. Bu şekilde geliştirilmiş bir simülasyon aleti, basıncın sistem içerisindeki değişiminin, bir üretim ya da injeksiyon kuyusuyla, rezervuar parametlerinin değişimiyle, heterojen ya da homojen geçirgenlik ve gözeneklilik dağılımlarıyla, birden fazla gözlem probe'larıyla olan bağlantısını daha iyi kavramaya yardımcı olur. Simülatör, kendi üretim stratejisine sahip birden çok üretim ya da injeksiyon senaryosuyla rezervuar sistemini modelleyerek, kuyu dibi basınçlarını her bir hücrede çözer. Logaritmik olarak artan zaman adımını seçen bir algoritmaya ek olarak ayrıca otomatik zaman adımı seçimini sağlayan bir algoritma geliştirilerek, basınçtaki hızlı değişimlerin bu adımların daha küçük atılması sağlanarak modellenir. Kullanıcının gözeneklilik ve geçirgenlik için heterojen dağılımlar oluşturulmasına imkan sağlanır. Simülatör, nesne yönelimli programlamayı ve arayüz oluşturmayı temel alan Visual Basic .NET'te kodlanmıştır. Düşey eksende düzenli olmayan gridlerin oluşturulması, gözeneklilik, geçirgenlik ve basınç dağılımları ile üretim stratejilerinin kaydedilmesi, yeniden yüklenmesi ve bu

parametrelerin grafiksel analizlerini gerçekleştirmek amacıyla iki boyutlu gösterimlerinin sunulması simülatörün diğer özelliklerindendir. Birçok örnek rezervuar simülasyon modelleri göz önüne alınarak, simülatörün ve arayüzün yararları gösterilmiştir.

1. INTRODUCTION

Reservoir simulation combines physics, mathematics, reservoir engineering, and computer programming to develop a tool for predicting hydrocarbon – reservoir performance under various operating conditions (Aziz and Settari, 1979). Numerical reservoir simulators are used widely, primarily because they can solve problems that cannot be solved in any other way. Usefulness of numerical models extends beyond solving difficult problems; even on simple problems, simulation is often the best solution method because it may be faster, cheaper, or more reliable that other methods (Onur, 1997).

In the last 30 years, reservoir simulation has evolved from a research area into one of the most flexible and widely used tools in reservoir engineering (Mattax and Dalton, 1990). Reservoir simulation has been extensively improved parallel to the development and enhancement in computer technology in the recent years. Modern reservoir simulators based on mathematical models are able to integrate spatially varying geologic descriptions, physical laws governing mass transport and phase behavior, well locations and constrains and many other factors (Ertekin et al. 2001).

Nowadays, advanced reservoir simulators are used by leading oil companies for management planning, production forecasting and decision making. The reliability of modern simulators and the fact that computers are always available and ready to use makes simulation practical to use on all sizes of reservoirs for daily planning and decision making. Application of such simulators to both mature and development stage fields became an inevitable part of reservoir engineering. Currently, reservoir engineers all over the world use numerical simulators with confidence; for reservoir management, field description, reservoir characterization and physical interpretation (Onur, 1997).

1.1 Literature Review

The field of numerical reservoir simulation has become one of the fastest growing bodies of knowledge over the past two decades, because of the strong demand for reliable predictions of reservoir performance. The tremendous progress in electronic computing hardware and the significant improvement in methods of numerical analysis were two important factors in the achievements made in numerical models of reservoirs (Esmail, 1985).

Numerical models which may address problems occurring either from nonlinearities such as multiphase or non-Darcy flow or characterizing the complex reservoir and well geometries has become more and more popular than analytical models in reservoir simulation. First attempts of reservoir simulation contain only standard reservoir simulators with local grid refinement usually performed by engineers in the industry. It was followed by pre-conditioning of standard simulator using PEBI gridding in the first industrial project which takes place in the early 1990's. Subsequently, there are numerous technical groups working on numerical projects dedicated to reservoir simulation. In the latest years, there are big improvements in automatic unstructured grids with the use of faster computer technology which allows users to generate models in much shorter times and also without a strong background in simulation. Unstructured (Voronoi, PEBI) gridding is commonly replaced the Cartesian grids or finite elements in modern reservoir simulators and does not require any knowledge by the user to perform the successful simulation.

The objective of numerical simulation is to create models that deal with problems such as complex boundary configurations as well as easy problems for analytical models such as the early time responses and logarithmic sampling of the time scale. However, considering all concerns to obtain a solution in a numerical model reasonably close to the analytical model generally requires to have smaller time steps and more and more gridblocks close to the well or an open interval where pressure is expected to change rapidly.

The methods normally developed in numerical simulators with a single-phase slightly compressible fluid assumption can be considered linear. However, gas, as a single-phase fluid, is not slightly compressible and moreover, gas diffusion is not a linear process, although real gas pseudo-functions (pseudo-pressure and pseudo-time

transformations) were developed to linearize the problem (Al-Hussiany et al. 1966, Agarwal 1979).

A systematic study has been made of the application of the real gas pseudo-pressure $m(p)$ to short-time gas well testing. The $m(p)$ function can be used in real gas flow problems to account for the variation of viscosity and Z-factor with pressure. A mathematical model was solved numerically to generate solutions of various real gas flow problems (Wattenbarger, 1968).

A mathematical model formulated in cylindrical, (r-z), coordinates which can simulate either a single-phase gas reservoir or a two phase (gas and water) reservoir with the capability of including non-Darcy flow effects through Forschheimer equation has been presented in the literature (Bratvold, 1986). Furthermore, Ding (1986) and Reynolds et al. (1987) presented the analysis of constant rate drawdown data and subsequent buildup data for the cases where non-Darcy flow effects are important examined. These works have shown the effect and the correct evaluation of the viscosity term which appears in the non-Darcy flow term representing the additional increase in the pressure drop throughout the reservoir due to non-Darcy flow effects. On the other hand, Kabir (2006) suggests a two step approach based on multirate transient drawdown tests, followed or preceded by a buildup in order to estimate reservoir parameters that may be of interest.

1.2 Statement of The Problem

The main purpose of this thesis is to develop a numerical simulator that simulates pressure behavior of a vertical well under 2-D (r-z) flow in a dry gas reservoir.

During the course of this work, a numerical simulator based on a mathematical model which is formulated in cylindrical, (r-z), coordinates is developed to simulate the pressure behavior of a vertical well in a single-phase real gas reservoir where gravity effects are neglected. The simulator considers a single well located at the center of a cylindrical drainage region. The reservoir where the top and bottom boundaries are closed has a uniform thickness, h. The outer boundary is a closed or no-flow boundary. The permeability and porosity is assumed to be independent of pressure, and the flow in the reservoir is assumed to be isothermal. The non-Darcy flow effects through the Forschheimer equation can be included in the pressure

behavior of the well and the reservoir. As mentioned above, we consider the gas as is real gas and, therefore, the viscosity and real gas deviation factor (Z-factor) are computed by the Lee et al. and Dranchuk and Abu-Kassem correlations, respectively.

A finite wellbore volume may be included to approximate the effect of wellbore storage which is discussed in Chapter 2. A constant rate need to be specified at standard conditions (i.e., at the wellhead). A sequence of constant rates where a production period may be followed by a buildup (constant rate may be zero to represent buildup) may be simulated.

Model neglects gravity effects, but in the single-phase gas case, the consequences of neglecting gravity effects are negligible since the flow will be controlled primarily by gas mobility because gas viscosities are small. In addition, the densities of dry gases are small.

The generation of both the *r*-direction and *z*-direction grids is thoroughly discussed in Chapter 2. Unlimited numbers of layers can be simulated.

Properties such as skin, thickness of skin zone, turbulence factors (β in both the *r* and *z*-directions and in the skin zone) and thickness may vary from layer to layer whereas permeability and porosity may vary from grid block to grid block. Within each layer we may include several gridblocks of variable thickness in *z*-direction. Whether a layer is open to flow or not must be specified through the input data. An arbitrary section of the wellbore adjacent to the formation may be open to flow.

1.3 Scope of the Thesis

Firstly, the mathematical formulation used to develop the numerical simulator is described. This is followed by an extensive verification of the simulator with the well-known well test analysis software called as ECRIN in order to perform a number of real field applications such as standard and routine tests of natural gas industry (i.e., flow-after-flow, isochronal and modified isochronal tests) for both partially and fully penetrated wells either in a single or multilayered systems. In many oil and gas reservoirs, producing wells are completed as limited-entry wells; that is, only a portion of the zone is perforated. If the limited-entry is adjacent to top of the formation, then wells are usually called partially penetrating wells. Limited-entry or partial penetration completions are preferred due to many reasons, but the

most common one is to prevent or delay the intrusion of unwanted fluids (gas or water) into the wellbore. Limited-entry or partial penetration will cause performance which, if not properly evaluated, can be mistaken for formation damage and can lead to errors in the interpretation of well-test data (Bilhartz, 1977). Another real field application which may be coupled with the application case mentioned previously, called as packer-probe test is also described in the Chapter 4. Traditionally, different testing procedures like flow-after-flow, isochronal and modified isochronal tests are used to estimate parameters required to provide deliverability estimates of gas wells and reservoirs. The turbulent or non-Darcy flow effects close to the wellbore, which appear as rate-dependent or non-Darcy skin, requires gas wells to be tested at a number of rates with the above mentioned tests so as to be able to estimate the non-Darcy flow coefficient by separating the mechanical skin component from the total skin factor (Horne and Kuchuk, 1988). The non-Darcy flow effect on wellbore pressure as well as throughout the reservoir is also investigated in an example application in Chapter 5. In addition, the effect of non-Darcy flow on pressure solutions at the tested well as well as throughout the reservoir is considered in a different manner than described in mathematical formulation such that the non-Darcy flow region is restricted to a region of specific radius which is concentric with the wellbore. The thesis ends with conclusions and recommendations which are given in Chapter 6.

2. MATHEMATICAL MODEL FOR 2-D (*r-z*) REAL GAS FLOW IN POROUS MEDIA

Mathematical models refer to physical processes such as the flow of fluids in porous media. Fluid flow in a reservoir can be characterized by partial different equations (PDEs) based on conversation of mass, which are converted into a numerical model by using finite difference approach. In this section, the mathematical formulation is discussed along with the inner and outer boundary condition as well as the finite difference solution procedure.

2.1 Continuity Equation

The mathematical model is presented for single-phase real gas isothermal flow in a cylindrical reservoir of uniform thickness with a single well located at the center. There are some assumptions made in deriving the flow equations such as the constant porosity as well as the neglecting of gravity effects. Flow is considered to be ax symmetrical so that the appropriate initial boundary problem can be formulated in a (*r-z*) coordinate system. The continuity equation for such systems in oil-field units is given by (see for example, Bratvold, 1986):

$$-5.615\left[\frac{1}{r}\frac{\partial}{\partial r}(r\rho v_r)+\frac{\partial}{\partial z}(\rho v_z)\right]=\frac{\partial}{\partial t}(\rho\phi) \qquad \textbf{(2.1)}$$

Here, v_r denotes the value of *r*-component of the velocity vector and v_z denotes the value of *z*-component of the velocity vector in units of RB/ft^2, ρ is density in units of lbm/ft^3, and the term in right hand side of the equation is in lbm/ft^3D.

The relationship between the flow rate and pressure gradient is normally described by Darcy's Law. The differential form of this relationship for single-phase flow in oilfield units where gravity effects are neglected is defined by:

$$v=-1.127\times10^{-3}\ \frac{[k]}{\mu}\ \nabla p \qquad \textbf{(2.2)}$$

where μ is viscosity of the fluid in *cp*, [*k*] is a permeability tensor of the porous media in *mD* and ∇p is the gradient vector of pressure in *psi/ft*. In Eq. 2.2, under the two-dimensional assumption of anisotropy considering a diagonal permeability tensor [*k*] and ∇p are respectively given by:

$$[k]=\begin{pmatrix} k_r & 0 \\ 0 & k_z \end{pmatrix} \tag{2.3}$$

and

$$\nabla p=\begin{pmatrix} \frac{\partial p}{\partial r} \\ \frac{\partial p}{\partial z} \end{pmatrix} \tag{2.4}$$

Eq. 2.2 includes the multiplication of [*k*] and ∇p which is shown below:

$$[k]\nabla p=\begin{pmatrix} k_r & 0 \\ 0 & k_z \end{pmatrix}\begin{pmatrix} \frac{\partial p}{\partial r} \\ \frac{\partial p}{\partial z} \end{pmatrix}=\begin{pmatrix} k_r \frac{\partial p}{\partial r} \\ k_z \frac{\partial p}{\partial z} \end{pmatrix} \tag{2.5}$$

Eq. 2.1 can be written more explicitly as:

$$c_1\left(\frac{1}{r}\frac{\partial}{\partial r}\left[r\rho\frac{k_r}{\mu}\left(\frac{\partial p}{\partial r}\right)\right]+\frac{\partial}{\partial z}\left[\rho\frac{k_z}{\mu}\left(\frac{\partial p}{\partial z}\right)\right]\right)=\frac{\partial}{\partial t}(\rho\phi) \tag{2.6}$$

where a coefficient for simplification is defined as $c_1=6.33\times10^{-3}$. In Eq. 2.6, *t* is given in days.

Note that Darcy's Law assumes that the inertial effects of fluid movement are negligible. This implies that laminar flow prevails and the paths of fluid particles are not affected by the flow rate. As discussed in the next section, this may not be valid for flow of real gases particularly near the wells where the fluids flow with higher velocities compared to the reservoir locations far away from the well due to reduction in cross-sectional area open to flow as well as the low viscosity (or equivalently high mobility) of real gases.

2.2 Non-Darcy Flow Equation

The pressure gradient is shown by Eq. 2.4 to be caused by a linear combination of viscous and inertial forces. In gas flow near the wellbore, where velocities are highest, it is often found that inertial effects are not negligible and deviations from Darcy's Law are observed. In 1901, Forchheimer expressed the pressure gradient in any absolute set of units with respect to one-dimensional (r) flow as:

$$-\frac{\partial p}{\partial r} = \frac{\mu}{k_r} v_r + \beta_r \rho v_r |v_r| \tag{2.7}$$

where β_r is called the coefficient of inertial flow resistance in the r-direction based on Geertsma's description (Geertsma, 1974). Geertsma gave the equation of the inertia coefficient beta which is also called turbulence factor, in field units, ft^{-1} as

$$\beta_r = \frac{48511}{\phi^{5.5}\sqrt{k_r}} \tag{2.8}$$

When turbulence flow feels near wellbore on gas reservoir it is called inertial turbulence flow or non-Darcy flow. After performing the unit conversion from cgs to oilfield units (Bratvold, 1986), Eq. 2.7 can be defined by:

$$-\frac{\partial p}{\partial r} = 8.87220048\times10^{2}\,\frac{\mu}{k_r} v_r + 9.11463311\times10^{-13}\,\beta_r \rho v_r |v_r| \tag{2.9}$$

We multiply both sides of Forchheimer equation given by Eq. 2.9 by k/μ and obtain:

$$-\frac{k_r}{\mu}\frac{\partial p}{\partial r} = \left(8.87220048\times10^{2} + 9.11463311\times10^{-13}\,\frac{k_r}{\mu}\beta_r \rho |v_r|\right) v_r \tag{2.10}$$

or Eq. 2.10 can be written as:

$$v_r = -\frac{1}{\left(8.87220048\times10^{2} + 9.11463311\times10^{-13}\,\frac{k_r}{\mu}\beta_r \rho |v_r|\right)}\frac{k_r}{\mu}\frac{\partial p}{\partial r} \tag{2.11}$$

or Eq. 2.11 can be written as:

$$v_r = -\left(1.127\times10^{-3}\right)\frac{1}{\left(1+1.027324972\times10^{-15}\,\frac{k_r\beta_r\rho}{\mu}|v_r|\right)}\frac{k_r}{\mu}\frac{\partial p}{\partial r} \qquad \textbf{(2.12)}$$

and Eq. 2.12 can be simplified and rearranged as:

$$v_r = -\left(1.127\times10^{-3}\right)\delta_r\frac{k_r}{\mu}\frac{\partial p}{\partial r} \qquad \textbf{(2.13)}$$

where δ_r represents unitless correction factor for non-Darcy flow in the *r*-direction and it will be expressed by:

$$\delta_r = \frac{1}{1+1.027324972\times10^{-15}\,\frac{k_r\beta_r\rho}{\mu}|v_r|} \qquad \textbf{(2.14)}$$

When non-Darcy flow effects are neglected in the model, Geertsma's factor is taken as $\beta=0$, then correction factor for non-Darcy flow is estimated as $\delta_r=1$ in Eq. 2.14.
It should be noted that we consider two-dimensional *r*-*z* flow in our study. So, under two-dimensional flow conditions, we need to define a correction factor in the *z*-direction (δ_z) for the velocity in the *z*-direction to account for non-Darcy flow. Therefore, assuming non-Darcy flow effects both in *r* and *z* directions, Eq. 2.7 can be expressed as:

$$c_1\left(\frac{1}{r}\frac{\partial}{\partial r}\left[\delta_r r\rho\frac{k_r}{\mu}\left(\frac{\partial p}{\partial r}\right)\right]+\frac{\partial}{\partial z}\left[\delta_z\rho\frac{k_z}{\mu}\left(\frac{\partial p}{\partial z}\right)\right]\right)=\frac{\partial}{\partial t}(\rho\phi) \qquad \textbf{(2.15)}$$

2.3 Diffusivity Equation

Note that Eq. 2.15 is a non-linear partial differential equation, because μ and ρ depends on pressure *p*. The well-known equation of state for a real gas can be written as:

$$\rho = \frac{pM}{ZRT} \qquad \textbf{(2.16)}$$

where M is the molecular weight in *lbm/lbm-mole*, T is reservoir temperature in ^oR, R is the universal gas constant, and defined as R=10.732 *psi.ft*^{3}*/lb-mole.*^oR. Now, we wish to evaluate right-hand side of the Eq. 2.15 and it will be obtained as:

$$\frac{\partial}{\partial t}(\rho\phi) = \phi\frac{\partial\rho}{\partial t} + \rho\frac{\partial\phi}{\partial t} = \phi\frac{\partial\rho}{\partial p}\frac{\partial p}{\partial t} + \rho\frac{\partial\phi}{\partial p}\frac{\partial p}{\partial t} = \phi\rho\left[\frac{1}{\rho}\frac{\partial\rho}{\partial p} + \frac{1}{\phi}\frac{\partial\phi}{\partial p}\right]\frac{\partial p}{\partial t} \tag{2.17}$$

The coefficient of isothermal gas compressibility is given by:

$$c_g = \frac{1}{\rho}\left(\frac{\partial\rho}{\partial p}\right)_T \tag{2.18}$$

where T, the reservoir temperature, is fixed, therefore ρ is a unique function of pressure. Thus, the rock isothermal compressibility (c_r) is given by:

$$c_r = \frac{1}{\phi}\frac{\partial\phi}{\partial p} \tag{2.19}$$

Using Eqs. 2.18 and 2.19 in Eq. 2.17 gives:

$$\frac{\partial}{\partial t}(\rho\phi) = \phi\rho c_t\frac{\partial p}{\partial t} \tag{2.20}$$

where c_t represents the total system compressibility and given as:

$$c_t = c_g + c_r \tag{2.21}$$

It is important to note that for real gas flow, coefficient of isothermal gas compressibility is typically much higher than the rock compressibility ($c_g >> c_r$). Thus, although in the simulator developed, we evaluate c_t as given by Eq. 2.2, in terms of practical applications, the total system compressibility can be approximated by the isothermal gas compressibility, i.e.,

$$c_t \approx c_g = \frac{1}{\rho}\frac{\partial\rho}{\partial p} = -\frac{1}{B}\frac{\partial B}{\partial p} = \frac{1}{p} - \frac{1}{Z}\frac{\partial Z}{\partial p} \tag{2.22}$$

Using Eq. 2.21 in Eq. 2.15 yields the diffusivity equation to be defined as:

$$c_1\left(\frac{1}{r}\frac{\partial}{\partial r}\left[\delta_r r\rho\frac{k_r}{\mu}\left(\frac{\partial p}{\partial r}\right)\right]+\frac{\partial}{\partial z}\left[\delta_z\rho\frac{k_z}{\mu}\left(\frac{\partial p}{\partial z}\right)\right]\right)=\phi\rho c_t\frac{\partial p}{\partial t} \qquad \textbf{(2.23)}$$

We wish to express our diffusivity equation in terms of the gas formation volume factor of gas (denoted by B), which is defined as (in ft^3/SCF) as:

$$B=\frac{\rho_{sc}}{\rho} \qquad \textbf{(2.24)}$$

where ρ_{sc} represents the density of gas at standard conditions (i.e., at p_{sc}, and T_{sc}), and ρ represents the density of gas at sandface conditions (i.e., at p_{wf}, and T). Using equation of state for a real gas given by Eq. 2.16 in Eq. 2.24, the formation volume factor, B can be expressed in terms of p, T, and Z as,

$$B=\frac{p_{sc}}{T_{sc}}\left(\frac{ZT}{p}\right) \qquad \textbf{(2.25)}$$

where pressure and temperature at standard conditions are given, respectively, p_{sc}=14.69595 *psi* and T_{sc} =519.6 ^oR. Dividing both sides of our diffusivity equation given by Eq. 2.23 by ρ_{sc}, which is a constant, and then, use the definition of formation volume factor given by Eq. 2.25, then we can express our diffusivity equation given by Eq. 2.23 as:

$$c_1\left(\frac{1}{r}\frac{\partial}{\partial r}\left[r\ \delta_r\frac{k_r}{B\mu}\left(\frac{\partial p}{\partial r}\right)\right]+\frac{\partial}{\partial z}\left[\delta_z\frac{k_z}{B\mu}\left(\frac{\partial p}{\partial z}\right)\right]\right)=\frac{\phi c_t}{B}\frac{\partial p}{\partial t} \qquad \textbf{(2.26)}$$

Note that Eq. 2.29 is still a nonlinear PDE. because B, μ and the non-Darcy correction terms δ_r and δ_z in the left-hand side as well as c_t in the right-hand side of Eq. 2.26 are dependent on pressure.

2.4 Inner and Outer Boundary Conditions

To complete the mathematical formulation of the problem, the appropriate initial and boundary conditions have to be considered. A uniform pressure initial condition in a two-dimensional problem in the r and z directions is given by:

$$p(r,z,t=0)=p_i \tag{2.27}$$

where p_i denotes the initial pressure which is assumed to be uniform throughout the reservoir. For the single-phase real gas, the outer boundary is a no flow outer boundary condition and defined by:

$$\left(\frac{\partial p}{\partial r}\right)_{r=r_e,z\in(0,h)}=0 \tag{2.28}$$

where r_e denotes the reservoir drainage radius.

The schematic of well/reservoir configuration is shown in **Figure 2.1**. Note that h is the reservoir thickness and $z=0$ denotes the top of the reservoir whereas $z=h$ denotes the bottom of the reservoir. The top and bottom boundaries of the reservoir are no flow boundaries and defined as, respectively,

$$\left(\frac{\partial p}{\partial z}\right)_{r\in(r_w,r_e),z=0}=0 \tag{2.29}$$

$$\left(\frac{\partial p}{\partial z}\right)_{r\in(r_w,r_e),z=h}=0 \tag{2.30}$$

Note that any arbitrary sections of the wellbore adjacent to the formation may be open to flow.

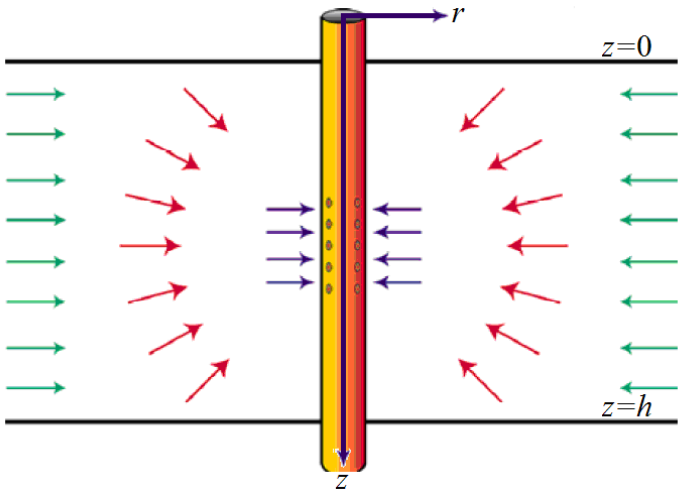

Figure 2.1 : Diagram of reservoir cross section (ECRIN, 2009).

For the single-phase of real gas, the inner boundary condition for the surface rate of production, q_{sc}, accounting for the wellbore storage effects, can be given by:

$$\tilde{q}_{sc}(t) = q_{sf}(t) - \frac{c_g V_w}{B}\frac{dp_{wf}}{dt} \tag{2.31}$$

where V_w denotes the wellbore volume in *RB*, t is time in *days*, $\tilde{q}_{sc}$ represents the specified surface rate in *STB/D*, and q_{sf} represents the sand face rate in *STB/D*, and B represents the gas formation volume factor in *RB/STB* or ft^3/SCF and given in Eq. 2.25. In Eq. 2.31, c_g represents the compressibility of gas evaluated at the sandface conditions and is given in Eq. 2.22 where Z is the well known Z-factor. Note that we can use the standard definition of wellbore storage coefficient given for a compressive type of wellbore storage as:

$$C = c_g V_w \tag{2.32}$$

where C is the wellbore storage coefficient in *RB/psi*. It should be noted that C is not constant and changes with p for a gas well because the isothermal gas compressibility, c_g, defined by Eq. 2.32 changes with pressure. For an option in the simulator, we can treat C as a constant, though this may not be realistic for all pressure ranges and depending on the magnitudes of the pressure drawdown during the drawdown period and pressure rise during the buildup period.

In Eq. 2.31, multiplying both sides by 5.615 ft^3/bbl gives:

$$5.615\tilde{q}_{sc}(t) = 5.615q_{sf}(t) - \frac{5.615c_g V_w}{B}\frac{dp_{wf}}{dt} \tag{2.33}$$

The surface rate of production, q_{sc}, in *SCF/D* can also be expressed as:

$$q_{sc}(t) = 5.615\tilde{q}_{sc}(t) \tag{2.34}$$

Thus, Eq. 2.33 can be rewritten as:

$$q_{sc}(t) = 5.615q_{sf}(t) - \frac{5.615c_g V_w}{B}\frac{dp_{wf}}{dt} \tag{2.35}$$

In Eq. 2.35, the sandface rate, q_{sf}, including the non-Darcy flow effects for a fully penetrating well which may also be represented in a vertical sketch (**Figure 2.1**) from z=0 to z=h given by:

$$q_{sf}(r=r_w,z,t)=1.127\times10^{-3}(2\pi h)\left(r\ \delta_r\frac{k_r}{B\mu}\frac{\partial p}{\partial r}\right)_{r=r_w} \qquad \textbf{(2.36)}$$

Using Eq. 2.36 in Eq. 2.35 gives:

$$q_{sc}(t)=5.615\times1.127\times10^{-3}(2\pi h)\left(r\ \delta_r\frac{k_r}{B\mu}\frac{\partial p}{\partial r}\right)_{r=r_w}-\frac{5.615c_gV_w}{B}\frac{dp_{wf}}{dt} \qquad \textbf{(2.37)}$$

When any arbitrary section of the wellbore adjacent to the formation is open to flow, which may also be represented in a vertical sketch **(2.1)** from z=h_1 to z=h_2, Eq. 2.37 becomes:

$$q_{sc}(t)=5.615\times1.127\times10^{-3}(2\pi)\int_{z=h_1}^{z=h_2}\left(r\ \delta_r\frac{k_r}{B\mu}\frac{\partial p}{\partial r}\right)_{r=r_w}dz-\frac{5.615c_gV_w}{B}\frac{dp_{wf}}{dt} \qquad \textbf{(2.38)}$$

It is important to note that h_1 is distance measured from z=0 to the top of the open interval and h_2 is the distance measured from z=0 to the bottom of the open interval.

2.5 Fully Implicit Finite Difference Formulation

Block-centered grid system (Aziz and Settari, 1979) is valid for this study. Grid system contains properties of reservoir, which are assigned to each grid block. In order to set up the grid blocks in radial coordinates for two dimensional study in the r and z directions, we define N to denote the number of grid blocks in the r-direction and M to denote the number of grid blocks in the z-direction. As we consider two dimensional r-z flow, only one grid block having 360^o in θ direction is considered. Simulator always uses a “block centered grid” with the grid points in the r-direction geometrically spaced (based on the procedure of Mac Donal and Coats, 1970) whereas in the z-direction user defined spaced. If not specified, as default, simulator uses equally spaced grid blocks in z-direction, which may not be realistic in some cases where the well is not fully penetrated and will be discussed further in Chapter 4. For the problem considered in this work the top and bottom boundaries and the

outer boundary are no flow (Neumann type). A general view of the grids used is shown in **Figure 2.2**.

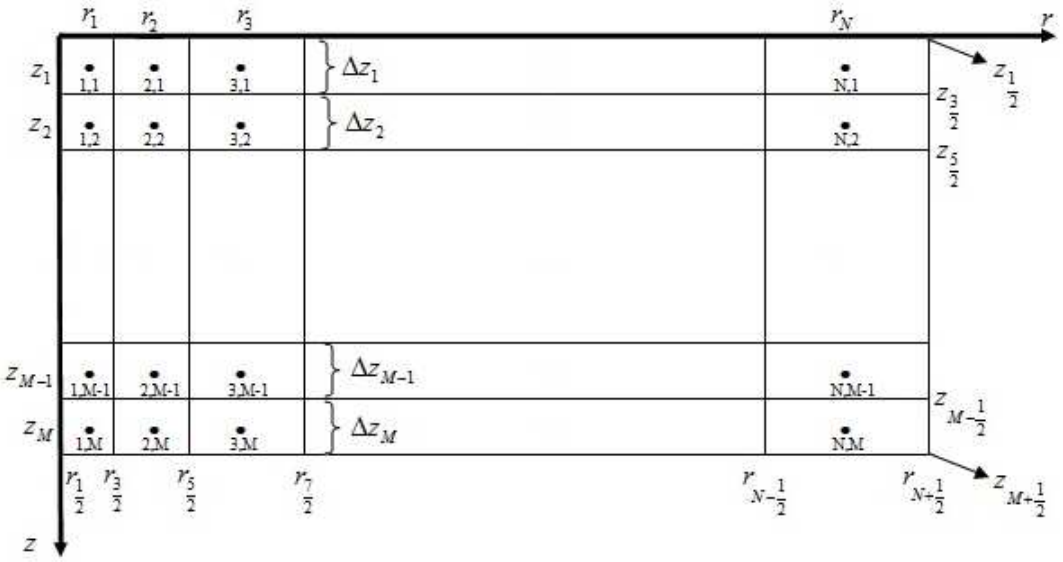

Figure 2.2 : Description and ordering of grid points.

The coordinate system can be defined with *i* and *j* "dummy" index, where the *i* index defines the coordinate in the *r*-direction whereas the index *j* defines the coordinate in the *z*-direction. Coordinate axes for block-centered grid with defining dummy index are shown also in **Figure 2.2**. The dots represent grid points of the form (r_i,z_j) and the subrectangles represent grid blocks. Note that $r_{½}$ is equal to the wellbore radius r_w and $r_{N+½}$ is equal to the reservoir drainage radius r_e whereas $z_{½}$ is equal to zero which represents the top boundary and $z_{M+½}$ is equal to the reservoir thickness.

The *z*-grid points are specified by first defining the block heights, Δz_j , j=1,2,…,M. Thus, taking the top boundary definition as $z_{½}$=0 when the first gridblock in *z*-direction is considered as j=1, the *z*-direction block boundaries $z_{j+½}$, for j=1,2,…,M are defined by:

$$z_{j+\frac{1}{2}} = z_{j-\frac{1}{2}} + \Delta z_j \qquad \textbf{(2.39)}$$

The grid points z_j , for j=1,2,…,M are then defined by

$$z_j = z_{j-\frac{1}{2}} + \left(\frac{\Delta z_j}{2}\right) \qquad \textbf{(2.40)}$$

Given that the terminology block centered grid is used, it may be noted that z_j is the center of each grid block at the vertical direction and can also be expressed as the halfway between $z_{j-½}$ and $z_{j+½}$:

$$z_j = \frac{\left(z_{j-\frac{1}{2}} + z_{j+\frac{1}{2}} \right)}{2} \tag{2.41}$$

Although the z_j's defined here, in our finite difference equations in the following sections, the values of the Δz_j's are used only. As mentioned before and as it is customary, the *r*-grid points are generated geometrically based on the Mac-Donald and Coats method. A standard method to generate grid points, r_i's, and the gridblock boundaries, $r_{i+½}$'s, in the *r*-direction is known as Coat's method. This method is based on the steady-state radial flow equation which is given by:

$$p\left(r_{i+1}\right) - p\left(r_i\right) = F \ln\left[\frac{r_{i+1}}{r_i}\right] \tag{2.42}$$

where F is a constant, $p(r_{i+1})$ and $p(r_i)$ represent the pressure values respectively at grid points r_{i+1} and r_i. Taking into account the definition of steady-state radial flow, in order to have the same pressure difference between r_i and r_{i+1} for i=0,1,...,N, another constant, α is defined by:

$$\alpha = \frac{r_{i+1}}{r_i} \tag{2.43}$$

where α >1. Eq. 2.43 defines calculation of grid points for i=0,1,...,N-1. Furthermore, it should be pointed out that r_0 is a fictitious gridpoint inside the wellbore for the Mac-Donald and Coats method and defined by:

$$r_0 = \frac{r_w \ln(\alpha)}{(\alpha - 1)} \tag{2.44}$$

In Coat's method, grid block boundaries, also shown in **Figure 2.2**, $r_{i+½}$'s, are defined by using the log-mean radius as:

$$r_{i+\frac{1}{2}} = \frac{r_{i+1} - r_i}{\ln\left(\frac{r_{i+1}}{r_i}\right)} = \frac{r_{i+1} - r_i}{\ln \alpha} \tag{2.45}$$

Therefore, initially, α need to be computed so that gridblock points and boundaries given in Eqs. 2.43-45 can also be calculated. α defined in Coat's method, is given by:

$$\alpha = \left(\frac{r_e}{r_w}\right)^{\frac{1}{N}} \tag{2.46}$$

where N is the number of gridblocks to be used in r-direction as mentioned before. Recalling Eq. 2.26 with taking into consideration of derivatives in both side of the equation at any grid block points (r_i, z_j) for the finite difference formulation gives:

$$c_1\left(\frac{1}{r}\frac{\partial}{\partial r}\left[r\ \delta_r \frac{k_r}{B\mu}\left(\frac{\partial p}{\partial r}\right)\right]_{i,j}^{n+1} + \frac{\partial}{\partial z}\left[\delta_z \frac{k_z}{B\mu}\left(\frac{\partial p}{\partial z}\right)\right]_{i,j}^{n+1}\right) = \left(\frac{\phi c_t}{B}\frac{\partial p}{\partial t}\right)_{i,j}^{n+1} \tag{2.47}$$

Eq. 2.47 is separately evaluated here. Therefore, in r-direction, the term of left hand side of the equation can be defined by central difference formulation as:

$$\frac{1}{r}\frac{\partial}{\partial r}\left[r\ \delta_r \frac{k_r}{B\mu}\left(\frac{\partial p}{\partial r}\right)\right]_{i,j}^{n+1} = \left(\frac{1}{r_i}\right)\frac{\left[r\ \delta_r \frac{k_r}{B\mu}\left(\frac{\partial p}{\partial r}\right)\right]_{i+\frac{1}{2},j}^{n+1} - \left[r\ \delta_r \frac{k_r}{B\mu}\left(\frac{\partial p}{\partial r}\right)\right]_{i-\frac{1}{2},j}^{n+1}}{r_{i+\frac{1}{2}} - r_{i-\frac{1}{2}}} \tag{2.48}$$

Provided that r_i is the centered block grid, and can be evaluated as:

$$r_i = \frac{r_{i+\frac{1}{2}} + r_{i-\frac{1}{2}}}{2} \tag{2.49}$$

Using Eq. 2.49 in Eq. 2.48 yields:

$$\frac{1}{r}\frac{\partial}{\partial r}\left[r\ \delta_r \frac{k_r}{B\mu}\left(\frac{\partial p}{\partial r}\right)\right]_{i,j}^{n+1} = \left(\frac{2}{r_{i+\frac{1}{2}}^2 - r_{i-\frac{1}{2}}^2}\right)\left(r_{i+\frac{1}{2}}\left[\delta_r \frac{k_r}{B\mu}\left(\frac{\partial p}{\partial r}\right)\right]_{i+\frac{1}{2},j}^{n+1} - r_{i-\frac{1}{2}}\left[\delta_r \frac{k_r}{B\mu}\left(\frac{\partial p}{\partial r}\right)\right]_{i-\frac{1}{2},j}^{n+1}\right) \tag{2.50}$$

In *z*-direction, the term of left hand side of Eq. 2.47 can be defined by central difference formulation as:

$$\frac{\partial}{\partial z}\left[\delta_z \frac{k_z}{B\mu}\left(\frac{\partial p}{\partial z}\right)\right]_{i,j}^{n+1} = \frac{\left[\delta_z \frac{k_z}{B\mu}\left(\frac{\partial p}{\partial z}\right)\right]_{i,j+\frac{1}{2}}^{n+1} - \left[\delta_z \frac{k_z}{B\mu}\left(\frac{\partial p}{\partial z}\right)\right]_{i,j-\frac{1}{2}}^{n+1}}{z_{i+\frac{1}{2}} - z_{i-\frac{1}{2}}} \tag{2.51}$$

Consequently, derivation of $\partial p/\partial r$ and $\partial p/\partial z$, in Eqs. 2.50 and 2.51 can be evaluated with central finite difference formulation as:

$$\left(\frac{\partial p}{\partial r}\right)_{i+\frac{1}{2},j}^{n+1} = \frac{p_{i+1,j}^{n+1} - p_{i,j}^{n+1}}{r_{i+1} - r_i} \tag{2.52a}$$

$$\left(\frac{\partial p}{\partial r}\right)_{i-\frac{1}{2},j}^{n+1} = \frac{p_{i,j}^{n+1} - p_{i-1,j}^{n+1}}{r_i - r_{i-1}} \tag{2.52b}$$

$$\left(\frac{\partial p}{\partial z}\right)_{i,j+\frac{1}{2}}^{n+1} = \frac{p_{i,j+1}^{n+1} - p_{i,j}^{n+1}}{z_{j+1} - z_j} \tag{2.53a}$$

$$\left(\frac{\partial p}{\partial z}\right)_{i,j-\frac{1}{2}}^{n+1} = \frac{p_{i,j}^{n+1} - p_{i,j-1}^{n+1}}{z_j - z_{j-1}} \tag{2.53b}$$

The term of right hand side of Eq. 2.47 includes time derivative which can be defined by dividing it into consecutive points as $[0 = t^0, t^1, t^2, t^3, ..., t^n, t^{n+1} = t]$. Therefore, difference in time between each consecutive point is called time step or delta time, Δt^{n+1}, which can be taken as $\Delta t^{n+1} = t^{n+1} - t^n$. Using this definition for any time steps,

we wish to consider the backward difference in time derivative, and rewrite the term of right hand side of Eq. 2.47 as:

$$\left(\frac{\phi c_t}{B}\frac{\partial p}{\partial t}\right)_{i,j}^{n+1}=\left(\frac{\phi c_t}{B}\right)_{i,j}^{n+1}\frac{p_{i,j}^{n+1}-p_{i,j}^{n}}{\Delta t^{n+1}} \tag{2.54}$$

Eq. 2.47 can be simply rearranged with the terms defined by Eqs. 2.50-2.54 as:

$$\begin{aligned}&c_1\left\{\frac{2}{r_{i+\frac{1}{2}}^2-r_{i-\frac{1}{2}}^2}\left(r_{i+\frac{1}{2}}\left[\delta_r\frac{k_r}{B\mu}\right]_{i+\frac{1}{2},j}^{n+1}\left(\frac{p_{i+1,j}^{n+1}-p_{i,j}^{n+1}}{r_{i+1}-r_i}\right)-r_{i-\frac{1}{2}}\left[\delta_r\frac{k_r}{B\mu}\right]_{i-\frac{1}{2},j}^{n+1}\left(\frac{p_{i,j}^{n+1}-p_{i-1,j}^{n+1}}{r_i-r_{i-1}}\right)\right)\right.\\&\left.+\frac{1}{z_{i+\frac{1}{2}}-z_{i-\frac{1}{2}}}\left(\left[\delta_z\frac{k_z}{B\mu}\right]_{i,j+\frac{1}{2}}^{n+1}\left(\frac{p_{i,j+1}^{n+1}-p_{i,j}^{n+1}}{z_{j+1}-z_j}\right)-\left[\delta_z\frac{k_z}{B\mu}\right]_{i,j-\frac{1}{2}}^{n+1}\left(\frac{p_{i,j}^{n+1}-p_{i,j-1}^{n+1}}{z_j-z_{j-1}}\right)\right)\right\}\\&=\left(\frac{\phi c_t}{B}\right)_{i,j}^{n+1}\frac{p_{i,j}^{n+1}-p_{i,j}^{n}}{\Delta t^{n+1}}\end{aligned} \tag{2.55}$$

We can rearrange Eq. 2.55 in such a way that the gridblock volume of any gridpoint (r_i, z_j), which is taken as $Vp_{i,j}=\phi\pi(r^2_{i+½}-r^2_{i-½})\Delta z_j$, will remain on the right hand side of the equation. Therefore, Eq. 2.56 need to be multiplied by the term of $\pi(r^2_{i+½}-r^2_{i-½})\Delta z_j$, and then, rewritten as:

$$\begin{aligned}&c_1\left\{2\pi\Delta z_j\left(\frac{r_{i+\frac{1}{2}}}{r_{i+1}-r_i}\left[\delta_r\frac{k_r}{B\mu}\right]_{i+\frac{1}{2},j}^{n+1}\left(p_{i+1,j}^{n+1}-p_{i,j}^{n+1}\right)-\frac{r_{i-\frac{1}{2}}}{r_i-r_{i-1}}\left[\delta_r\frac{k_r}{B\mu}\right]_{i-\frac{1}{2},j}^{n+1}\left(p_{i,j}^{n+1}-p_{i-1,j}^{n+1}\right)\right)\right.\\&+\pi\left(r_{i+\frac{1}{2}}^2-r_{i-\frac{1}{2}}^2\right)\left(\frac{1}{z_{j+1}-z_j}\left[\delta_z\frac{k_z}{B\mu}\right]_{i,j+\frac{1}{2}}^{n+1}\left(p_{i,j+1}^{n+1}-p_{i,j}^{n+1}\right)\right.\\&\left.\left.-\frac{1}{z_j-z_{j-1}}\left[\delta_z\frac{k_z}{B\mu}\right]_{i,j-\frac{1}{2}}^{n+1}\left(p_{i,j}^{n+1}-p_{i,j-1}^{n+1}\right)\right)\right\}=\left(\frac{\phi c_t}{B}\right)_{i,j}^{n+1}\left(p_{i,j}^{n+1}-p_{i,j}^{n}\right)\left(\frac{Vp_{i,j}}{\Delta t^{n+1}}\right)\end{aligned} \tag{2.56}$$

Using the definition of α in Eq. 2.45, transmissibility terms in r-direction and z-direction at a grid block, (r_i, z_j)'s boundaries can be defined as:

$$Tr_{i+\frac{1}{2},j}^{n+1}=c_1 2\pi\Delta z_j\left(\frac{1}{\ln\alpha}\right)\left[\delta_r\frac{k_r}{B\mu}\right]_{i+\frac{1}{2},j}^{n+1} \tag{2.57a}$$

$$Tr^{n+1}_{i-\frac{1}{2},j} = c_1 2\pi\Delta z_j \left(\frac{1}{\ln\alpha}\right)\left[\delta_r \frac{k_r}{B\mu}\right]^{n+1}_{i-\frac{1}{2},j} \tag{2.57b}$$

$$Tz^{n+1}_{i,j+\frac{1}{2}} = c_1\pi\left(r^2_{i+\frac{1}{2}} - r^2_{i-\frac{1}{2}}\right)\left(\frac{1}{z_{j+1} - z_j}\right)\left[\delta_z \frac{k_z}{B\mu}\right]^{n+1}_{i,j+\frac{1}{2}} \tag{2.57c}$$

$$Tz^{n+1}_{i,j-\frac{1}{2}} = c_1\pi\left(r^2_{i+\frac{1}{2}} - r^2_{i-\frac{1}{2}}\right)\left(\frac{1}{z_j - z_{j-1}}\right)\left[\delta_z \frac{k_z}{B\mu}\right]^{n+1}_{i,j-\frac{1}{2}} \tag{2.57d}$$

Furthermore, the volumetric term at a grid block, (r_i, z_j) is defined as:

$$V^{n+1}_{i,j} = \left(\frac{\phi c_t}{B}\right)^{n+1}_{i,j}\left(\frac{Vp_{i,j}}{\Delta t^{n+1}}\right) \tag{2.59}$$

Thus, using the preceding definitions of transmissibility and volumetric terms, Eq. 2.56 can be rewritten for i=2,...,N and j=1,...,M as:

$$\begin{aligned} &Tr^{n+1}_{i+\frac{1}{2},j}\left(p^{n+1}_{i+1,j} - p^{n+1}_{i,j}\right) - Tr^{n+1}_{i-\frac{1}{2},j}\left(p^{n+1}_{i,j} - p^{n+1}_{i-1,j}\right) + Tz^{n+1}_{i,j+\frac{1}{2}}\left(p^{n+1}_{i,j+1} - p^{n+1}_{i,j}\right) \\ &-Tz^{n+1}_{i,j-\frac{1}{2}}\left(p^{n+1}_{i,j} - p^{n+1}_{i,j-1}\right) = V^{n+1}_{i,j}\left(p^{n+1}_{i,j} - p^{n}_{i,j}\right) \end{aligned} \tag{2.60}$$

It is important to note that transmissibility term in r-direction, when i=1, is the representative section of the wellbore adjacent to the formation and should be defined in a different manner since it decides whether the layer beyond this gridblock is open to flow or not. Therefore, Eq. 2.52b is approximated as:

$$\left(\frac{\partial p}{\partial r}\right)^{n+1}_{\frac{1}{2},j} = \frac{p^{n+1}_{1,j} - p^{n+1}_{wf}}{r_1 - r_w} \tag{2.61}$$

The subscript j is not included in the wellbore pressure expansion. Since gravity effects are neglected, p^{n+1}_{wf} is not a function of depth in Eq. 2.61. Thus, the transmissibility term recalculated for j=1,2,...,M as:

$$Tr_{\frac{1}{2},j}^{n+1} = c_1 2\pi\Delta z_j \left(\frac{r_w}{r_1 - r_w}\right)\left[\delta_r \frac{k_r}{B\mu}\right]_{\frac{1}{2},j}^{n+1} \tag{2.62}$$

Thus, using the preceding definitions of transmissibility, when i=1, we may rewrite Eq. 2.60 as:

$$\begin{aligned} &T_{\frac{3}{2},j}^{n+1}\left(p_{2,j}^{n+1} - p_{1,j}^{n+1}\right) - T_{\frac{1}{2},j}^{n+1}\left(p_{1,j}^{n+1} - p_{wf}^{n+1}\right) + T_{1,j+\frac{1}{2}}^{n+1}\left(p_{1,j+1}^{n+1} - p_{1,j}^{n+1}\right) \\ &- T_{1,j-\frac{1}{2}}^{n+1}\left(p_{1,j}^{n+1} - p_{1,j-1}^{n+1}\right) = V_{1,j}^{n+1}\left(p_{1,j}^{n+1} - p_{1,j}^{n}\right) \end{aligned} \tag{2.63}$$

Please note that along the closed wellbore interval at all z_j's, we simply require to clarify the following term in Eq. 2.62 as:

$$\left[\delta_r \frac{k_r}{B\mu}\right]_{\frac{1}{2},j}^{n+1} = 0 \tag{2.64}$$

Thus, the transmissibility term yields,

$$T_{\frac{1}{2},j}^{n+1} = 0 \tag{2.65}$$

Recalling the boundary condition in Eq. 2.28, it is important to note that when i=N, in order to incorporate a no flow outer boundary condition, transmissibility term yields for j=1,2,...,M :

$$Tr_{N+\frac{1}{2},j}^{n+1} = 0 \tag{2.66}$$

Recalling the boundary conditions in Eqs. 2.29 and 2.30, it is important to note that when j=1 or j=N, in order to incorporate the top and bottom boundary conditions, transmissibility terms yield, respectively, for i=1,2,...,N:

$$T_{i,\frac{1}{2}}^{n+1} = 0 \tag{2.67a}$$

$$T_{i,M+\frac{1}{2}}^{n+1} = 0 \tag{2.67b}$$

Recalling Eq. 2.63, we can rewrite our system of equations by putting unknown pressure terms one side and known pressure terms to the other side as:

$$p_{i,j-1}^{n+1}\left(T_{i,j-\frac{1}{2}}^{n+1}\right)+p_{i-1,j}^{n+1}\left(T_{i-\frac{1}{2},j}^{n+1}\right)+p_{i+1,j}^{n+1}\left(T_{i+\frac{1}{2},j}^{n+1}\right)+p_{i,j+1}^{n+1}\left(T_{i,j+\frac{1}{2}}^{n+1}\right)$$
$$+p_{i,j}^{n+1}\left(-T_{i-\frac{1}{2},j}^{n+1}-T_{i+\frac{1}{2},j}^{n+1}-T_{i,j-\frac{1}{2}}^{n+1}-T_{i,j+\frac{1}{2}}^{n+1}-V_{i,j}^{n+1}\right)=-V_{i,j}^{n+1}p_{i,j}^{n} \qquad \textbf{(2.68)}$$

Eq. 2.68 contains *NxM* unknown pressures, $p_{i,j}^{n+1}$ for i=1,2,...,N and j=1,2,...,M , and *NxM* equations. Since there is a production at a specified surface flow rate, q_{sc}^{n+1} , in the model, p_{wf}^{n+1} will be an unknown as well. In that case, the system of equations will have *NxM*+1 unknowns (p_{wf}^{n+1} and $p_{i,j}^{n+1}$ for i=1,2,...,N and j=1,2,...,M), but have *NxM* equations. Therefore, we need to add another equation. The extra equation is obtained by approximating the inner boundary condition from Eq. 2.38, which can be differenced by using Eq. 2.61, as:

$$q_{sc}=5.615\times1.127\times10^{-3}\left(2\pi\right)\left\{\sum_{m=1}^{Nopi}\sum_{j=n_{tm}}^{n_{bm}}\left(r_w\left[\delta_r\frac{k_r}{B\mu}\right]_{\frac{1}{2},j}^{n+1}\left(\frac{p_{1,j}^{n+1}-p_{wf}^{n+1}}{r_1-r_w}\right)\right)\Delta z_j\right.$$
$$\left.-\frac{5.615c_gV_w}{B}\left(\frac{p_{wf}^{n+1}-p_{wf}^{n}}{\Delta t^{n+1}}\right)\right\} \qquad \textbf{(2.69)}$$

where *Nopi* denotes the total number of open intervals adjacent to the wellbore and n_{tm} denotes the grid block number in the z-direction to top of the open interval m and n_{bm} denotes the grid block number in the z-direction to the bottom of the open interval m. Note that Eq. 2.69 is a general inner boundary condition in the sense that we can simulate flow towards the well through multiple open intervals along the wellbore. We define a wellbore storage, C_{ws}, as:

$$C_{ws}^{n+1}=\frac{5.615V_w}{\Delta t^{n+1}}\left(\frac{c_g}{B}\right)_{r=r_w}^{n+1} \qquad \textbf{(2.70)}$$

Recalling transmissibility term, when i=1, from Eq. 2.62, and rewrite Eq. 2.69 as:

$$q_{sc}^{n+1} = \sum_{m=1}^{Nopi} \sum_{j=n_{tm}}^{n_{bm}} T_{\frac{1}{2},j}^{n+1} \left(p_{1,j}^{n+1} - p_{wf}^{n+1} \right) - C_{ws}^{n+1} \left(p_{wf}^{n+1} - p_{wf}^{n} \right) \tag{2.71}$$

Rearranging Eq. 2.71 by putting unknown pressure terms one side and known pressure terms to the other side gives:

$$\left(\sum_{m=1}^{Nopi} \sum_{j=n_{tm}}^{n_{bm}} p_{1,j}^{n+1} Tr_{\frac{1}{2},j}^{n+1} \right) + p_{wf}^{n+1} \left(C_{ws}^{n+1} - \sum_{j=1}^{j=M} Tr_{\frac{1}{2},j}^{n+1} \right) = q_{sc}^{n+1} - C_{ws}^{n+1} p_{wf}^{n} \tag{2.72}$$

2.5.1 Averaging procedure

Let's evaluate all transmissibility terms in r-direction and z-direction, which contain the sums, consequently in Eqs. 2.73.

$$\left[\delta_r \frac{k_r}{B\mu} \right]_{i+\frac{1}{2},j}^{n+1} \quad , \quad \left[\delta_r \frac{k_r}{B\mu} \right]_{i-\frac{1}{2},j}^{n+1} \quad , \quad \left[\delta_z \frac{k_z}{B\mu} \right]_{i,j+\frac{1}{2}}^{n+1} \quad , \quad \left[\delta_z \frac{k_z}{B\mu} \right]_{i,j-\frac{1}{2}}^{n+1} \tag{2.73}$$

We use the harmonic averages for the permeability (Aziz and Settari, 1979). Therefore, permeability in r-direction can be derived as:

$$k_{r_{i+\frac{1}{2},j}} = \frac{\left(k_r\right)_{i,j} \left(k_r\right)_{i+1,j} \ln\left(\frac{r_{i+1}}{r_i} \right)}{\left(k_r\right)_{i,j} \ln\left(\frac{r_{i+1}}{r_{i+\frac{1}{2}}} \right) + \left(k_r\right)_{i+1,j} \ln\left(\frac{r_{i+\frac{1}{2}}}{r_i} \right)} \tag{2.74}$$

whereas permeability in z-direction will be derived as:

$$k_{z_{i,j+\frac{1}{2}}} = \frac{\left(k_z\right)_{i,j} \left(k_z\right)_{i,j+1} \left(\Delta z_j + \Delta z_{j+1} \right)}{\left(k_z\right)_{i,j} \Delta z_{j+1} + \left(k_z\right)_{i,j+1} \Delta z_j} \tag{2.75}$$

Furthermore, the pressure dependent terms in the sums in Eq. 2.73 are δ, μ and B. It can be obtained from Eq. 2.14 that δ_r and δ_z are functions of ρ and μ.

Recalling Eq. 2.25, ρ is given by Eq. 2.26. Therefore, B and μ need be evaluated by using a simple averaging given by:

$$B^{n+1}_{i+\frac{1}{2},j} = \frac{B^{n+1}_{i+1,j} + B^{n+1}_{i,j}}{2} \quad , \quad B^{n+1}_{i-\frac{1}{2},j} = \frac{B^{n+1}_{i,j} + B^{n+1}_{i-1,j}}{2}$$

$$B^{n+1}_{i,j+\frac{1}{2}} = \frac{B^{n+1}_{i,j+1} + B^{n+1}_{i,j}}{2} \quad , \quad B^{n+1}_{i,j-\frac{1}{2}} = \frac{B^{n+1}_{i,j} + B^{n+1}_{i,j-1}}{2} \qquad \textbf{(2.76)}$$

$$\mu^{n+1}_{i+\frac{1}{2},j} = \frac{\mu^{n+1}_{i+1,j} + \mu^{n+1}_{i,j}}{2} \quad , \quad \mu^{n+1}_{i-\frac{1}{2},j} = \frac{\mu^{n+1}_{i,j} + \mu^{n+1}_{i-1,j}}{2}$$

$$\mu^{n+1}_{i,j+\frac{1}{2}} = \frac{\mu^{n+1}_{i,j+1} + \mu^{n+1}_{i,j}}{2} \quad , \quad \mu^{n+1}_{i,j-\frac{1}{2}} = \frac{\mu^{n+1}_{i,j} + \mu^{n+1}_{i,j-1}}{2} \qquad \textbf{(2.77)}$$

Then, the terms discussed in Eqs. 2.73 yield,

$$\left[\delta_r \frac{k_r}{B\mu}\right]^{n+1}_{i+\frac{1}{2},j} = 4k_r{}^{n+1}_{i+\frac{1}{2},j} \left[\frac{\delta_r{}^{n+1}_{i+\frac{1}{2},j}}{\left(B_{i+1,j} + B_{i,j}\right)\left(\mu_{i+1,j} + \mu_{i,j}\right)}\right] \qquad \textbf{(2.78a)}$$

$$\left[\delta_r \frac{k_r}{B\mu}\right]^{n+1}_{i-\frac{1}{2},j} = 4k_r{}^{n+1}_{i-\frac{1}{2},j} \left[\frac{\delta_r{}^{n+1}_{i-\frac{1}{2},j}}{\left(B_{i,j} + B_{i-1,j}\right)\left(\mu_{i,j} + \mu_{i-1,j}\right)}\right] \qquad \textbf{(2.78b)}$$

$$\left[\delta_z \frac{k_z}{B\mu}\right]^{n+1}_{i,j+\frac{1}{2}} = 4k_z{}^{n+1}_{i,j+\frac{1}{2}} \left[\frac{\delta_z{}^{n+1}_{i,j+\frac{1}{2}}}{\left(B_{i,j+1} + B_{i,j}\right)\left(\mu_{i,j+1} + \mu_{i,j}\right)}\right] \qquad \textbf{(2.78c)}$$

$$\left[\delta_z \frac{k_z}{B\mu}\right]^{n+1}_{i,j-\frac{1}{2}} = 4k_z{}^{n+1}_{i,j-\frac{1}{2}} \left[\frac{\delta_z{}^{n+1}_{i,j-\frac{1}{2}}}{\left(B_{i,j} + B_{i,j-1}\right)\left(\mu_{i,j} + \mu_{i,j-1}\right)}\right] \qquad \textbf{(2.78d)}$$

In order to compute the terms δ_r and δ_z at the boundaries, in Eqs. 2.78a-2.78d, which reflect the non-Darcy flow effects and also called correction factor, we need to recall Eq. 2.14. Here, in order to give an example of the calculation of correction factor, we will evaluate only the correction factor in *r*-direction defined by Eq. 2.78a.

To start with, let's define a new term as:

$$\gamma_r = 1.027324972\times10^{-15}\,\frac{k_r\beta_r\rho}{\mu} \tag{2.79}$$

Using Eq. 2.79 in Eq. 2.14 gives:

$$\delta_r = \frac{1}{1+\gamma_r\left|v_r\right|} \tag{2.80}$$

Since $v_r > 0$, let's recall Eq. 2.14 and use in Eq. 2.80.

$$\delta_r = \frac{1}{1+\hat{\gamma}_r\ \delta_r\left|\frac{\partial p}{\partial r}\right|} \tag{2.81}$$

where

$$\hat{\gamma}_r = \gamma_r\left(1.127\times10^{-3}\,\frac{k_r}{\mu}\right) = \left(1.127\times10^{-3}\right)\left(1.027324972\times10^{-15}\right)\frac{\beta_r\rho k_r^2}{\mu^2} \tag{2.82}$$

Let's define another term as:

$$\theta_r = \hat{\gamma}_r\left|\frac{\partial p}{\partial r}\right| \tag{2.83}$$

Then, Eq. 2.81 becomes:

$$\delta_r = \frac{1}{1+\theta_r\ \delta_r} \tag{2.84}$$

Since $\theta > 0$ and $\delta_r > 0$, then the root that we are interested is:

$$\delta_r = \frac{-1+\sqrt{1+4\theta_r}}{2\theta_r} \tag{2.85}$$

Thus, δ_r is simplified and rearranged as:

$$\begin{aligned}\delta_r &= \frac{1}{2\theta_r}\left(\sqrt{1+4\theta_r}-1\right)\\ &= \frac{1}{2\theta_r}\left(\frac{\left(\sqrt{1+4\theta_r}-1\right)\left(\sqrt{1+4\theta_r}+1\right)}{\sqrt{1+4\theta_r}+1}\right)\\ &= \frac{1}{2\theta_r}\ \frac{4\theta_r}{\sqrt{1+4\theta_r}+1}\\ &= \frac{2}{1+\sqrt{1+4\theta_r}}\end{aligned} \tag{2.86}$$

Therefore, the term discussed, $\delta_{r_{i+\frac{1}{2},j}}^{n+1}$, can be defined by:

$$\delta_{r_{i+\frac{1}{2},j}}^{n+1} = \frac{2}{1+\sqrt{1+4\theta_{r_{i+\frac{1}{2},j}}^{n+1}}} \tag{2.87}$$

where

$$\theta_{r_{i+\frac{1}{2},j}}^{n+1} = \hat{\gamma}_{r_{i+\frac{1}{2},j}}^{n+1}\left|\left(\frac{\partial p}{\partial r}\right)_{i+\frac{1}{2},j}^{n+1}\right| \tag{2.88}$$

and

$$\hat{\gamma}_{r_{i+\frac{1}{2},j}}^{n+1} = \left(1.127\times10^{-3}\right)\left(1.027324972\times10^{-15}\right)\left(\frac{\beta_r\rho k_r^2}{\mu^2}\right)_{i+\frac{1}{2},j}^{n+1} \tag{2.89}$$

Please note that we use the same equations given by Eqs. 2.79 – 2.89 replacing the subscript *r* by the subscript *z* for *z*-direction non-Darcy flow corrections.

2.5.2 Incorporation of skin zone

A skin factor is incorporated into our finite difference model by two different approaches. First case is the use of the thick skin concept of Hawkins (Hawkins, 1956). Specifically, we represent a skin region as a zone of altered permeability adjacent to the producing interval. The horizontal permeability of the skin zone, $k_{r,s}$

is defined by specifying the radius of the skin region, r_s, the skin factor, S, and using the following equation of Hawkins:

$$s = \left(\frac{k_r}{k_{r,s}} - 1 \right) \ln \left(\frac{r_s}{r_w} \right) \tag{2.90}$$

We wish to choose r_s to be equal to a gridblock boundary. If $s>0$, it is convenient to choose the fifth gridblock boundary as $r_s=r_{5/2,j}$. Then, we need to evaluate $k_{r,5/2,j}$ for $j=1,2,\ldots,M$ as harmonic averages of $k_{r,s,5/2,j}$ and $k_{r,5/2,j}$ using Eq. 2.74. For skin case, we replace $k_{r,i+1/2,j}$ in all transmissibility terms as well as in all Geertsma's beta terms, in order to incorporate with non-Darcy flow effects, by $k_{s,i+1/2,j}$ for the skin zone. The vertical permeability in the skin region $k_{z,s}$ is assigned by requiring that:

$$\frac{k_{z,s}}{k_{r,s}} = \frac{k_z}{k_r} \tag{2.91}$$

Second case is to add individual skin to each gridblock which is adjacent to the producing interval and open to flow. Transmissibility term which is discussed in Eq. 2.62, when $i=1$, for $j=1,2,...,M$ yields:

$$Tr_{\frac{1}{2},j}^{n+1} = c_1 2\pi \Delta z_j \left(\frac{1}{\frac{r_{3/2}^2}{r_{3/2}^2 - r_w^2} \ln \left(\frac{r_{3/2}}{r_w} \right) - \frac{1}{2} + S_{1,j} + D\left| q_{sc}^{n+1} \right|} \right) \left[\delta_r \frac{k_r}{\mu} \right]_{\frac{1}{2},j}^{n+1} \tag{2.92}$$

In this case, we need to evaluate non-Darcy flow effects in a different manner and introduce a new non-Darcy flow coefficient called as D, in the units of $(MSCF/D)^{-1}$, which is given by:

$$D = \frac{2.715 \times 10^{-15} \beta_r}{r_w h} \left(\frac{k_r}{\mu_{wf}} \right) \left(\frac{p_{sc} M}{T_{sc}} \right) \tag{2.93}$$

where k_r is the permeability in the units of mD in r-direction since D is an input to transmissibility term in r-direction, and it can be assigned by user in the simulator in the presence of heterogeneous distribution of permeability throughout the reservoir; μ_{wf} is viscosity evaluated at wellbore flowing pressure and it can be evaluated either

in the beginning or in the end of the production period by user defined in the simulator, β_r is Geertsma's term in ft^{-1} in Eq. 2.8, and permeability and porosity terms in the equation can also be evaluated by user in the simulator in the presence of heterogeneous distributions of permeability and porosity throughout the reservoir. In Eq. 2.93, absolute value of flow rate term is expressed due to the consideration of injection cases in the flow rate history that may be defined by user. It should also be noted that during buildup period, the flow rate term is not taken as zero constant rate to represent buildup. Instead, it is automatically considered by the last flow rate of the production even if multiple productions exist before the buildup. The correction term for non-Darcy flow effects, called as δ, need to be excluded from all equations in transmissibility definitions when this case is considered. In this case, we simply treat non-Darcy flow effects in our simulation model as a constant, though this may not be realistic for all pressure ranges and depending on the magnitudes of the pressure drawdown during the drawdown period and pressure rise during the buildup period.

Non-Darcy correction factor, δ, as can be seen in finite difference equations derived in Chapter 3, depend on the terms which change with pressure and temperature as well as porosity and permeability when heterogeneity exists throughout the reservoir at a given time during the simulation. Therefore, non-Darcy flow effects can not be calculated as a constant value in finite difference equations. However, ECRIN defines non-Darcy flow effects by using well-known term in literature called as non-Darcy coefficient, D, which is an easily calculated constant value (Eq. 2.93), and implemented as an input to all transmissibility terms of the gridblocks that are adjacent to the wellbore. Although treating non-Darcy flow effects as a constant value may not be realistic for all pressure ranges, it is used widely in the industry since data interpretation techniques need to define a constant value in order to evaluate flow regimes represented by pressure responses during well testing.

Finally, since most of the turbulent flow takes place near the wellbore in producing formations, the effect of non-Darcy flow is a rate-dependent skin effect. The formula that relates the total skin to the mechanical skin to non-Darcy skin is given by

$$S_t = S + D|q_{sc}| \tag{2.94}$$

where S_t denotes the total skin factor, S is the mechanical skin due to damage or stimulation, D is the non-Darcy coefficient in $(MSCF/D)^{-1}$, and q_{sc} is the flow rate for the drawdown period preceding a buildup period. This method needs multiple production or buildup periods to be evaluated in Eq. 2.94 and will be further discussed with examples in verification and application chapters.

3. METHODS OF NUMERICAL SOLUTION

Eqs. 2.68 and 2.72 constitute our finite difference system of equations to be solved for pressures which are unknown at the center of gridblocks. Once the pressure at time level t^n is given, the system of difference equations can be solved to obtain pressure at time level t^{n+1}. In order to solve the pressure values, a matrix solution process must be developed. Many procedures have been advocated for solving the system of difference equations. There are two methods discussed in this section to obtain an implicit pressure solution.

Let's write system of equations for each grid block in an example model of three grid blocks in *r*-direction and three grid blocks in *z*-direction shown in **Figure 3.1**. Suppose we produce at a specified surface flow rate in fully penetrating well through the entire thickness of the reservoir with a no flow outer, top and bottom boundary conditions.

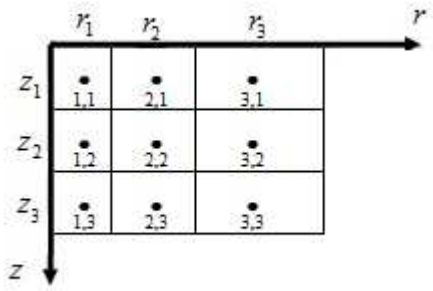

Figure 3.1 : Ordering of the pressure points.

Initially, Eq. 2.68 need to be modified for i=1,2,3 and j=1,2,3 and generate NxM equations with NxM unknows as:

When i=1, j=1, it is given by:

$$p_{wf}^{n+1}\left(Tr_{\frac{1}{2},1}^{n+1}\right)+p_{2,1}^{n+1}\left(Tr_{\frac{3}{2},1}^{n+1}\right)+p_{1,2}^{n+1}\left(Tz_{1,\frac{3}{2}}^{n+1}\right)$$
$$+p_{1,1}^{n+1}\left(-Tr_{\frac{1}{2},1}^{n+1}-Tr_{\frac{3}{2},1}^{n+1}-Tz_{1,\frac{3}{2}}^{n+1}-V_{1,1}^{n+1}\right)=-V_{1,1}^{n+1}p_{1,1}^{n} \qquad \textbf{(3.1)}$$

When i=1, j=2, it is given by:

$$p_{1,1}^{n+1}\left(Tz_{1,\frac{3}{2}}^{n+1}\right)+p_{wf}^{n+1}\left(Tr_{\frac{1}{2},2}^{n+1}\right)+p_{2,2}^{n+1}\left(Tr_{\frac{3}{2},2}^{n+1}\right)+p_{1,3}^{n+1}\left(Tz_{1,\frac{5}{2}}^{n+1}\right)$$
$$+p_{1,2}^{n+1}\left(-Tr_{\frac{1}{2},2}^{n+1}-Tr_{\frac{3}{2},2}^{n+1}-Tz_{1,\frac{3}{2}}^{n+1}-Tz_{1,\frac{5}{2}}^{n+1}-V_{1,2}^{n+1}\right)=-V_{1,2}^{n+1}p_{1,2}^{n} \quad \textbf{(3.2)}$$

When i=1, j=3, it is given by:

$$p_{1,2}^{n+1}\left(Tz_{1,\frac{5}{2}}^{n+1}\right)+p_{wf}^{n+1}\left(Tr_{\frac{1}{2},3}^{n+1}\right)+p_{2,3}^{n+1}\left(Tr_{\frac{3}{2},3}^{n+1}\right)$$
$$+p_{1,3}^{n+1}\left(-Tr_{\frac{1}{2},3}^{n+1}-Tr_{\frac{3}{2},3}^{n+1}-Tz_{1,\frac{5}{2}}^{n+1}-V_{1,3}^{n+1}\right)=-V_{1,3}^{n+1}p_{1,3}^{n} \quad \textbf{(3.3)}$$

When i=2, j=1, it is given by:

$$p_{1,1}^{n+1}\left(Tr_{\frac{3}{2},1}^{n+1}\right)+p_{3,1}^{n+1}\left(Tr_{\frac{5}{2},1}^{n+1}\right)+p_{2,2}^{n+1}\left(Tz_{2,\frac{3}{2}}^{n+1}\right)$$
$$+p_{2,1}^{n+1}\left(-Tr_{\frac{3}{2},1}^{n+1}-Tr_{\frac{5}{2},1}^{n+1}-Tz_{2,\frac{3}{2}}^{n+1}-V_{2,1}^{n+1}\right)=-V_{2,1}^{n+1}p_{2,1}^{n} \quad \textbf{(3.4)}$$

When i=2, j=2, it is given by:

$$p_{2,1}^{n+1}\left(Tz_{2,\frac{3}{2}}^{n+1}\right)+p_{1,2}^{n+1}\left(Tr_{\frac{3}{2},2}^{n+1}\right)+p_{3,2}^{n+1}\left(Tr_{\frac{5}{2},2}^{n+1}\right)+p_{2,3}^{n+1}\left(Tz_{2,\frac{5}{2}}^{n+1}\right)$$
$$+p_{2,2}^{n+1}\left(-Tr_{\frac{3}{2},2}^{n+1}-Tr_{\frac{5}{2},2}^{n+1}-Tz_{2,\frac{3}{2}}^{n+1}-Tz_{2,\frac{5}{2}}^{n+1}-V_{2,2}^{n+1}\right)=-V_{2,2}^{n+1}p_{2,2}^{n} \quad \textbf{(3.5)}$$

When i=2, j=3, it is given by:

$$p_{2,2}^{n+1}\left(Tz_{2,\frac{5}{2}}^{n+1}\right)+p_{1,3}^{n+1}\left(Tr_{\frac{3}{2},3}^{n+1}\right)+p_{3,3}^{n+1}\left(Tr_{\frac{5}{2},3}^{n+1}\right)$$
$$+p_{2,3}^{n+1}\left(-Tr_{\frac{3}{2},3}^{n+1}-Tr_{\frac{5}{2},3}^{n+1}-Tz_{2,\frac{5}{2}}^{n+1}-V_{2,3}^{n+1}\right)=-V_{2,3}^{n+1}p_{2,3}^{n} \quad \textbf{(3.6)}$$

When i=3, j=1, it is given by:

$$p_{2,1}^{n+1}\left(Tr_{\frac{5}{2},1}^{n+1}\right)+p_{3,2}^{n+1}\left(Tz_{3,\frac{3}{2}}^{n+1}\right)+p_{3,1}^{n+1}\left(-Tr_{\frac{5}{2},1}^{n+1}-Tz_{3,\frac{3}{2}}^{n+1}-V_{3,1}^{n+1}\right)=-V_{3,1}^{n+1}p_{3,1}^{n} \tag{3.7}$$

When i=3, j=2, it is given by:

$$\begin{aligned}&p_{3,1}^{n+1}\left(Tz_{3,\frac{3}{2}}^{n+1}\right)+p_{2,2}^{n+1}\left(Tr_{\frac{5}{2},2}^{n+1}\right)+p_{3,3}^{n+1}\left(Tz_{3,\frac{5}{2}}^{n+1}\right)\\&+p_{3,2}^{n+1}\left(-Tr_{\frac{5}{2},2}^{n+1}-Tz_{3,\frac{3}{2}}^{n+1}-Tz_{3,\frac{5}{2}}^{n+1}-V_{3,2}^{n+1}\right)=-V_{3,2}^{n+1}p_{3,2}^{n}\end{aligned} \tag{3.8}$$

When i=3, j=3, it is given by:

$$p_{3,2}^{n+1}\left(Tz_{3,\frac{5}{2}}^{n+1}\right)+p_{2,3}^{n+1}\left(Tr_{\frac{5}{2},3}^{n+1}\right)+p_{3,3}^{n+1}\left(-Tr_{\frac{5}{2},3}^{n+1}-Tz_{3,\frac{5}{2}}^{n+1}-V_{3,3}^{n+1}\right)=-V_{3,3}^{n+1}p_{3,3}^{n} \tag{3.9}$$

Additionally, since we would like to produce at a specified surface flow rate and also solve wellbore pressure, p_{wf}^{n+1}, Eq. 2.72 needs to be modified for a fully penetrating well as:

$$\begin{aligned}&p_{1,1}^{n+1}\left(Tr_{\frac{1}{2},1}^{n+1}\right)+p_{1,2}^{n+1}\left(Tr_{\frac{1}{2},2}^{n+1}\right)+p_{1,3}^{n+1}\left(Tr_{\frac{1}{2},3}^{n+1}\right)\\&+p_{wf}^{n+1}\left[C_{ws}^{n+1}-\left(Tr_{\frac{1}{2},1}^{n+1}+Tr_{\frac{1}{2},2}^{n+1}+Tr_{\frac{1}{2},3}^{n+1}\right)\right]=q_{sc}^{n+1}-C_{ws}^{n+1}p_{wf}^{n}\end{aligned} \tag{3.10}$$

Therefore, system of equations is obtained for the model considered above. There are ten equations and ten unknown pressures to solve in each time step called as $p_{1,1}$, $p_{1,2}$, $p_{1,3}$, $p_{2,1}$, $p_{2,2}$, $p_{2,3}$, $p_{3,1}$, $p_{3,2}$, $p_{3,3}$, p_{wf} for a specified surface flow rate which can be either positive for production and negative for injection cases.

The above system of reservoir and well equations can be solved implicitly either using the Newton method or functional iteration method, as to be discussed next.

3.1 Newton Method

The Newton method is the most accurate method of solving the nonlinear system of equations, but it is computationally expensive as it requires computation of the derivatives of the system of equations with respect to the unknowns. The method is briefly described below.

3.1.1 Brief description

In order to solve, system of equations described in the previous section, first, we discuss well known Newton's method in numerical analysis, (also known as the Newton–Raphson method), named after Isaac Newton and Joseph Raphson, which is a method for finding successively better approximations to the roots (or zeroes) of a real-valued function.

Given a function $f(x)$ and its derivative $f'(x)$, we begin with a first guess x_0 for a root of the function. Provided the function is reasonably well-behaved a better approximation x_1 is given by:

$$x_1 = x_0 - \frac{f(x_0)}{f'(x_0)} \tag{3.11}$$

or it can be rearranged as:

$$f'(x_0) \times (x_1 - x_0) = -f(x_0) \tag{3.12}$$

Geometrically, x_1 is the intersection with the x-axis of a line tangent to f at $f(x_0)$. The process is repeated until a sufficiently accurate value is reached:

$$x_{k+1} = x_k - \frac{f(x_k)}{f'(x_k)} \tag{3.13}$$

or rearranging

$$f'(x_k) \times (x_{k+1} - x_k) = -f(x_k) \tag{3.14}$$

Now, suppose we have N system of equations with N independent variables such as:

$$\begin{aligned} & f_1\left(x_1, x_2, ..., x_N\right) = 0 \\ & f_1\left(x_1, x_2, ..., x_N\right) = 0 \\ & \vdots \\ & f_N\left(x_1, x_2, ..., x_N\right) = 0 \end{aligned} \tag{3.15}$$

Eq. 3.15 can be taken as $f_i(x_1,x_2,...,x_N)=0$ for $i=1,2,...,N$. We would like to solve x_i's which can also be expressed as $\mathbf{x}=[x_1,x_2,...,x_N]$ so that $f_i(\mathbf{x})=0$ for $i=1,2,...,N$. We let $\hat{\mathbf{x}}$ be the solution such that $f_i(\mathbf{x})=0$ for $i=1,2,...,N$. If $\mathbf{x}$ is close to $\hat{\mathbf{x}}$, then the Taylor series is approximately satisfied for $i=1,2,...,N$ as:

$$f_i\left(\hat{\mathbf{x}}\right) = f_i\left(\mathbf{x}\right) + \sum_{j=1}^{N}\left(\hat{x}_j - x_j\right)\frac{\partial f_i\left(\mathbf{x}\right)}{\partial x_j} \tag{3.16}$$

or because all f_i's are zero at the solution vector $\hat{\mathbf{x}}$, then Eq. 3.16 can be rearranged to obtain:

$$\sum_{j=1}^{N}\frac{\partial f_i\left(\mathbf{x}\right)}{\partial x_j}\left(\hat{x}_j - x_j\right) = -f_i\left(\mathbf{x}\right) \tag{3.17}$$

This suggests an iterative scheme for $i=1,2,...,N$ with an iteration index l, as given by:

$$\sum_{j=1}^{N}\frac{\partial f_i\left(\mathbf{x}^l\right)}{\partial x_j}\left(x_j^{l+1} - x_j^l\right) = -f_i\left(\mathbf{x}^l\right) \tag{3.18}$$

If we let ψ_i^{l+1} to denote $\psi_j^{l+1} = x_j^{l+1} - x_j^l$ for $j=1,2,...,N$, then, system of equations can be defined as:

$$\begin{aligned} & \frac{\partial f_1\left(\mathbf{x}^l\right)}{\partial x_1}\psi_1^{l+1} + \frac{\partial f_1\left(\mathbf{x}^l\right)}{\partial x_2}\psi_2^{l+1} + \frac{\partial f_1\left(\mathbf{x}^l\right)}{\partial x_3}\psi_3^{l+1} + ... + \frac{\partial f_1\left(\mathbf{x}^l\right)}{\partial x_N}\psi_N^{l+1} = -f_1\left(\mathbf{x}^l\right) \\ & \frac{\partial f_2\left(\mathbf{x}^l\right)}{\partial x_1}\psi_1^{l+1} + \frac{\partial f_2\left(\mathbf{x}^l\right)}{\partial x_2}\psi_2^{l+1} + \frac{\partial f_2\left(\mathbf{x}^l\right)}{\partial x_3}\psi_3^{l+1} + ... + \frac{\partial f_2\left(\mathbf{x}^l\right)}{\partial x_N}\psi_N^{l+1} = -f_2\left(\mathbf{x}^l\right) \\ & \vdots \\ & \frac{\partial f_N\left(\mathbf{x}^l\right)}{\partial x_1}\psi_1^{l+1} + \frac{\partial f_N\left(\mathbf{x}^l\right)}{\partial x_2}\psi_2^{l+1} + \frac{\partial f_N\left(\mathbf{x}^l\right)}{\partial x_3}\psi_3^{l+1} + ... + \frac{\partial f_N\left(\mathbf{x}^l\right)}{\partial x_N}\psi_N^{l+1} = -f_N\left(\mathbf{x}^l\right) \end{aligned} \tag{3.19}$$

For the system of equations described in Eq. 3.19, the coefficient matrix, also called as Jacobian matrix, is given by:

$$\mathbf{J}\left(\mathbf{x}^{l}\right)=\begin{pmatrix} \frac{\partial f_1}{\partial x_1} & \frac{\partial f_1}{\partial x_2} & \cdots & \frac{\partial f_1}{\partial x_N} \\ \frac{\partial f_2}{\partial x_1} & \frac{\partial f_2}{\partial x_2} & \cdots & \frac{\partial f_2}{\partial x_1} \\ \vdots & \vdots & \ddots & \vdots \\ \frac{\partial f_N}{\partial x_1} & \frac{\partial f_N}{\partial x_2} & \cdots & \frac{\partial f_N}{\partial x_N} \end{pmatrix} \tag{3.20}$$

Furthermore, in order to define unknown terms of the system, another matrix is developed as:

$$\boldsymbol{\psi}^{l+1}=\begin{pmatrix} \boldsymbol{\psi}_1^{l+1} \\ \boldsymbol{\psi}_2^{l+1} \\ \vdots \\ \boldsymbol{\psi}_N^{l+1} \end{pmatrix} \tag{3.21}$$

Consequently, the matrix for right hand side of the system of equations is given by:

$$\mathbf{f}\left(\mathbf{x}^{l}\right)=\begin{pmatrix} f_1\left(\mathbf{x}^{l}\right) \\ f_2\left(\mathbf{x}^{l}\right) \\ \vdots \\ f_N\left(\mathbf{x}^{l}\right) \end{pmatrix} \tag{3.22}$$

Then, our solution yields:

$$\mathbf{J}\left(x^{l+1}\right)\boldsymbol{\psi}^{l+1}=-f\left(\mathbf{x}^{l}\right) \tag{3.23}$$

The procedure steps are, respectively,

1. Set l=0 and guess $\mathbf{x}^{l}=\left[x_1^0, x_2^0, ..., x_N^0\right]^T$.
2. Form $\mathbf{J}\left(x^{l}\right)$ and $f\left(x^{l}\right)$
3. Compute $\boldsymbol{\psi}^{l+1}$ and compute $x^{l+1}=x^{l}+\psi^{l+1}$

4. Check the term in Eq. 3.24 if it is satisfied or not. If so, accept x^{l+1} as the solution and stop iterating.

$$\max_{i \le j \le N} \left| \frac{x_j^{l+1} - x_j^l}{x_j^{l+1} + 10^{-13}} \right| \le \in \tag{3.24}$$

5. If condition given in Step 3 is not satisfied, set $l=l+1$ and go to Step 2.

The procedure will converge to $\hat{\mathbf{x}}$ provided that:

- $\mathbf{J}^{-1}\left(x^l\right)$ exists. In order words, $\mathbf{J}\left(x^l\right)$ is non-singular.
- For x^0 (initial guess) is sufficiently close to $\hat{\mathbf{x}}$.

Note that Newton's method converges much faster than the functional iteration method.

3.1.2 Matrix problem

The Jacobian matrix to be used in the Newton method involves the derivatives of the residual equations (Eq. 3.20). These derivatives can be calculated either analytically or numerically as discussed in the following subsections. It is preferable to use the analytical approach due to less computational labor compared to the numerical approach. We considered numerical approach here just to make sure that our analytical expressions used in the analytical approach are correct.

3.1.2.1 Analytical approach for derivatives

In order to set up Newton's procedure for the model described in this chapter, Eqs. 3.25 and 3.26 define the terms described in Eq. 3.23 in order to solve the system for a delta time, Δt, which can be taken between the time steps from t^n to t^{n+1}. Here, upscript $(k+1)$ and k denotes the standard ordering notation of the number of iterations if iteration is not converged at the first time and so on. The vector and matrices to be used for the simple example application of **Figure 3.1** as follows:

$$\psi^{l+1}=\begin{pmatrix} p_{1,1}^{n+1,l+1}-p_{1,1}^{n+1,l} \\ p_{2,1}^{n+1,l+1}-p_{2,1}^{n+1,l} \\ p_{3,1}^{n+1,l+1}-p_{3,1}^{n+1,l} \\ p_{1,2}^{n+1,l+1}-p_{1,2}^{n+1,l} \\ p_{2,2}^{n+1,l+1}-p_{2,2}^{n+1,l} \\ p_{3,2}^{n+1,l+1}-p_{3,2}^{n+1,l} \\ p_{1,3}^{n+1,l+1}-p_{1,3}^{n+1,l} \\ p_{2,3}^{n+1,l+1}-p_{2,3}^{n+1,l} \\ p_{3,3}^{n+1,l+1}-p_{3,3}^{n+1,l} \\ p_{wf}^{n+1,l+1}-p_{wf}^{n+1,l} \end{pmatrix}, \mathbf{p}^{n+1,l}=\begin{pmatrix} p_{1,1}^{n+1,l} \\ p_{2,1}^{n+1,l} \\ p_{3,1}^{n+1,l} \\ p_{1,2}^{n+1,l} \\ p_{2,2}^{n+1,l} \\ p_{3,2}^{n+1,l} \\ p_{1,3}^{n+1,l} \\ p_{2,3}^{n+1,l} \\ p_{3,3}^{n+1,l} \\ p_{wf}^{n+1,l} \end{pmatrix}, \mathbf{f}\left(p^{n+1,l}\right)=\begin{pmatrix} f_{1,1}\left(p^{n+1,l}\right) \\ f_{2,1}\left(p^{n+1,l}\right) \\ f_{3,1}\left(p^{n+1,l}\right) \\ f_{1,2}\left(p^{n+1,l}\right) \\ f_{2,2}\left(p^{n+1,l}\right) \\ f_{3,2}\left(p^{n+1,l}\right) \\ f_{1,3}\left(p^{n+1,l}\right) \\ f_{2,3}\left(p^{n+1,l}\right) \\ f_{3,3}\left(p^{n+1,l}\right) \\ f_{wf}\left(p^{n+1,l}\right) \end{pmatrix} \quad \textbf{(3.25)}$$

The coefficient matrix is evaluated in the time step, t^{n+1}, is given by:

$$\mathbf{J}\left(\mathbf{x}^{l+1}\right)=\begin{pmatrix} \frac{\partial f_{1,1}}{\partial p_{1,1}^{n+1}} & \frac{\partial f_{1,1}}{\partial p_{2,1}^{n+1}} & 0 & \frac{\partial f_{1,1}}{\partial p_{1,2}^{n+1}} & 0 & 0 & 0 & 0 & 0 & \frac{\partial f_{1,1}}{\partial p_{wf}^{n+1}} \\ \frac{\partial f_{2,1}}{\partial p_{1,1}^{n+1}} & \frac{\partial f_{2,1}}{\partial p_{2,1}^{n+1}} & \frac{\partial f_{2,1}}{\partial p_{3,1}^{n+1}} & 0 & \frac{\partial f_{2,1}}{\partial p_{2,2}^{n+1}} & 0 & 0 & 0 & 0 & 0 \\ 0 & \frac{\partial f_{3,1}}{\partial p_{2,1}^{n+1}} & \frac{\partial f_{3,1}}{\partial p_{3,1}^{n+1}} & 0 & 0 & \frac{\partial f_{3,1}}{\partial p_{3,2}^{n+1}} & 0 & 0 & 0 & 0 \\ \frac{\partial f_{1,2}}{\partial p_{1,1}^{n+1}} & 0 & 0 & \frac{\partial f_{1,2}}{\partial p_{1,2}^{n+1}} & \frac{\partial f_{1,2}}{\partial p_{2,2}^{n+1}} & 0 & \frac{\partial f_{1,2}}{\partial p_{1,3}^{n+1}} & 0 & 0 & \frac{\partial f_{1,2}}{\partial p_{wf}^{n+1}} \\ 0 & \frac{\partial f_{2,2}}{\partial p_{2,1}^{n+1}} & 0 & \frac{\partial f_{2,2}}{\partial p_{1,2}^{n+1}} & \frac{\partial f_{2,2}}{\partial p_{2,2}^{n+1}} & \frac{\partial f_{2,2}}{\partial p_{3,2}^{n+1}} & 0 & \frac{\partial f_{2,2}}{\partial p_{2,3}^{n+1}} & 0 & 0 \\ 0 & 0 & \frac{\partial f_{3,2}}{\partial p_{3,1}^{n+1}} & 0 & \frac{\partial f_{3,2}}{\partial p_{2,2}^{n+1}} & \frac{\partial f_{3,2}}{\partial p_{3,2}^{n+1}} & 0 & 0 & \frac{\partial f_{3,2}}{\partial p_{3,3}^{n+1}} & 0 \\ 0 & 0 & 0 & \frac{\partial f_{1,3}}{\partial p_{1,2}^{n+1}} & 0 & 0 & \frac{\partial f_{1,3}}{\partial p_{1,3}^{n+1}} & \frac{\partial f_{1,3}}{\partial p_{2,3}^{n+1}} & 0 & \frac{\partial f_{1,3}}{\partial p_{wf}^{n+1}} \\ 0 & 0 & 0 & 0 & \frac{\partial f_{2,3}}{\partial p_{2,2}^{n+1}} & 0 & \frac{\partial f_{2,3}}{\partial p_{1,3}^{n+1}} & \frac{\partial f_{2,3}}{\partial p_{2,3}^{n+1}} & \frac{\partial f_{2,3}}{\partial p_{3,3}^{n+1}} & 0 \\ 0 & 0 & 0 & 0 & 0 & \frac{\partial f_{3,3}}{\partial p_{3,2}^{n+1}} & 0 & \frac{\partial f_{3,3}}{\partial p_{2,3}^{n+1}} & \frac{\partial f_{3,3}}{\partial p_{3,3}^{n+1}} & 0 \\ \frac{\partial f_{wf}}{\partial p_{1,1}^{n+1}} & 0 & 0 & \frac{\partial f_{wf}}{\partial p_{1,2}^{n+1}} & 0 & 0 & \frac{\partial f_{wf}}{\partial p_{1,3}^{n+1}} & 0 & 0 & \frac{\partial f_{wf}}{\partial p_{wf}^{n+1}} \end{pmatrix} \quad \textbf{(3.26)}$$

Therefore, Eq. 3.25 requires the derivatives of system of equations described in Eqs. 3.1-3.10 with respect to all unknowns individually. Let's rewrite Eq. 2.68 in a

general form for i=1,2,…,N and j=1,2,…M in order to take derivates with respect to each of the gridblock's pressures in the system:

$$f_{i,j} = p_{i,j-1}^{n+1}\left(T_{i,j-\frac{1}{2}}^{n+1}\right) + p_{i-1,j}^{n+1}\left(T_{i-\frac{1}{2},j}^{n+1}\right) + p_{i+1,j}^{n+1}\left(T_{i+\frac{1}{2},j}^{n+1}\right) + p_{i,j+1}^{n+1}\left(T_{i,j+\frac{1}{2}}^{n+1}\right)$$
$$+ p_{i,j}^{n+1}\left(-T_{i,j-\frac{1}{2}}^{n+1} - T_{i,j+\frac{1}{2}}^{n+1} - T_{i-\frac{1}{2},j}^{n+1} - T_{i+\frac{1}{2},j}^{n+1} - V_{i,j}^{n+1}\right) + V_{i,j}^{n+1} p_{i,j}^{n} \qquad \textbf{(3.27)}$$

Similarly, let's rewrite Eq. 2.72 in a general form for j=1,2,...,M as:

$$f_{wf} = \left(\sum_{j=1}^{j=M} p_{1,j}^{n+1} Tr_{\frac{1}{2},j}^{n+1}\right) + p_{wf}^{n+1}\left(C_{ws}^{n+1} - \sum_{j=1}^{j=M} Tr_{\frac{1}{2},j}^{n+1}\right) - q_{sc}^{n+1} + C_{ws}^{n+1} p_{wf}^{n} \qquad \textbf{(3.28)}$$

Since averaging procedure is used to calculate the properties at the gridblock boundaries, there will be non-zero terms always in the same ordering at the coefficient matrix as long as the open interval to flow will not change during the simulation. **Figure 3.2** represents an example for the gridpoint (2,2) in order to show the non-zero derivative terms' requiring calculation with respect to its neighbours' pressure values.

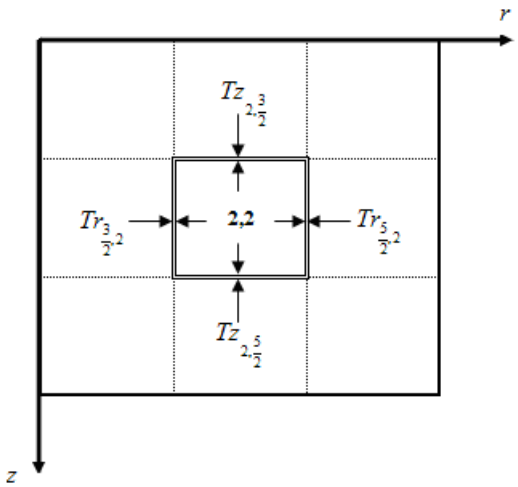

Figure 3.2 : Averaging procedure.

Derivatives of Eq. 3.26 for any gridblock in the model with respect to each neighbour gridblock's pressures as well as with respect to its own pressure are given by:

$$\frac{\partial f_{i,j}}{\partial p^{n+1}_{i,j-1}} = Tz^{n+1}_{i,j-\frac{1}{2}} + \left(\frac{\partial Tz^{n+1}_{i,j-\frac{1}{2}}}{\partial p^{n+1}_{i,j-1}} \right) \left(p^{n+1}_{i,j-1} - p^{n+1}_{i,j} \right) \tag{3.29a}$$

$$\frac{\partial f_{i,j}}{\partial p^{n+1}_{i,j+1}} = Tz^{n+1}_{i,j+\frac{1}{2}} + \left(\frac{\partial Tz^{n+1}_{i,j+\frac{1}{2}}}{\partial p^{n+1}_{i,j+1}} \right) \left(p^{n+1}_{i,j+1} - p^{n+1}_{i,j} \right) \tag{3.29b}$$

$$\frac{\partial f_{i,j}}{\partial p^{n+1}_{i-1,j}} = Tr^{n+1}_{i-\frac{1}{2},j} + \left(\frac{\partial Tr^{n+1}_{i-\frac{1}{2},j}}{\partial p^{n+1}_{i-1,j}} \right) \left(p^{n+1}_{i-1,j} - p^{n+1}_{i,j} \right) \tag{3.29c}$$

$$\frac{\partial f_{i,j}}{\partial p^{n+1}_{i+1,j}} = Tr^{n+1}_{i+\frac{1}{2},j} + \left(\frac{\partial Tr^{n+1}_{i+\frac{1}{2},j}}{\partial p^{n+1}_{i+1,j}} \right) \left(p^{n+1}_{i+1,j} - p^{n+1}_{i,j} \right) \tag{3.29d}$$

$$\begin{aligned} \frac{\partial f_{i,j}}{\partial p^{n+1}_{i,j}} = & -Tz^{n+1}_{i,j-\frac{1}{2}} + \left(\frac{\partial Tz^{n+1}_{i,j-\frac{1}{2}}}{\partial p^{n+1}_{i,j}} \right) \left(p^{n+1}_{i,j-1} - p^{n+1}_{i,j} \right) - Tz^{n+1}_{i,j+\frac{1}{2}} \\ & + \left(\frac{\partial Tz^{n+1}_{i,j+\frac{1}{2}}}{\partial p^{n+1}_{i,j}} \right) \left(p^{n+1}_{i,j+1} - p^{n+1}_{i,j} \right) - Tr^{n+1}_{i-\frac{1}{2},j} + \left(\frac{\partial Tr^{n+1}_{i-\frac{1}{2},j}}{\partial p^{n+1}_{i,j}} \right) \left(p^{n+1}_{i-1,j} - p^{n+1}_{i,j} \right) \\ & - Tr^{n+1}_{i+\frac{1}{2},j} \left(\frac{\partial Tr^{n+1}_{i+\frac{1}{2},j}}{\partial p^{n+1}_{i,j}} \right) \left(p^{n+1}_{i+1,j} - p^{n+1}_{i,j} \right) - V^{n+1}_{i,j} + \left(\frac{\partial V^{n+1}_{i,j}}{\partial p^{n+1}_{i,j}} \right) \left(p^{n}_{i,j} - p^{n+1}_{i,j} \right) \end{aligned} \tag{3.29e}$$

The gridblocks, when i=1, for j=1,2,…,M in Eq. 3.26, which are adjacent to the formation and open to flow, requires another derivative with respect to wellbore pressure and it is given by:

$$\frac{\partial f_{1,j}}{\partial p^{n+1}_{wf}} = Tr^{n+1}_{\frac{1}{2},j} + \left(\frac{\partial Tr^{n+1}_{\frac{1}{2},j}}{\partial p^{n+1}_{wf}} \right) \left(p^{n+1}_{wf} - p^{n+1}_{1,j} \right) \tag{3.30}$$

Eq. 3.27, which is also called as well equation, requires derivatives with respect to the gridblocks, when i=1, for j=1,2,…,M , which are adjacent to the formation and open to flow, and it is given by:

$$\frac{\partial f_{wf}}{\partial p_{1,j}^{n+1}} = Tr_{\frac{1}{2},j}^{n+1} + \left(\frac{\partial Tr_{\frac{1}{2},j}^{n+1}}{\partial p_{1,j}^{n+1}} \right) \left(p_{1,j}^{n+1} - p_{wf}^{n+1} \right) \tag{3.31}$$

Well equation's derivative with respect to wellbore pressure is given by:

$$\frac{\partial f_{wf}}{\partial p_{wf}^{n+1}} = \sum_{j=1}^{j=M} \left[Tr_{\frac{1}{2},j}^{n+1} + \left(\frac{\partial Tr_{\frac{1}{2},j}^{n+1}}{\partial p_{wf}^{n+1}} \right) \left(p_{1,j}^{n+1} - p_{wf}^{n+1} \right) \right] - C_{ws}^{n+1} + \frac{\partial C_{ws}^{n+1}}{\partial p_{wf}^{n+1}} \left(p_{wf}^{n} - p_{wf}^{n+1} \right) \tag{3.32}$$

Transmissibility's derivatives need to be defined in Eqs. 3.29-3.31. Using Eq. 2.78b in Eq. 2.57b gives the transmissibility term which is required to compute for Eq. 2.29d:

$$Tr_{i-\frac{1}{2},j}^{n+1} = c_1 2\pi \Delta z_j \left(\frac{1}{\ln \alpha} \right) 4k_{r_{i-\frac{1}{2},j}}^{n+1} \left[\frac{\delta_{r_{i-\frac{1}{2},j}}^{n+1}}{\left(B_{i,j} + B_{i-1,j} \right) \left(\mu_{i,j} + \mu_{i-1,j} \right)} \right] \tag{3.33}$$

Derivative of Eq. 3.33 with respect to the gridblock pressure at (r_i, z_j) is given by:

$$\frac{\partial Tr_{i-\frac{1}{2},j}^{n+1}}{\partial p_{i,j}^{n+1}} = c_1 2\pi \Delta z_j \left(\frac{1}{\ln \alpha} \right) 4k_{r_{i-\frac{1}{2},j}}^{n+1} \left(\frac{\frac{\partial \delta_{r_{i-\frac{1}{2},j}}^{n+1}}{\partial p_{i,j}^{n+1}}}{\left(B_{i,j} + B_{i-1,j} \right) \left(\mu_{i,j} + \mu_{i-1,j} \right)} - \frac{\delta_{r_{i-\frac{1}{2},j}}^{n+1} \left[\left(\frac{\partial B_{i,j}}{\partial p_{i,j}^{n+1}} \mu_{i,j} + B_{i,j} \frac{\partial \mu_{i,j}}{\partial p_{i,j}^{n+1}} \right) + \left(\frac{\partial B_{i,j}}{\partial p_{i,j}^{n+1}} \mu_{i-1,j} \right) + \left(B_{i-1,j} \frac{\partial \mu_{i,j}}{\partial p_{i,j}^{n+1}} \right) \right]}{\left[\left(B_{i,j} + B_{i-1,j} \right) \left(\mu_{i,j} + \mu_{i-1,j} \right) \right]^2} \right) \tag{3.34}$$

Derivative of Eq. 3.33 with respect to the gridblock pressure at (r_{i-1}, z_j) is given by:

$$\frac{\partial Tr^{n+1}_{i-\frac{1}{2},j}}{\partial p^{n+1}_{i-1,j}} = c_1 2\pi\Delta z_j \left(\frac{1}{\ln\alpha}\right) 4k_{r^{n+1}_{i-\frac{1}{2},j}} \left(\frac{\dfrac{\partial \delta^{n+1}_{r_{i-\frac{1}{2},j}}}{\partial p^{n+1}_{i-1,j}}}{\left(B_{i,j}+B_{i-1,j}\right)\left(\mu_{i,j}+\mu_{i-1,j}\right)} - \frac{\delta^{n+1}_{r_{i-\frac{1}{2},j}} \left[\left(B_i \dfrac{\partial \mu_{i-1}}{\partial p^{n+1}_{i-1,j}} \right) + \left(\dfrac{\partial B_{i-1}}{\partial p^{n+1}_{i-1,j}} \mu_i \right) + \left(\dfrac{\partial B_{i-1}}{\partial p^{n+1}_{i-1,j}} \mu_{i-1} + B_{i-1} \dfrac{\partial \mu_{i-1}}{\partial p^{n+1}_{i-1,j}} \right) \right]}{\left[\left(B_{i,j}+B_{i-1,j}\right)\left(\mu_{i,j}+\mu_{i-1,j}\right)\right]^2} \right) \tag{3.35}$$

Using Eq. 2.78b in Eq. 2.57b gives the transmissibility term which is required to compute for Eq. 2.29d:

$$Tr^{n+1}_{i+\frac{1}{2},j} = c_1 2\pi\Delta z_j \left(\frac{1}{\ln\alpha}\right) 4k_{r^{n+1}_{i+\frac{1}{2},j}} \left[\frac{\delta^{n+1}_{r_{i+\frac{1}{2},j}}}{\left(B_{i+1,j}+B_{i,j}\right)\left(\mu_{i+1,j}+\mu_{i,j}\right)} \right] \tag{3.36}$$

Derivative of Eq. 3.33 with respect to the gridblock pressure at (r_i, z_j) is given by:

$$\frac{\partial Tr^{n+1}_{i+\frac{1}{2},j}}{\partial p^{n+1}_{i,j}} = c_1 2\pi\Delta z_j \left(\frac{1}{\ln\alpha}\right) 4k_{r^{n+1}_{i+\frac{1}{2},j}} \left(\frac{\dfrac{\partial \delta^{n+1}_{r_{i+\frac{1}{2},j}}}{\partial p^{n+1}_{i,j}}}{\left(B_{i+1,j}+B_{i,j}\right)\left(\mu_{i+1,j}+\mu_{i,j}\right)} - \frac{\delta^{n+1}_{r_{i+\frac{1}{2},j}} \left[\left(B_{i+1,j} \dfrac{\partial \mu_{i,j}}{\partial p^{n+1}_{i,j}} \right) + \left(\dfrac{\partial B_{i,j}}{\partial p^{n+1}_{i,j}} \mu_{i+1,j} \right) + \left(\dfrac{\partial B_{i,j}}{\partial p^{n+1}_{i,j}} \mu_{i,j} + B_{i,j} \dfrac{\partial \mu_{i,j}}{\partial p^{n+1}_{i,j}} \right) \right]}{\left[\left(B_{i+1,j}+B_{i,j}\right)\left(\mu_{i+1,j}+\mu_{i,j}\right)\right]^2} \right) \tag{3.37}$$

Derivative of Eq. 3.33 with respect to the gridblock pressure at (r_{i+1}, z_j) is given by:

$$\frac{\partial Tr^{n+1}_{i+\frac{1}{2},j}}{\partial p^{n+1}_{i+1,j}} = c_1 2\pi\Delta z_j \left(\frac{1}{\ln\alpha}\right) 4k_{r^{n+1}_{i+\frac{1}{2},j}} \left(\frac{\frac{\partial \delta^{n+1}_{r_{i+\frac{1}{2},j}}}{\partial p^{n+1}_{i+1,j}}}{\left(B_{i+1,j}+B_{i,j}\right)\left(\mu_{i+1,j}+\mu_{i,j}\right)} \right.$$

$$\left. - \frac{\delta^{n+1}_{r_{i+\frac{1}{2},j}} \left[\left(B_{i+1,j} \frac{\partial \mu_{i,j}}{\partial p^{n+1}_{i+1,j}} \right) + \left(\frac{\partial B_{i,j}}{\partial p^{n+1}_{i+1,j}} \mu_{i+1,j} \right) + \left(\frac{\partial B_{i,j}}{\partial p^{n+1}_{i+1,j}} \mu_{i,j} + B_{i,j} \frac{\partial \mu_{i,j}}{\partial p^{n+1}_{i+1,j}} \right) \right]}{\left[\left(B_{i+1,j}+B_{i,j}\right)\left(\mu_{i+1,j}+\mu_{i,j}\right) \right]^2} \right) \quad \textbf{(3.38)}$$

Using Eq. 2.78b in Eq. 2.57b gives the transmissibility term which is required to compute for Eq. 2.29d:

$$Tz^{n+1}_{i,j-\frac{1}{2}} = c_1\pi \left(r^2_{i+\frac{1}{2}} - r^2_{i-\frac{1}{2}} \right) \left(\frac{1}{z_j - z_{j-1}} \right) 4k_{z^{n+1}_{i,j-\frac{1}{2}}} \left[\frac{\delta^{n+1}_{z_{i,j-\frac{1}{2}}}}{\left(B_{i,j}+B_{i,j-1}\right)\left(\mu_{i,j}+\mu_{i,j-1}\right)} \right] \quad \textbf{(3.39)}$$

Derivative of Eq. 3.33 with respect to the gridblock pressure at (r_i, z_j) is given by:

$$\frac{\partial Tz^{n+1}_{i,j-\frac{1}{2}}}{\partial p^{n+1}_{i,j}} = c_1\pi \left(r^2_{i+\frac{1}{2}} - r^2_{i-\frac{1}{2}} \right) \left(\frac{1}{z_j - z_{j-1}} \right) 4k_{z^{n+1}_{i,j-\frac{1}{2}}} \left(\frac{\frac{\partial \delta^{n+1}_{z_{i,j-\frac{1}{2}}}}{\partial p^{n+1}_{i,j}}}{\left(B_{i,j}+B_{i,j-1}\right)\left(\mu_{i,j}+\mu_{i,j-1}\right)} \right.$$

$$\left. \left. - \frac{\delta^{n+1}_{z_{i,j-\frac{1}{2}}} \left[\left(\frac{\partial B_{i,j}}{\partial p^{n+1}_{i,j}} \mu_{i,j} + B_{i,j} \frac{\partial \mu_{i,j}}{\partial p^{n+1}_{i,j}} \right) + \left(\frac{\partial B_{i,j}}{\partial p^{n+1}_{i,j}} \mu_{i,j-1} \right) + \left(B_{i,j-1} \frac{\partial \mu_{i,j}}{\partial p^{n+1}_{i,j}} \right) \right]}{\left[\left(B_{i,j}+B_{i,j-1}\right)\left(\mu_{i,j}+\mu_{i,j-1}\right) \right]^2} \right) \right) \quad \textbf{(3.40)}$$

Derivative of Eq. 3.33 with respect to the gridblock pressure at (r_i, z_{j-1}) is given by:

$$\frac{\partial Tz^{n+1}_{i,j-\frac{1}{2}}}{\partial p^{n+1}_{i,j-1}} = c_1\pi\left(r^2_{i+\frac{1}{2}} - r^2_{i-\frac{1}{2}}\right)\left(\frac{1}{z_j - z_{j-1}}\right)4k^{n+1}_{z_{i,j-\frac{1}{2}}}\left\{\frac{\frac{\partial \delta^{n+1}_{z_{i,j-\frac{1}{2}}}}{\partial p^{n+1}_{i,j-1}}}{\left(B_{i,j}+B_{i,j-1}\right)\left(\mu_{i,j}+\mu_{i,j-1}\right)}\right.$$

$$\left. - \frac{\delta^{n+1}_{z_{i,j-\frac{1}{2}}}\left[\left(B_{i,j}\frac{\partial \mu_{i,j-1}}{\partial p^{n+1}_{i,j-1}}\right)+\left(\frac{\partial B_{i,j-1}}{\partial p^{n+1}_{i,j-1}}\mu_{i,j}\right)+\left(\frac{\partial B_{i,j-1}}{\partial p^{n+1}_{i,j-1}}\mu_{i,j-1}+B_{i,j-1}\frac{\partial \mu_{i,j-1}}{\partial p^{n+1}_{i,j-1,}}\right)\right]}{\left[\left(B_{i,j}+B_{i,j-1}\right)\left(\mu_{i,j}+\mu_{i,j-1}\right)\right]^2}\right\} \quad \textbf{(3.41)}$$

Using Eq. 2.78b in Eq. 2.57b gives the transmissibility term which is required to compute for Eq. 2.29d:

$$Tz^{n+1}_{i,j+\frac{1}{2}} = c_1\pi\left(r^2_{i+\frac{1}{2}} - r^2_{i-\frac{1}{2}}\right)\left(\frac{1}{z_{j+1} - z_j}\right)4k^{n+1}_{z_{i,j+\frac{1}{2}}}\left[\frac{\delta^{n+1}_{z_{i,j+\frac{1}{2}}}}{\left(B_{i,j+1}+B_{i,j}\right)\left(\mu_{i,j+1}+\mu_{i,j}\right)}\right] \quad \textbf{(3.42)}$$

Derivative of Eq. 3.33 with respect to the gridblock pressure at (r_i, z_j) is given by:

$$\frac{\partial Tz^{n+1}_{i,j+\frac{1}{2}}}{\partial p^{n+1}_{i,j}} = c_1\pi\left(r^2_{i+\frac{1}{2}} - r^2_{i-\frac{1}{2}}\right)\left(\frac{1}{z_{j+1} - z_j}\right)4k^{n+1}_{z_{i,j+\frac{1}{2}}}\left\{\frac{\frac{\partial \delta^{n+1}_{z_{i,j+\frac{1}{2}}}}{\partial p^{n+1}_{i,j}}}{\left(B_{i,j+1}+B_{i,j}\right)\left(\mu_{i,j+1}+\mu_{i,j}\right)}\right.$$

$$\left. - \frac{\delta^{n+1}_{z_{i,j+\frac{1}{2}}}\left[\left(B_{i,j+1}\frac{\partial \mu_{i,j}}{\partial p^{n+1}_{i,j}}\right)+\left(\frac{\partial B_{i,j}}{\partial p^{n+1}_{i,j}}\mu_{i,j+1}\right)+\left(\frac{\partial B_{i,j}}{\partial p^{n+1}_{i,j}}\mu_{i,j}+B_{i,j}\frac{\partial \mu_{i,j}}{\partial p^{n+1}_{i,j}}\right)\right]}{\left[\left(B_{i,j+1}+B_{i,j}\right)\left(\mu_{i,j+1}+\mu_{i,j}\right)\right]^2}\right\} \quad \textbf{(3.43)}$$

Derivative of Eq. 3.33 with respect to the gridblock pressure at (r_i, z_{j+1}) is given by:

$$\frac{\partial Tz^{n+1}_{i,j+\frac{1}{2}}}{\partial p^{n+1}_{i,j+1}} = c_1\pi\left(r^2_{i+\frac{1}{2}} - r^2_{i-\frac{1}{2}}\right)\left(\frac{1}{z_{j+1}-z_j}\right)4k^{n+1}_{z_{i,j+\frac{1}{2}}}\left(\frac{\frac{\partial \delta^{n+1}_{z_{i,j+\frac{1}{2}}}}{\partial p^{n+1}_{i,j+1}}}{\left(B_{i,j+1}+B_{i,j}\right)\left(\mu_{i,j+1}+\mu_{i,j}\right)}\right.$$

$$\left. - \frac{\delta^{n+1}_{z_{i,j+\frac{1}{2}}}\left[\left(\frac{\partial B_{i,j+1}}{\partial p^{n+1}_{i,j+1}}\mu_{i,j+1} + B_{i,j+1}\frac{\partial \mu_{i,j+1}}{\partial p^{n+1}_{i,j+1}}\right) + \left(\frac{\partial B_{i,j+1}}{\partial p^{n+1}_{i,j+1}}\mu_{i,j}\right) + \left(B_{i,j}\frac{\partial \mu_{i,j+1}}{\partial p^{n+1}_{i,j+1}}\right)\right]}{\left[\left(B_{i,j+1}+B_{i,j}\right)\left(\mu_{i,j+1}+\mu_{i,j}\right)\right]^2}\right) \quad \textbf{(3.44)}$$

We will again evaluate the correction factor only in *r*-direction defined by Eq. 2.87. Recalling Eq. 2.87 and taking derivative of correction factor with respect to $p^{n+1}_{i,j}$ in *r*-direction yields, when $p^{n+1}_{i+1,j} > p^{n+1}_{i,j}$:

$$\frac{\partial \delta^{n+1}_{r_{i+\frac{1}{2},j}}}{\partial p^{n+1}_{i,j}} = \frac{4\left(\sqrt{1+4\hat{\gamma}^{n+1}_{r_{i+\frac{1}{2},j}}\left|\frac{p^{n+1}_{i+1,j}-p^{n+1}_{i,j}}{r_{i+1}-r_i}\right|}+1\right)^{-2}}{\sqrt{1+4\hat{\gamma}^{n+1}_{r_{i+\frac{1}{2},j}}\left|\frac{p^{n+1}_{i+1,j}-p^{n+1}_{i,j}}{r_{i+1}-r_i}\right|}}\left(\frac{\partial \hat{\gamma}^{n+1}_{r_{i+\frac{1}{2},j}}}{\partial p^{n+1}_{i,j}}\left|\frac{p^{n+1}_{i+1,j}-p^{n+1}_{i,j}}{r_{i+1}-r_i}\right| - \frac{\hat{\gamma}^{n+1}_{r_{i+\frac{1}{2},j}}}{r_{i+1}-r_i}\right) \quad \textbf{(3.45)}$$

when $p^{n+1}_{i+1,j} < p^{n+1}_{i,j}$:

$$\frac{\partial \delta^{n+1}_{r_{i+\frac{1}{2},j}}}{\partial p^{n+1}_{i,j}} = \frac{4\left(\sqrt{1+4\hat{\gamma}^{n+1}_{r_{i+\frac{1}{2},j}}\left|\frac{p^{n+1}_{i+1,j}-p^{n+1}_{i,j}}{r_{i+1}-r_i}\right|}+1\right)^{-2}}{\sqrt{1+4\hat{\gamma}^{n+1}_{r_{i+\frac{1}{2},j}}\left|\frac{p^{n+1}_{i+1,j}-p^{n+1}_{i,j}}{r_{i+1}-r_i}\right|}}\left(\frac{\partial \hat{\gamma}^{n+1}_{r_{i+\frac{1}{2},j}}}{\partial p^{n+1}_{i,j}}\left|\frac{p^{n+1}_{i+1,j}-p^{n+1}_{i,j}}{r_{i+1}-r_i}\right| + \frac{\hat{\gamma}^{n+1}_{r_{i+\frac{1}{2},j}}}{r_{i+1}-r_i}\right) \quad \textbf{(3.46)}$$

Recalling Eq. 2.89 in order to use in Eqs. 3.45 and 3.46 yields:

$$\hat{\gamma}_{r_{i+\frac{1}{2},j}}^{n+1} = \left(1.157795\times10^{-15}\right)\beta_r k_{r_{i+\frac{1}{2},j}}^{2}\frac{\frac{\partial\rho_{i+\frac{1}{2},j}^{n+1}}{\partial p_{i,j}^{n+1}}\left(\mu_{i+\frac{1}{2},j}^{n+1}\right)^2 + 2\rho_{i+\frac{1}{2},j}^{n+1}\mu_{i+\frac{1}{2},j}^{n+1}\frac{\partial\mu_{i+\frac{1}{2},j}^{n+1}}{\partial p_{i,j}^{n+1}}}{\left(\mu_{i+\frac{1}{2},j}^{n+1}\right)^4} \tag{3.47}$$

Correction factor in *r*-direction expressed in Eq. 2.87 has a non-zero derivative term with respect to $p_{i+1,j}^{n+1}$. Recalling Eq. 2.87 and taking derivative of correction factor with respect to $p_{i+1,j}^{n+1}$ in *r*-direction yields, when $p_{i+1,j}^{n+1} > p_{i,j}^{n+1}$:

$$\frac{\partial\delta_{r_{i+\frac{1}{2},j}}^{n+1}}{\partial p_{i+1,j}^{n+1}} = \frac{4\left(\sqrt{1+4\hat{\gamma}_{r_{i+\frac{1}{2},j}}^{n+1}\left|\frac{p_{i+1,j}^{n+1}-p_{i,j}^{n+1}}{r_{i+1}-r_i}\right|}+1\right)^{-2}}{\sqrt{1+4\hat{\gamma}_{r_{i+\frac{1}{2},j}}^{n+1}\left|\frac{p_{i+1,j}^{n+1}-p_{i,j}^{n+1}}{r_{i+1}-r_i}\right|}}\left(\frac{\partial\hat{\gamma}_{r_{i+\frac{1}{2},j}}^{n+1}}{\partial p_{i+1,j}^{n+1}}\left|\frac{p_{i+1,j}^{n+1}-p_{i,j}^{n+1}}{r_{i+1}-r_i}\right| + \frac{\hat{\gamma}_{r_{i+\frac{1}{2},j}}^{n+1}}{r_{i+1}-r_i}\right) \tag{3.48}$$

when $p_{i+1,j}^{n+1} < p_{i,j}^{n+1}$:

$$\frac{\partial\delta_{r_{i+\frac{1}{2},j}}^{n+1}}{\partial p_{i+1,j}^{n+1}} = \frac{4\left(\sqrt{1+4\hat{\gamma}_{r_{i+\frac{1}{2},j}}^{n+1}\left|\frac{p_{i+1,j}^{n+1}-p_{i,j}^{n+1}}{r_{i+1}-r_i}\right|}+1\right)^{-2}}{\sqrt{1+4\hat{\gamma}_{r_{i+\frac{1}{2},j}}^{n+1}\left|\frac{p_{i+1,j}^{n+1}-p_{i,j}^{n+1}}{r_{i+1}-r_i}\right|}}\left(\frac{\partial\hat{\gamma}_{r_{i+\frac{1}{2},j}}^{n+1}}{\partial p_{i+1,j}^{n+1}}\left|\frac{p_{i+1,j}^{n+1}-p_{i,j}^{n+1}}{r_{i+1}-r_i}\right| - \frac{\hat{\gamma}_{r_{i+\frac{1}{2},j}}^{n+1}}{r_{i+1}-r_i}\right) \tag{3.49}$$

Recalling Eq. 2.89 in order to use in Eqs. 3.48 and 3.49 yields:

$$\hat{\gamma}_{r_{i+\frac{1}{2},j}}^{n+1} = \left(1.157795\times10^{-15}\right)\beta_r k_{r_{i+\frac{1}{2},j}}^{2}\frac{\frac{\partial\rho_{i+\frac{1}{2},j}^{n+1}}{\partial p_{i+1,j}^{n+1}}\left(\mu_{i+\frac{1}{2},j}^{n+1}\right)^2 + 2\rho_{i+\frac{1}{2},j}^{n+1}\mu_{i+\frac{1}{2},j}^{n+1}\frac{\partial\mu_{i+\frac{1}{2},j}^{n+1}}{\partial p_{i+1,j}^{n+1}}}{\left(\mu_{i+\frac{1}{2},j}^{n+1}\right)^4} \tag{3.50}$$

The derivatives of the correction term in the *z*-direction with respect to pressures are computed from the same expressions, Eqs. 3.45-3.50 given for the *r*-direction just by replacing the subscript *r* by *z*.

Formation volume factor, density and viscosity derivative terms with respect to pressure are discussed in Appendix B.

3.1.2.2 Numerical approach for derivatives

The approximation of derivatives in Eq. 3.26 by finite differences plays a significant role for the numerical solution of differential equations, especially boundary value problems. In the numerical solution of Eq. 3.26, derivatives are considered with forward difference method while the spacing h_s is considered as constant in our application. All derivative terms in the matrix for one gridblock with dummy index as (i,j) are calculated for i=1,2,…,N and j=1,2,…,M as follows:

$$\frac{\partial f_{i,j}}{\partial p_{i,j}^{n+1}} = \frac{f_{i,j}\left(p_{i,j}^{n+1} + h_s\right) - f_{i,j}\left(p_{i,j}^{n+1}\right)}{h_s} \tag{3.51a}$$

$$\frac{\partial f_{i,j}}{\partial P_{i-1,j}^{n+1}} = \frac{f_{i,j}\left(P_{i-1,j}^{n+1} + h_s\right) - f_{i,j}\left(P_{i-1,j}^{n+1}\right)}{h_s} \tag{3.51b}$$

$$\frac{\partial f_{i,j}}{\partial p_{i+1,j}^{n+1}} = \frac{f_{i,j}\left(p_{i+1,j}^{n+1} + h_s\right) - f_{i,j}\left(p_{i+1,j}^{n+1}\right)}{h_s} \tag{3.51c}$$

$$\frac{\partial f_{i,j}}{\partial p_{i,j-1}^{n+1}} = \frac{f_{i,j}\left(p_{i,j-1}^{n+1} + h_s\right) - f_{i,j}\left(p_{i,j-1}^{n+1}\right)}{h_s} \tag{3.51d}$$

$$\frac{\partial f_{i,j}}{\partial p_{i,j+1}^{n+1}} = \frac{f_{i,j}\left(p_{i,j+1}^{n+1} + h_s\right) - f_{i,j}\left(p_{i,j+1}^{n+1}\right)}{h_s} \tag{3.51e}$$

Furthermore, numerical solution can work depend on the choice of h_s even if the finite difference scheme is consistent. The stability condition is a requirement that the error in the computed solution would be amplified in the subsequent computations. Our experiments not shown here with the derivatives of pressure dependent terms such as viscosity, formation volume factor, and gas compressibility, etc., indicate that only the calculation of derivative of gas compressibility with

respect to pressure brings restriction for choosing the value of perturbation h_s. As can be seen in **Figure 3.1** in which temperature is 212^oF and specific gravity of the gas is 0.7, the derivative of gas compressibility shows oscillatory behavior if h_s is chosen 'too' small, but if h_s is greater than 1×10^{-4}, then these oscillations do not exist.

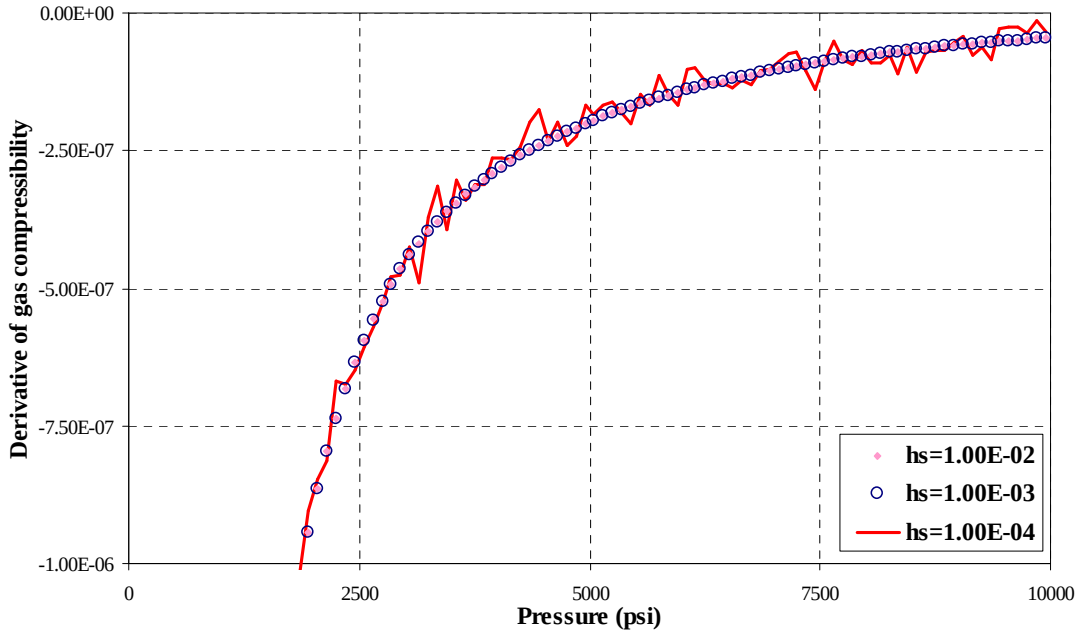

Figure 3.3 : Investigation on the stability of derivative of gas compressibility.

3.1.3 Matrix solver

In the Newton method, we solve the matrix problem given by Eq. 3.23. Here, the Jacobian matrix arising from our model is a sparse matrix. A sparse matrix is defined as a matrix having non-zero terms far exceeding than the number of zero terms. It is also important to note the Jacobian matrix for our problem (see the matrix given by Eq. 3.26) is non-symmetric. So, solving the matrix problem arising from the Newton method efficiently requires special matrix solvers. One of the efficient matrix solvers that can be used is the Yale Nonsymmetric Sparse Matrix Codes (Eisenstat, 1979). The Yale code is a direct solution of the system of equations. The nonsymmetric Yale code includes three driver subroutines by which a system of linear equations having a nonsymmetric sparse coefficient matrix can be solved. It is mentioned that the driver NDRV is designed for speed, the driver TDRV emphasizes storage economy, and finally the driver CDRV attempts to balance the goals of speed and storage economy. Note that this code was developed in 1968 when the computer technology was not improved as much as it is right now. Since storage economy is

not a critical concern at the moment, NDRV is implemented in the simulator while all of the drivers were tested in the Chapter 4 in a verification case. In the reference, there is another subroutine called as ODRV suggested to be used prior to running of the main three drivers whereas the code is not provided. Also, for all NW cases run in this study, we used ODRV first for ordering and then NDRV, TDRV, or CDRV codes. ODRV is an ordering driver. The coding may be found in another reference of Yale Symmetric Sparse Matrix Codes (Eisenstat, 1979). It reorders the rows and columns of the original matrix. This is primarily done to reduce fill-in. The reordering of the matrix need only be done once, since the nonzero-zero structure is the same for all the subsequent iterations and time steps. Our experiments with the nonsymmetric Yale code as implemented in our simulator can handle a matrix size of 250,000×250,000.

We also considered an iterative solver called as LINBCG (Press et al., 2010) which is a biconjugate gradient solution of sparse systems uses preconditioners. Our limited experiments with this solver indicate that it is not as efficient as the Yale nonsymmetric code if a preconditioner is not used. We did not consider using preconditioning matrix to speed up the computations by LINBCG. Also, this routine uses an indexed storage scheme to avoid storing zeros of the matrix.

3.2 Functional Iteration Method

Unlike the Newton method, the functional iteration method does not require the computation of derivatives of the residual equations to compute the unknown pressures and hence, it is less computationally expensive. Furthermore, the matrix problem arising from the functional iteration method is a symmetric one, compared to the nonsymmetric matrix in the Newton method. The functional iteration method is described below.

3.2.1 Brief description

It is a simple method as it solves the reservoir and well equations iteratively from time step t^n to t^{n+1} by starting with an initial guess at t^n and then by updating the pressures and the pressure dependent terms until we achieve convergence in pressures. Recalling Eq. 2.88,

$$p_{i,j-1}^{n+1,l+1}\left(T_{i,j-\frac{1}{2}}^{n+1,l}\right)+p_{i-1,j}^{n+1,l+1}\left(T_{i-\frac{1}{2},j}^{n+1,l}\right)+p_{i+1,j}^{n+1,l+1}\left(T_{i+\frac{1}{2},j}^{n+1,l}\right)+p_{i,j+1}^{n+1,l+1}\left(T_{i,j+\frac{1}{2}}^{n+1,l}\right)$$
$$+p_{i,j}^{n+1,l+1}\left(-T_{i,j-\frac{1}{2}}^{n+1,l}-T_{i,j+\frac{1}{2}}^{n+1,l}-T_{i-\frac{1}{2},j}^{n+1,l}-T_{i+\frac{1}{2},j}^{n+1,l}-V_{i,j}^{n+1,l}\right)=-V_{i,j}^{n+1,l}p_{i,j}^{n} \quad \textbf{(3.52)}$$

where $p_{i,j}^{n+1,l+1}$ is the (l+1)st approximation to $p_{i,j}^{n+1}$. We wish to have $p_{i,j}^{n+1,l+1}$ converge to $p_{i,j}^{n+1}$ within the following two converge criteria for i=1,2,…,N and j=1,2,…,M as well as p_{wf}^{n+1}.

Converge criteria 1: $\in$ = 0.1 or 1

$$\max\left|p_{i,j}^{n+1,l+1}-p_{i,j}^{n+1,l}\right|\leq\in \quad \textbf{(3.53)}$$

Converge criteria 2: φ = 0.0001

$$\max\left|\frac{p_{i,j}^{n+1,l+1}-p_{i,j}^{n+1,l}}{p_{i,j}^{n+1,l+1}+10^{-13}}\right|\leq\varphi \quad \textbf{(3.54)}$$

This method may require much iteration in case large steps are taken and if the problem is highly non-linear.

3.2.2 Matrix problem

In the functional iteration method, we solve the following matrix-vector equation:

$$\mathbf{A}^{n+1,l}\mathbf{p}^{n+1,l+1}=\mathbf{d}^{n,l} \quad \textbf{(3.55)}$$

where l represents the iteration index for the time level, t^{n+1}. In this method, once we solve pressures at t^n, then we set $\mathbf{p}^{n+1,l}$=$\mathbf{p}^n$ and then update the matrix **A** and the right hand side vector **d** with this pressure vector and then solve Eq. 3.55 for $\mathbf{p}^{n+1,l+1}$. Then, the solutions $\mathbf{p}^{n+1,l+1}$ and $\mathbf{p}^{n+1,l}$ are compared until convergence. The right hand side vector is illustrated as:

$$\mathbf{d}^{n,l} = \begin{pmatrix} -p_{1,1}^{n} V_{1,1}^{n+1,l} \\ -p_{2,1}^{n} V_{2,1}^{n+1,l} \\ -p_{3,1}^{n} V_{3,1}^{n+1,l} \\ -p_{1,2}^{n} V_{1,2}^{n+1,l} \\ -p_{2,2}^{n} V_{2,2}^{n+1,l} \\ -p_{3,2}^{n} V_{3,2}^{n+1,l} \\ -p_{1,3}^{n} V_{1,3}^{n+1,l} \\ -p_{2,3}^{n} V_{2,3}^{n+1,l} \\ -p_{3,3}^{n} V_{3,3}^{n+1,l} \\ q_{sc}^{n+1} - C_{ws}^{n+1,l} p_{wf}^{n} \end{pmatrix} \quad \textbf{(3.56)}$$

The solution matrix will be as:

$$\mathbf{p}_{i,j}^{n+1,l+1} = \begin{pmatrix} p_{1,1}^{n+1,l+1} \\ p_{2,1}^{n+1,l+1} \\ p_{3,1}^{n+1,l+1} \\ p_{1,2}^{n+1,l+1} \\ p_{2,2}^{n+1,l+1} \\ p_{3,2}^{n+1,l+1} \\ p_{1,3}^{n+1,l+1} \\ p_{2,3}^{n+1,l+1} \\ p_{3,3}^{n+1,l+1} \\ p_{wf}^{n+1,l+1} \end{pmatrix} \quad \textbf{(3.57)}$$

The coefficient matrix arising from finite difference formulation can be represented as in Eq. 3.58 and it can directly be implemented into the code. Note that for simplification in presenting the matrix in Eq. 3.58, a new transmissibility term which is the sum of each transmissibility term in all directions, using dummy index (*i,j*) is introduced as:

$$\sum T_{i,j}^{n+1,l} = Tr_{i-\frac{1}{2},j}^{n+1,l} + Tr_{i+\frac{1}{2},j}^{n+1,l} + Tz_{i,j-\frac{1}{2}}^{n+1,l} + Tz_{i,j+\frac{1}{2}}^{n+1,l} \quad \textbf{(3.58)}$$

$$\mathbf{A} = \begin{pmatrix}
-\sum T_{1,1}^{n+1,l} - V_{1,1}^{n+1,l} & Tr_{\frac{3}{2},1}^{n+1,l} & 0 & Tz_{1,\frac{3}{2}}^{n+1,l} & 0 & 0 & 0 & 0 & 0 & Tr_{\frac{1}{2},1}^{n+1,l} \\
Tr_{\frac{3}{2},1}^{n+1,l} & -\sum T_{2,1}^{n+1,l} - V_{2,1}^{n+1,l} & Tr_{\frac{5}{2},1}^{n+1,l} & 0 & Tz_{2,\frac{3}{2}}^{n+1,l} & 0 & 0 & 0 & 0 & 0 \\
0 & Tr_{\frac{5}{2},1}^{n+1,l} & -\sum T_{3,1}^{n+1,l} - V_{3,1}^{n+1,l} & 0 & 0 & Tz_{3,\frac{3}{2}}^{n+1,l} & 0 & 0 & 0 & 0 \\
Tz_{1,\frac{3}{2}}^{n+1,l} & 0 & 0 & -\sum T_{1,2}^{n+1,l} - V_{1,2}^{n+1,l} & Tr_{\frac{3}{2},2}^{n+1,l} & 0 & Tz_{1,\frac{5}{2}}^{n+1,l} & 0 & 0 & Tr_{\frac{1}{2},2}^{n+1,l} \\
0 & Tz_{2,\frac{3}{2}}^{n+1,l} & 0 & Tr_{\frac{3}{2},2}^{n+1,l} & -\sum T_{2,2}^{n+1,l} - V_{2,2}^{n+1,l} & Tr_{\frac{5}{2},2}^{n+1,l} & 0 & Tz_{i,\,j+\frac{1}{2}}^{n+1,l} & 0 & 0 \\
0 & 0 & Tz_{3,\frac{3}{2}}^{n+1,l} & 0 & Tr_{\frac{5}{2},2}^{n+1,l} & -\sum T_{3,2}^{n+1,l} - V_{3,2}^{n+1,l} & 0 & 0 & Tz_{3,\frac{5}{2}}^{n+1,l} & 0 \\
0 & 0 & 0 & Tz_{1,\frac{5}{2}}^{n+1,l} & 0 & 0 & -\sum T_{1,3}^{n+1,l} - V_{1,3}^{n+1,l} & Tr_{\frac{3}{2},3}^{n+1,l} & 0 & Tr_{\frac{1}{2},3}^{n+1,l} \\
0 & 0 & 0 & 0 & Tz_{2,\frac{5}{2}}^{n+1,l} & 0 & Tr_{\frac{3}{2},3}^{n+1,l} & -\sum T_{2,3}^{n+1,l} - V_{2,3}^{n+1,l} & Tr_{\frac{5}{2},3}^{n+1,l} & 0 \\
0 & 0 & 0 & 0 & 0 & Tz_{3,\frac{5}{2}}^{n+1,l} & 0 & Tr_{\frac{5}{2},3}^{n+1,l} & -\sum T_{3,3}^{n+1,l} - V_{3,3}^{n+1,l} & 0 \\
Tr_{\frac{1}{2},1}^{n+1,l} & 0 & 0 & Tr_{\frac{1}{2},2}^{n+1,l} & 0 & 0 & Tr_{\frac{1}{2},3}^{n+1,l} & 0 & 0 & C_{ws}^{n+1,l} - \sum_{j=1}^{j=M} Tr_{\frac{1}{2},j}^{n+1,l}
\end{pmatrix}$$

(3.59)

3.2.3 Matrix solver

The matrix obtained by using this method (see Eq. 3.59) will yield a symmetric matrix. There are two different algorithms used to solve this problem, Symmetric Strongly Implicit Procedure (SSIP) of Welty and Meijerink (1981) and the SDRV (a solution driver) for Yale Symmetric Sparse Matrix Codes (Eisenstat, 1979). SSIP is an iterative solver, whereas the Yale is a direct solver. SSIP performs iteration to achieve solutions at a given time and require less storage compared to the Yale for large sized matrix problems. So, in very large sized matrix problems, SSIP is expected to find solution faster than the Yale. However, our experiments show that Yale symmetric code is even faster than SSIP for large sized matrix problems. The only problem with Yale we found is that we could not run Yale for matrix sizes larger than 250,000×250,000 due to memory (storage) problems. Therefore, takes more time to achieve solutions. However, in very large matrix problems, SSIP is expected to find solution faster than SDRV which is an indirect solver. Also, for all FIT cases run in this study, we used ODRV first for ordering and then SDRV codes.

4. VERIFICATION OF THE SIMULATOR

In this chapter, several different well/reservoir systems are considered to perform the verification of simulator, and also to test the capabilities of the simulator developed. The results obtained from the simulator is compared with those obtained from the analytical solutions as well as the numerical solutions based on Voronoi grids of ECRIN (2009) developed by Kappa Engineering for a single production or injection well in the center of a cylindrical reservoir with a specified constant surface flow rate for both fully penetrating and limited-entry vertical wells producing from homogeneous isotropic and anisotropic reservoir. Boundary conditions are already discussed in Chapter 2. For the verification purposes, different test sequences which contain either drawdown and buildup, or injection and falloff periods are considered. Input data for all cases considered in this chapter given in Table 4.1 unless otherwise specified.

Table 4.1 : Input parameters for verification tests.

Parameters	Values
r_w (ft)	0.3
r_e (ft)	750
h (ft)	30
p_i (psi)	5000
T (^{o}F)	212
Gas gravity	0.7
$k_r = k_z$ (mD)	30
First time step (Days)	1×10^{-4}
c_r (psi^{-1})	3.0×10^{-6}
ϕ (fraction)	0.1

For the first four cases where we simulate a drawdown (DD) period followed by buildup (BU) period, the total duration of the simulation is 20 hr, as can be seen from **Figure 4.1**. The duration of the drawdown period is 10 hr, the duration of the buildup period is 10 hr. Flow rate during the drawdown period is 5000 *MSCF/D*.

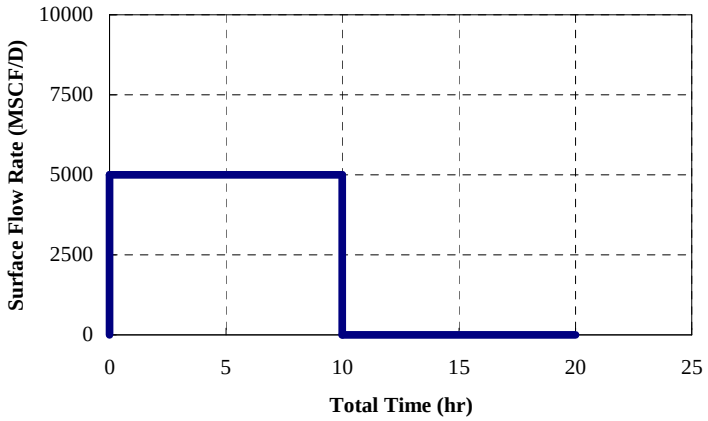

Figure 4.1 : Flow rate history at the tested well, verification tests.

For each flow period, uniformly spaced time points are used by the logarithmic sampling of the time interval for computing flowing bottomhole pressure at the well. As mentioned earlier, ECRIN evaluates both wellbore storage and non-Darcy flow coefficients as constant values in its calculations during simulation. Although this may not be realistic, all cases considered in this chapter also use ECRIN's way as an option provided in the simulator for verification purposes if not otherwise stated in the description of each case. Note that throughout the verification and application cases, in all log-log plots, pressure and pressure derivatives refer to real gas pseudo pressures and its Bourdet's derivatives.

4.1 Case 1: Full Penetration

The first case is for a fully penetrating vertical well ignoring wellbore storage, skin and non-Darcy flow effects producing at specified constant surface flow rate in a homogeneous and isotropic single-layer reservoir described in Table 4.1. The model designed in simulator uses structured, uniform block centered grid system with 10000 gridblocks in *r*-direction (**Figure 4.2)** and 1 gridblock in *z*-direction whereas ECRIN uses 727 automatically generated voronoid grids shown in **Figure 4.3**. Since this is a homogeneous isotropic and single-layer case, both simulator and ECRIN do not create more than one gridblock in *z*-direction. **Figure 4.4** and **Figure 4.5** show the comparison of the pressure change and its Bourdet's derivative (Bourdet et al., 1989) for drawdown and buildup periods respectively obtained from the analytical and numerical solution methods in ECRIN and from the simulator for the grid system of N=10000 and M=1. Boundary effects (or pseudo-steady state flow) can be clearly

seen from the plot (**Figure. 4.3**) as the derivative curve's slope becomes unity while reaching the end of production period. Boundary effects are representing with minus one slope on the derivative curve during buildup period.

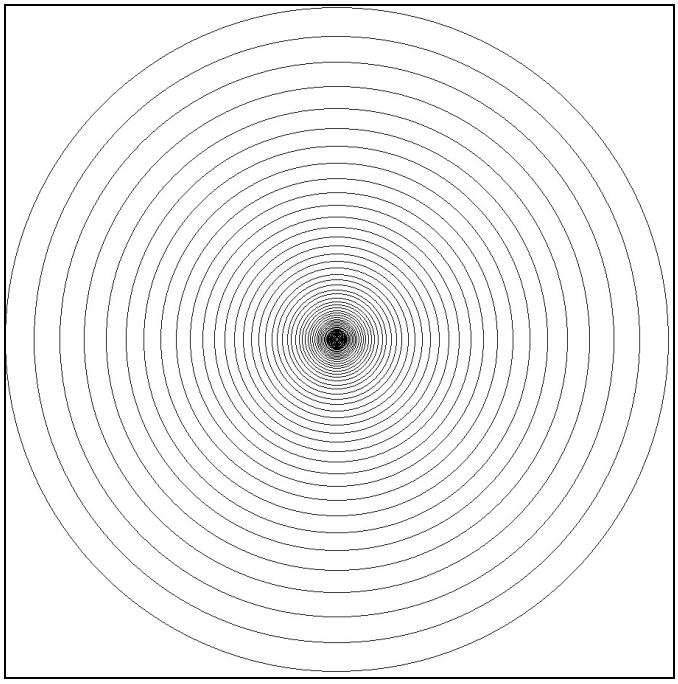

Figure 4.2 : Areal Coat's grids of simulator.

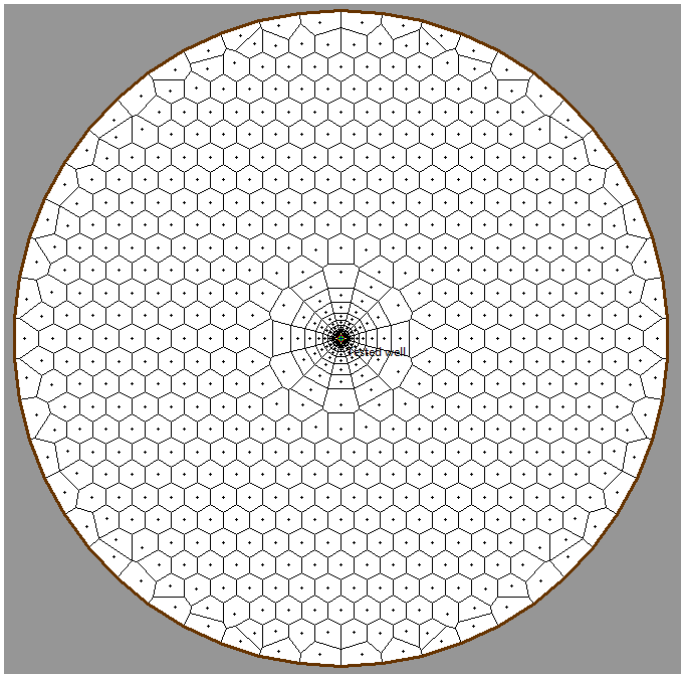

Figure 4.3 : Areal Voronoi grids of ECRIN used for full penetration well.

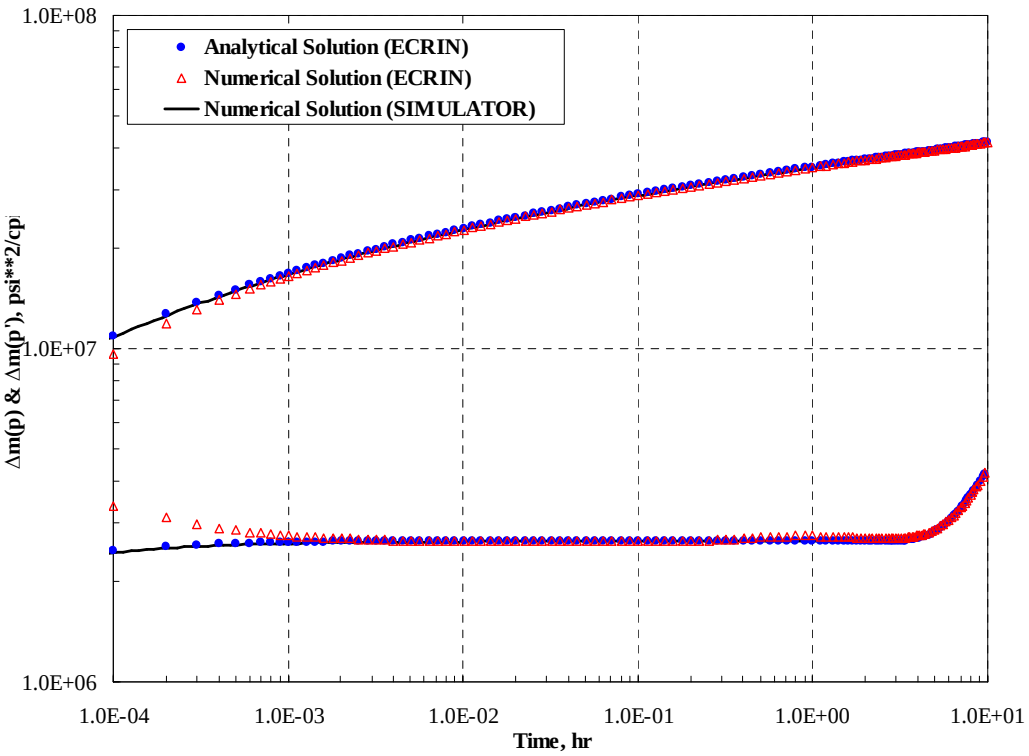

Figure 4.4 : Comparison of results, DD, full penetration.

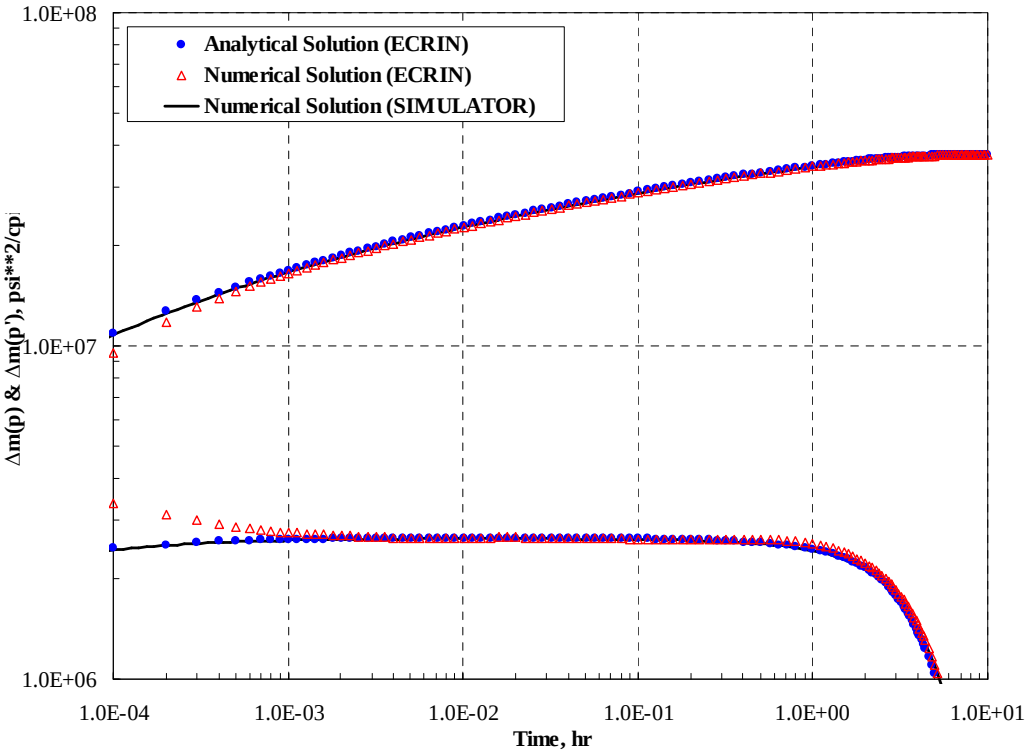

Figure 4.5 : Comparison of results, BU, full penetration.

Analytical and numerical solutions from ECRIN and the simulator yield almost identical pressure responses throughout the simulation for both periods as expected.

However, numerical solution from ECRIN does not provide accurate pressure derivative responses in the time interval from 0.0001 to 0.001 hours when compared to corresponding responses generated from the analytical solution. This behaviour is mainly due to either the effect of grid system used in ECRIN (**Figure 4.3**) or the different treatments of infinite-conductivity wellbore assumption used in numerical simulators.

All log-log plots in this chapter having the legend called as numerical solution of simulator represent the solution from the functional iteration technique (FIT) discussed in the previous chapter. We compared the solutions obtained from the FIT with the Newton (NW) method. The grid system considered is N=10000 and M=1. **Figure 4.6** shows a comparison of the pressure versus time data for the entire duration of the drawdown and buildup periods for both the FIT and NW methods with analytical and numerical approaches). As can be seen, FIT and NW methods provide almost identical pressures. The CPU times used to obtain the solutions from FIT and NW method with analytical and numerical approaches were 199 seconds, 201 seconds, and 206 seconds, respectively. We should note that we use the same time steps to compute pressures for both methods. Clearly, for this example, NW method does not provide any advantage over the FIT. Moreover, the NW methods take slightly more computational times compared to FIT. For the example case considered, FIT and NW methods provide the same results for each time step point up to five decimal digits at the end of production and up to seven decimal digits at the end of buildup. Both methods yield identical pressure derivatives as well although not shown here.

In comparison with Ecrin, at the end of production and buildup periods, respectively, pressure differences are 0.7 psi and 0.001 psi. In order to further improve the solution, the effect of number of gridblocks used in the simulation is investigated. Therefore, the same system is simulated with 100000 gridblocks in *r*-direction and 1 gridblock in *z*-direction and tabulated results in Table 4.2.

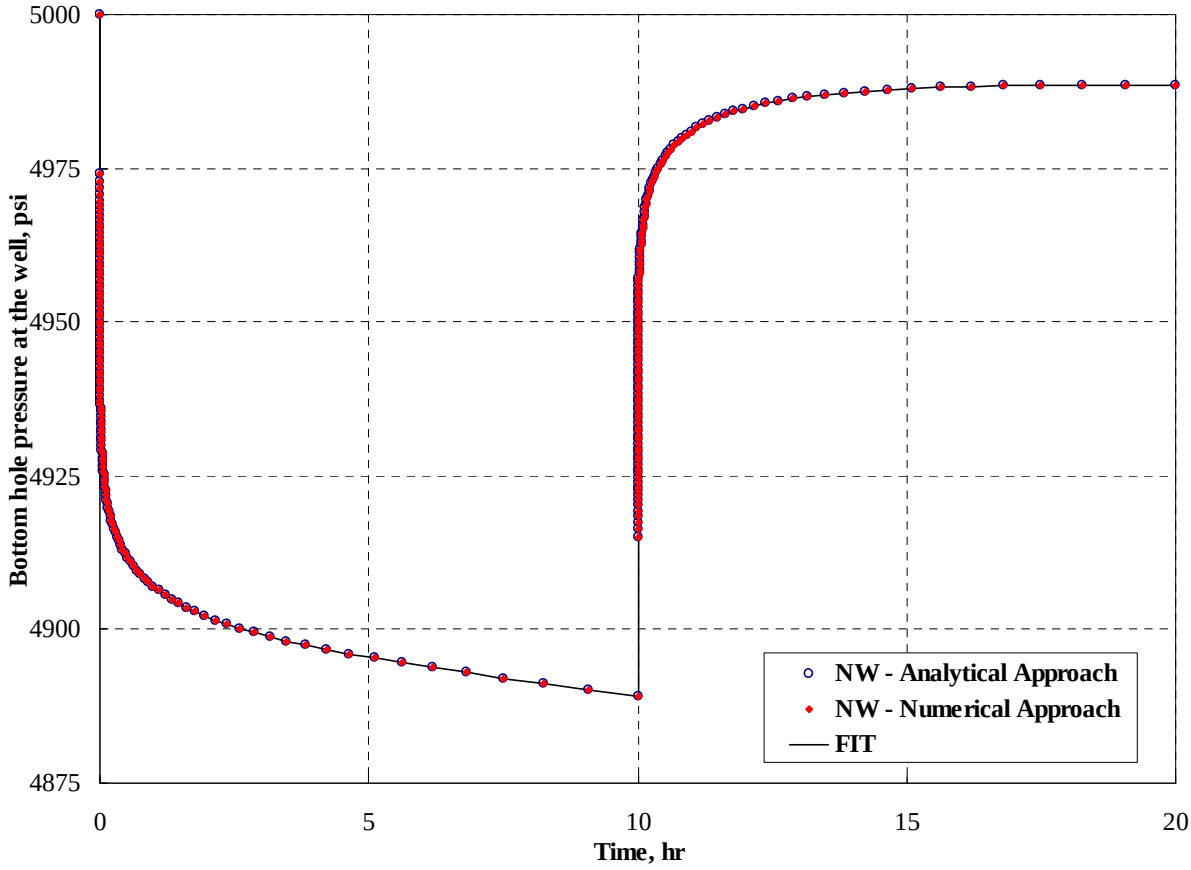

Figure 4.6 : Comparison of pressures for the entire flow rate history, case #1.

From the results given in Table 4.2, it seems that chosen value for the number of gridblocks to simulate the system is sufficiently reasonable since pressure responses as well as the derivatives do not improve considerably well for the case considered. Thus, simulation on such a grid would be neither practical nor feasible due to both computational time and storage requirements.

Table 4.2 : Comparison of results, full penetration.

Number of Gridblocks used in *r*-direction and *z*-direction respectively	At end of production	At end of buildup
10000×1	4889.170	4991.557
100000×1	4889.166	4991.561
Analytical Solution (ECRIN)	4889.128	4988.598

4.2 Case 2: Limited-Entry

The accuracy and gridding issues for a single limited-entry well case are investigated in this case. The reservoir (Table 4.1), flow rate history (**Figure 4.2)** and logarithmic time stepping procedure described in the previous case are considered while using

the areal Coat's grid with the logarithmic refinement near the well-block as given in **Figure 4.7**.

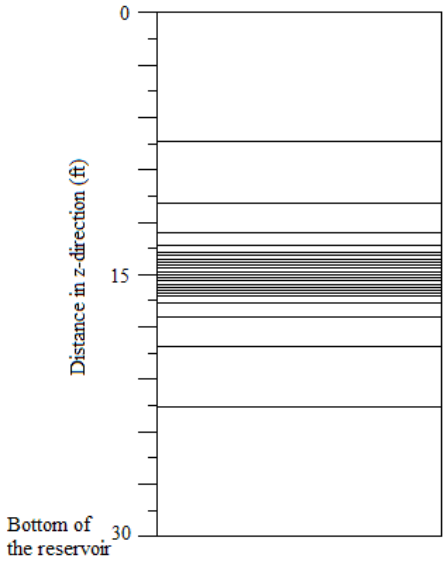

Figure 4.7 : Vertical grids of simulator, limited-entry well.

The vertical grid has a definite effect on the pressure response for limited-entry vertical wells because the numerical solution is quite sensitive to the tips of the interval. Thus, fine gridblocks near the tips of the open interval generates sufficiently accurate pressure responses. The inside of the open interval is usually considered at least 10 uniform block centered grid and then logarithmically refined from the tips to the boundary in the vertical direction. A vertical grid shown in **Figure 4.7** has a total of 100 gridblocks with 16 gridblocks with a size of 0.3125 ft for the open interval length of 5 ft and a total of 84 gridblocks logarithmically refined from the lower (and upper) tips to the bottom and top formation boundary. Therefore, the model designed in simulator uses grid system with 100 gridblocks in *r*-direction and 100 gridblocks in *z*-direction. The configuration of the example case is given by **Figure 4.8**. **Figure 4.9** and **Figure 4.10** show the comparison of the pressure change and its Bourdet's derivative solutions for drawdown and buildup periods respectively obtained from the analytical and numerical solution methods in ECRIN and from the simulator for the grid system of N=100 and M=100. The results given for our simulator are for the FIT.

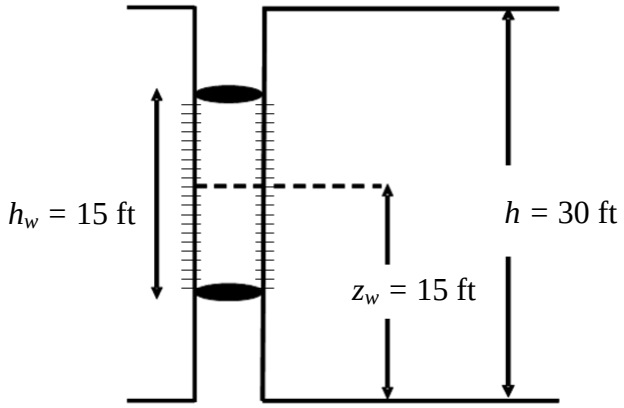

Figure 4.8 : Configuration of limited-entry.

Analytical and numerical solutions from ECRIN and the simulator yield almost identical pressure responses throughout the simulation for both periods as observed in the previous case as well. Except the time interval from 0.0001 to 0.002 hours for numerical solution from ECRIN which does not provide accurate responses like in the previous case in which reasons for the issue are stated, the agreement between the responses is very good and identical, capturing all the flow regimes; spherical flow regime (-1/2 slope line on derivative data) due to limited-entry, pseudo-radial flow (zero slope on the derivative) due to total no-flow top and bottom boundaries, and finally the pseudo-state state flow (unit-slope line) due to no-flow boundaries.

In order to investigate gridding issues, vertical voronoi grid of ECRIN is shown in **Figure 4.11** where total number of gridblocks is 2051 while the system used in our simulator contains 10000 gridblocks. Pressure change between simulator computation and analytical solution of ECRIN is slightly different (about 11 psi maximum, at the end of production period) whereas pressure change between numerical and analytical solution of ECRIN is also slightly different (about 3.2 psi maximum, at the end of production period) for the time points considered for the entire production period. Both of the numerical solutions for buildup period compare quite well with the analytical solution (maximum difference is 0.04 psi).

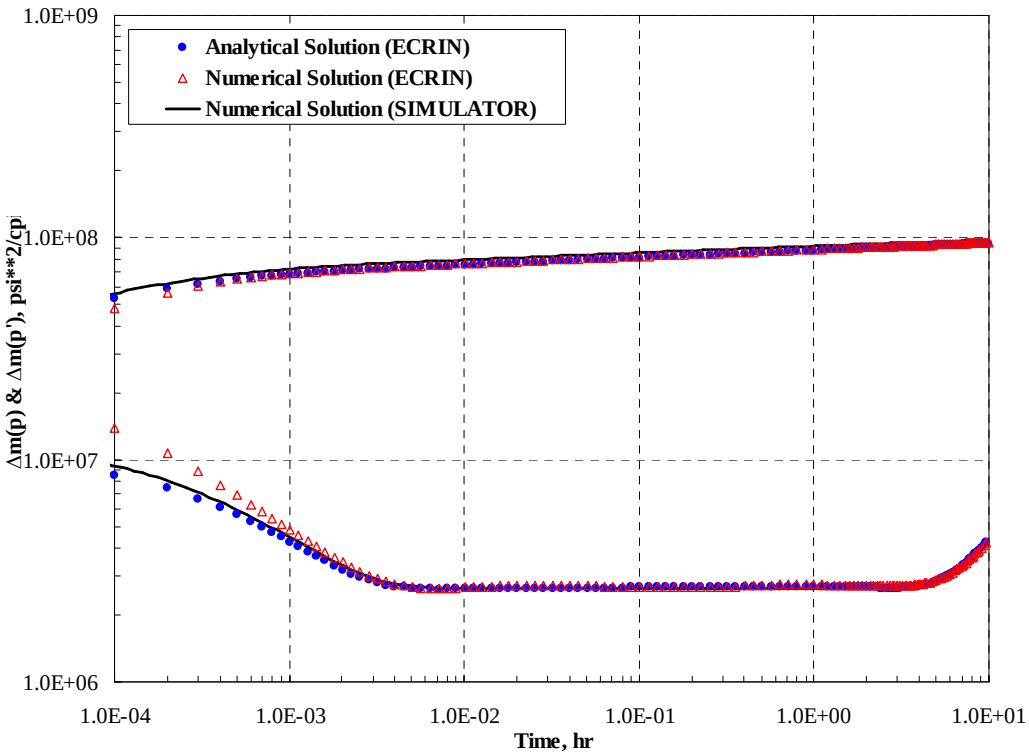

Figure 4.9 : Comparison of results, DD, limited-entry.

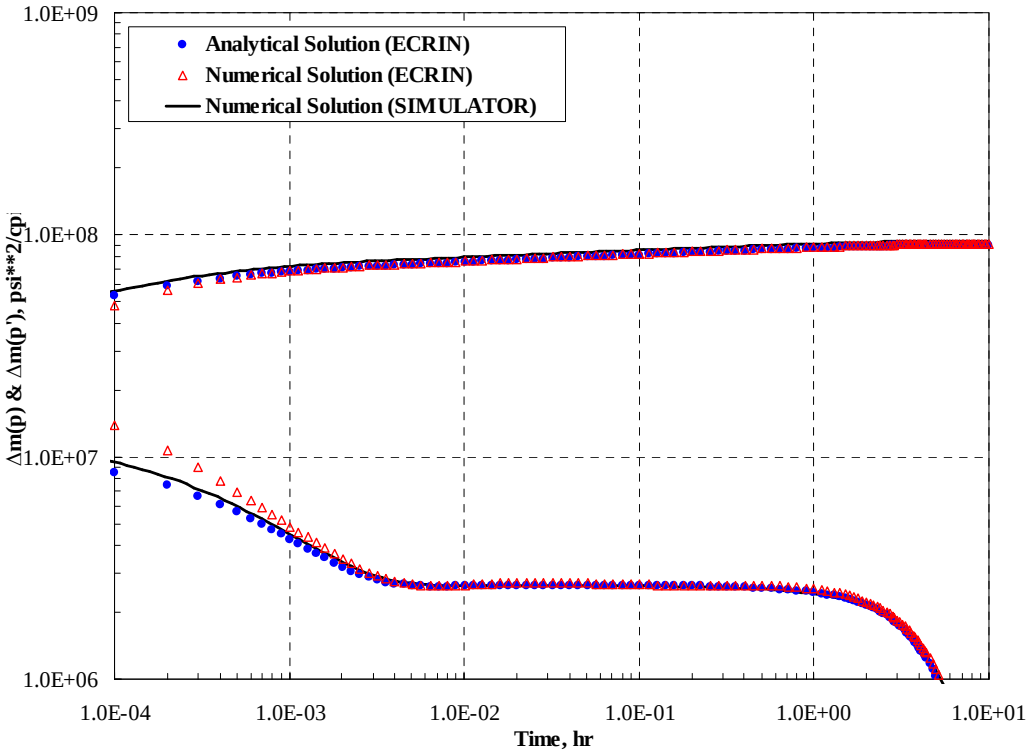

Figure 4.10 : Comparison of results, BU, limited-entry.

.

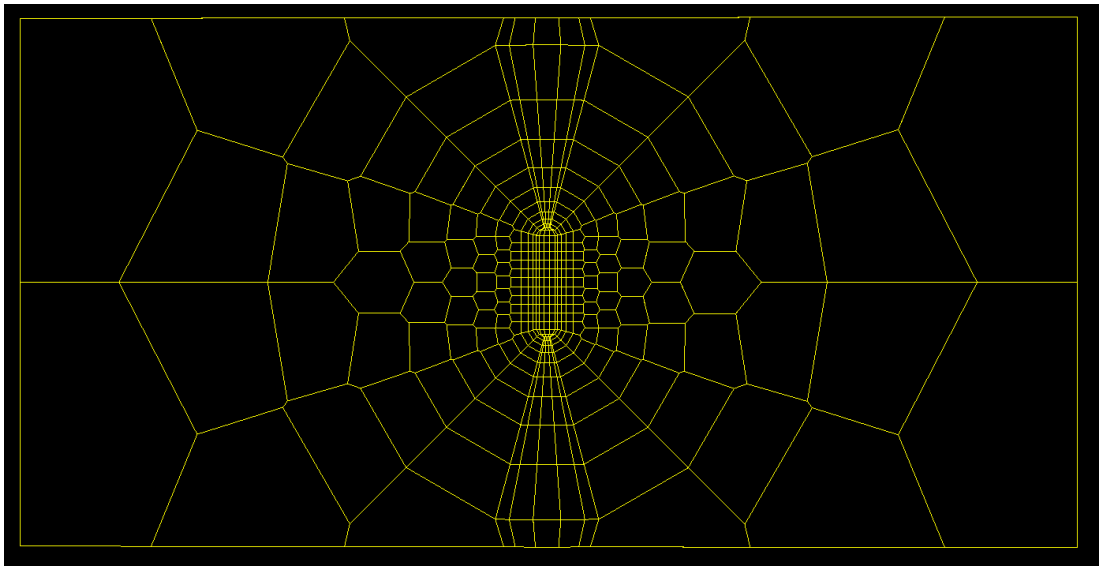

Figure 4.11 : Vertical Voronoi grids of ECRIN used for limited-entry well.

Next, like in the Case 1 of fully penetrating well case, we provide a comparison of the pressure versus time solutions generated from the FIT, NW with analytical derivatives, and NW with numerical derivatives for this limited-entry vertical case. The grid system is N=100 and M=100. This comparison is shown in **Figure 4.12**. As can be seen, all pressure solutions for the entire DD and BU periods are identical, indicating that the FIT provides the same pressures as the NW method with analytical and numerical derivatives. The CPU times for FIT, NW with analytical approach, and the NW with the numerical approach are 254 seconds, 285 seconds, and 290 seconds. Like the fully penetrating well case, the FIT method is the slightly fastest computationally. From now on, unless otherwise stated, we will use our simulator based on the FIT method to generate the pressure data.

To continue with the investigation of gridding issues and to further improve the solution, the same reservoir system is solved for different number of gridblocks in each direction. Firstly, the importance of logarithmic refinement near the well-block is shown in Table 4.3 by running the model with increased number of gridblocks in z-direction from 100 to 1000 and 2000 while keeping the same number of gridblocks in r-direction as 100. Note that logarithmically sampled time step points for each log cycle for the models considered (with 100x100, 100x1000 and 100x2000 gridblocks in r and z directions respectively) is decreased from 20 (default for all cases) to 5 in order to obtain solution faster as well as checking the consistency and number of iterations at each time step. While a simulation with 20 points per each log cycle have 243 time steps in total, newly considered simulation models with 5 points per

each log cycle have only 63. Certainly, this does not affect pressure responses and does not have any changes in the derivative plot. Thus, iteration numbers for each time step point in the case which uses higher number of time step points are less because of the corresponding time interval's being smaller. Total CPU time needed for the case in which total time step points increased from 63 to 243 is also increasing from 0.5 minutes (min) to 1.7 min.

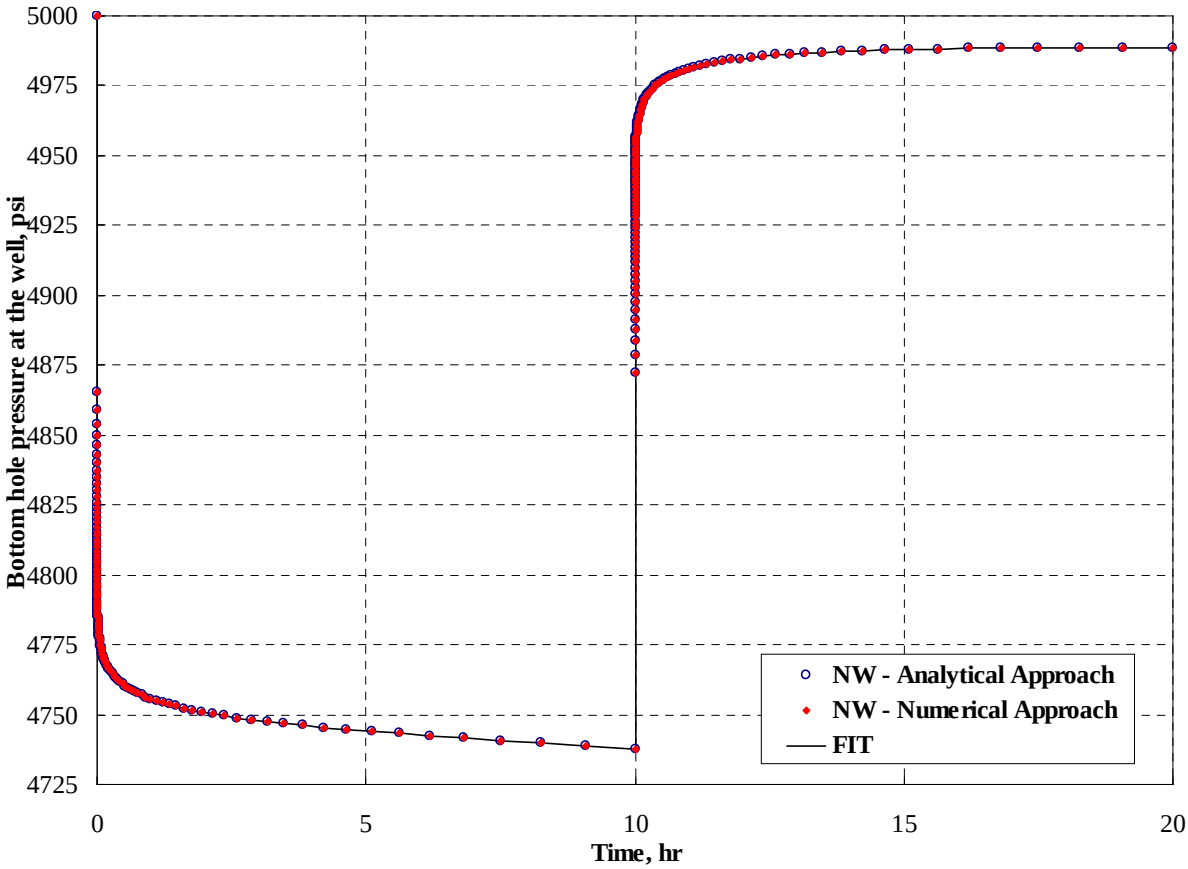

Figure 4.12 : Comparison of pressures for entire flow rate history, limited-entry.

The effect of first time step selection is also investigated by decreasing its value, which forces simulator to use more time step points and consume extra CPU times, however, give identical pressure responses as well as the pressure derivatives. Note that all models throughout the entire project are solved with the same first time step point which is the minimum value allowable to choose for calculations in ECRIN given in Table 1.1.

Table 4.3 : Effect of increase in the number of gridblocks in *z*-direction.

Number of Gridblocks used in *r*-direction and *z*-direction respectively	At end of production	At end of buildup	CPU time (min)
100x100	4737.726	4988.597	0.5
100x1000	4739.094	4988.473	7.2
100x2000	4739.453	4988.472	16
Numerical Solution (ECRIN)	4745.527	4988.637	< 0.1
Analytical Solution (ECRIN)	4748.677	4988.635	< 0.01

Next, the effect of change in number of gridblocks in *r*-direction is investigated and the results are tabulated in Table 4.4. It can be well observed that it does not have any effects as long as the sufficient amount of gridblocks in *r*-direction used. If this does not prevail (usually at very less amount of gridblocks practices like below 25), then both pressure and particularly pressure derivative responses are affected significantly and resulting in misrepresentation of the flow regimes by giving unreasonable responses.

Table 4.4 : Effect of increase in number of gridblocks in the *r*-direction.

Number of Gridblocks used in *r*-direction and *z*-direction respectively	At end of production	At end of buildup
100x100	4737.726	4988.597
1000x100	4737.937	4988.475
100x1000	4739.182	4988.473
200x1000	4739.253	4988.473
Numerical Solution (ECRIN)	4745.527	4988.637
Analytical Solution (ECRIN)	4748.677	4988.635

Pressure solutions at each iteration of any time step points during the simulation are also investigated from different solvers which are introduced in Chapter 3 to solve matrix problems resulting from both FIT and NW methods. SDRV for FIT method and NDRV for NW method are decided to use for the entire project taking into consideration of the minimum CPU time (Table 4.5) and the identical agreement of all solutions between each other. Note that number of logarithmic time step points for each log cycle is selected as 3, while first time step point is default from Table 4.1, and as a final point, the grid system used is 100x1000. Pressure solutions (up to 10 digits) and total iteration numbers from each solver for the entire time period of simulation are exactly same. In fact, total iteration number dominated by the magnitude of the non-linearity of the problem as well as each time step duration

selected to simulate for the entire flow rate history. Therefore, it may certainly depend on logarithmic sampling of time step points per each log cycle in the simulator. When it is selected as 3, 5, 10 and 20; total iteration numbers considering all solvers for this case, respectively, are 76, 123, 240, and 465. Note that LINCGB is not considered since matrix obtained from the case considered is higher than its limits.

Table 4.5 : Comparison of all sparse matrix solvers with respect to CPU time.

Solvers (Numerical Model)	CPU Time (min)
SDRV (FIT)	4.9
SSIP (FIT)	7.5
NDRV (NW-Analytical)	6.4
TDRV (NW-Analytical)	7.2
CDRV (NW-Analytical)	6.6

Several properties to model the reservoir system have been discussed and further implemented for the other following cases as well as the applications such as:

- For limited-entry well cases, it is critical to use logarithmic refinement in gridblocks with the maximum available number of gridblocks. However, for the case considered, solutions from simulator do not increase more than 1.5 psi. Therefore, throughout the study, no more than 100 gridblocks are encouraged to use in *z*-direction since it can already provide reasonably close pressure and pressure derivative results to the analytical solution of ECRIN.
- Increase in time step points or decrease in first time step selection (for all cases) and increase in the number of gridblocks in *r*-direction (for limited-entry well cases) do not improve solution at all, provided that the minimum required values are not manipulated. Though, taking more CPU time.
- CPU time dominated by three properties used in simulation calculations which are the number of logarithmic time step points for each log cycle, first time step point and finally the number of gridblocks in each direction.

4.3 Case 3: Limited-Entry with Non-Darcy Flow Effects

Non-Darcy flow effects for a single limited-entry well case are investigated in this case where the reservoir (Table 4.1), flow rate history (**Figure 4.3**), configuration (**Figure 4.7**), grid system, and time points described in the previous case are considered. As described previously, ECRIN evaluates non-Darcy flow effects as constant in the simulation model unlike the finite difference equations derived in Chapter 3. In order to verify simulator results with ECRIN, either non-Darcy coefficient, *D*, should be calculated from Eq. 2.93 before the simulation, and provided as an input to the simulator or pressure results may be obtained from the simulator by running the finite difference method including non-Darcy flow effects and then interpreted in ECRIN's non-linear regression module so that a non-Darcy flow coefficient, *D*, represented by the obtained data from simulator can be approximated in order to further be taken as an input value for the simulator to re-run the same model in ECRIN's way (described in Chapter 3 and provided as an option in the simulator) and finally compare these results with an additional run in ECRIN performed with the non-Darcy flow coefficient. Second option allows demonstrating simulator's capability by running both with non-Darcy flow coefficient, *D* as well as with evaluating non-Darcy flow effects in the finite difference equations. In the result of running the model described here in finite difference method of the simulator, pressure responses and flow rate history are put as input data in order to perform data interpretation in ECRIN and eventually used to approximate a non-Darcy flow coefficient as, $D=2.31\times10^{-5}$ *MSCF/D*$^{-1}$. Subsequently, simulator is run again for the same model with ECRIN's way (provided as an option in the simulator) which requires a non-Darcy flow coefficient as a constant value that is already achieved from the result of data interpretation in ECRIN.

Figure 4.13 and **Figure 4.14** show the comparison of the pressure change and its Bourdet's derivative solutions for drawdown and buildup periods respectively obtained from the analytical and numerical solution methods in ECRIN and from the simulator for the grid system of $N=100$ and $M=100$ when non-Darcy coefficient provided as, $D=2.31\times10^{-5}$ *MSCF/D*$^{-1}$. Since the case considered here and the previous one is identical except non-Darcy flow effects, pressure responses from both of the cases are plotted in **Figure 4.15** in order to show the impact of non-Darcy flow effects. FIT and Newton's methods from simulator provide almost same

pressure responses as well as pressure derivatives for each time step similar to the previous cases. Therefore, comparison is not considered for the rest of the study.

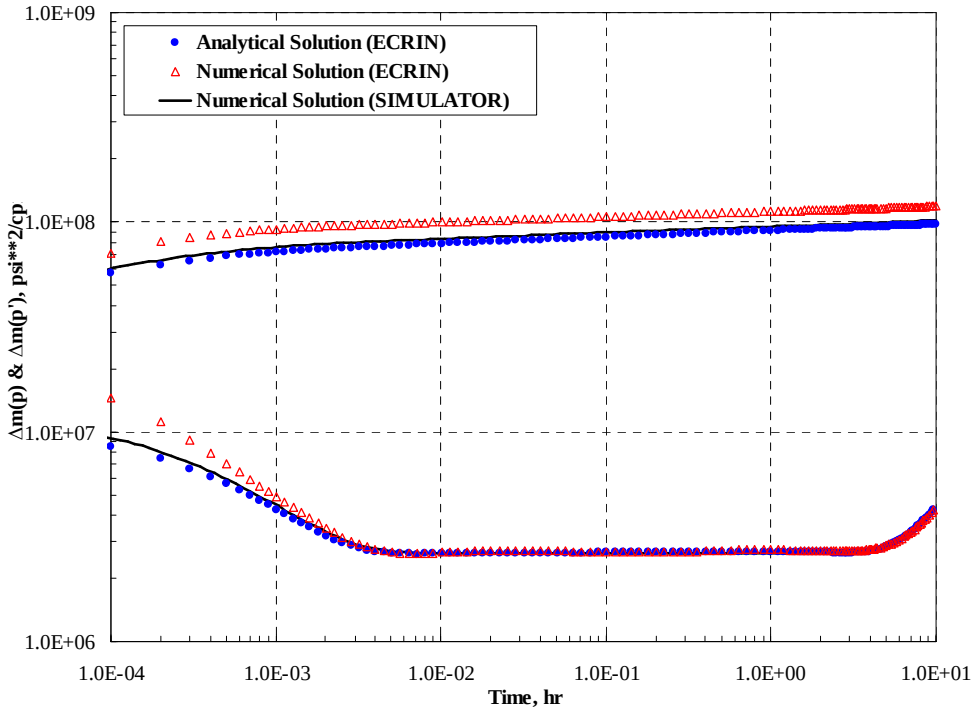

Figure 4.13 : Comparison of results, DD, limited-entry with non-Darcy flow effects.

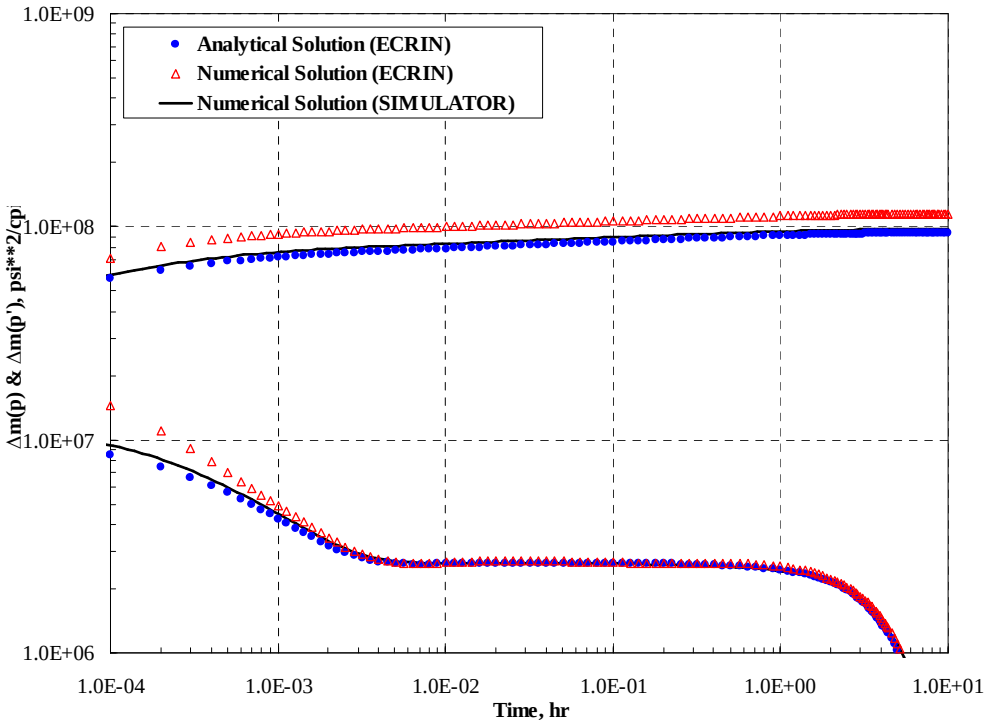

Figure 4.14 : Comparison of results, BU, limited-entry with non-Darcy flow effects.

Analytical and numerical solutions from ECRIN and the simulator yield almost identical pressure derivative responses throughout the simulation for both periods. Except the time interval from 0.0001 to 0.002 hours for numerical solution from ECRIN which does not provide accurate responses like in the previous case in which reasons for the issue are stated, the agreement between the responses is very good and identical, capturing all the flow regimes; spherical flow regime (-1/2 slope line on derivative data) due to limited-entry, pseudo-radial flow (zero slope on the derivative) due to total no-flow top and bottom boundaries, and finally the pseudo-state state flow (unit-slope line) due to no-flow boundaries. Pressure change between simulator computation and analytical solution of ECRIN is slightly different (about 11.4 psi maximum, at the end of production period) whereas pressure change between numerical and analytical solution of ECRIN is quite different (about 60 psi maximum, at the end of production period) for the time points at the production period. Both numerical solutions at buildup period compare quite well with the analytical solution (maximum difference is 0.04 psi).

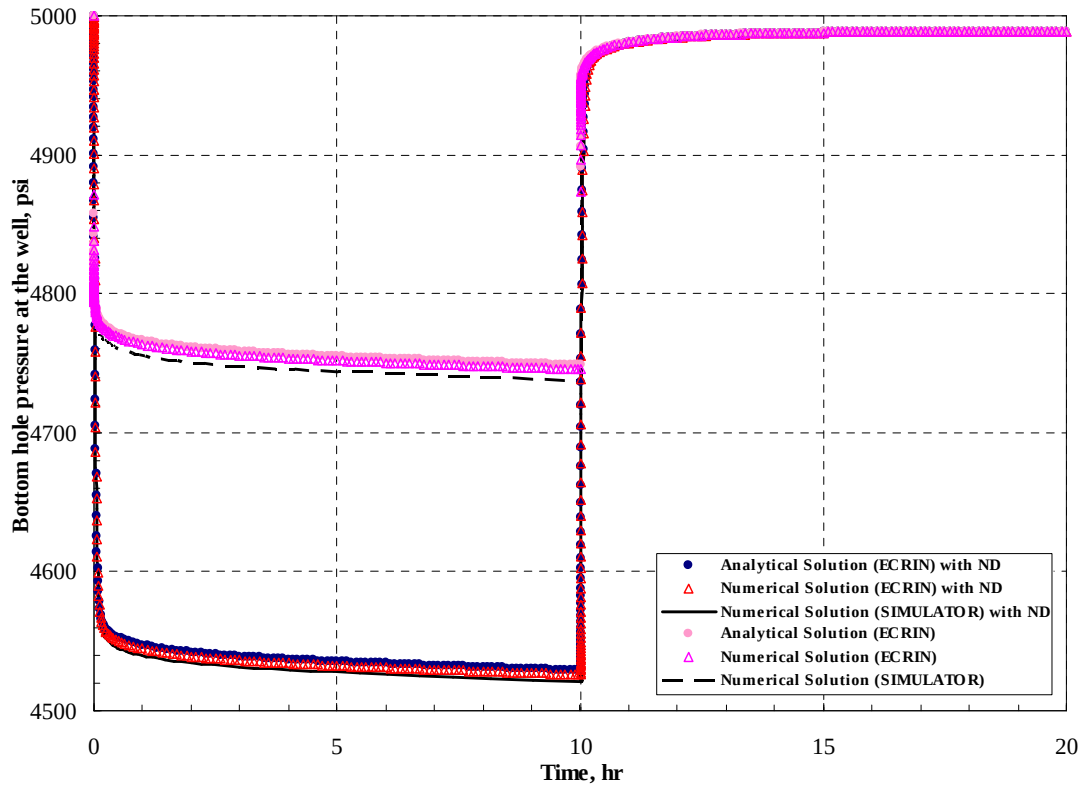

Figure 4.15 : Comparison of pressures for the entire flow rate history, case #3.

4.4 Case 4: Limited-Entry with Wellbore Storage and Skin

Wellbore storage as well as positive skin for a single limited-entry well case are investigated in this case where the reservoir (Table 4.1), flow rate history (**Figure 4.3),** grid system and time points described in the first case are considered while the location of the open interval is changed as adjacent to the top boundary as given in the configuration of the well sketch in **Figure 4.7** whereas open interval length which has logarithmic refinement near the well-block and thickness remains the same. As mentioned in Chapter 3, ECRIN defines wellbore storage effects as a constant value in the simulation model, and skin only in the gridblocks which are adjacent to the wellbore. Simulator is capable of considering both of these parameters in the way ECRIN does, however, finite difference method in the simulator can only treat skin in such way that a skin region in the *r*-direction is created around the wellbore as also discussed earlier. Results from both ways are discussed further progressively. In order to verify results with ECRIN, wellbore storage is treated as constant, C=0.01 *bbl/psi*, in the simulator and skin is performed the way ECRIN evaluates and chosen as 2.

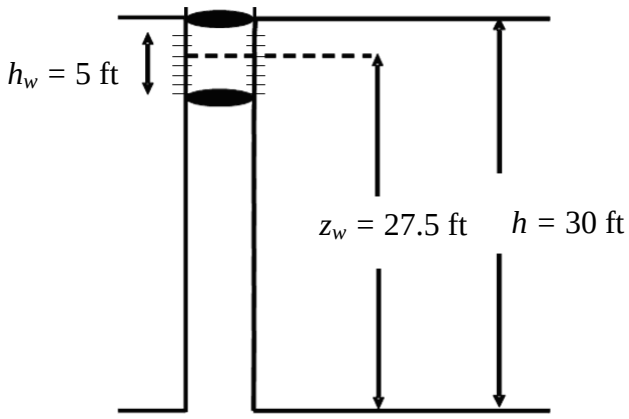

Figure 4.16 : Configuration of limited-entry with WBS and skin.

Figure 4.17 and **Figure 4.18** show the comparison of the pressure change and its Bourdet's derivative solutions for drawdown and buildup periods respectively obtained from the analytical and numerical solution methods in ECRIN and from the simulator for the grid system of N=100 and M=100.

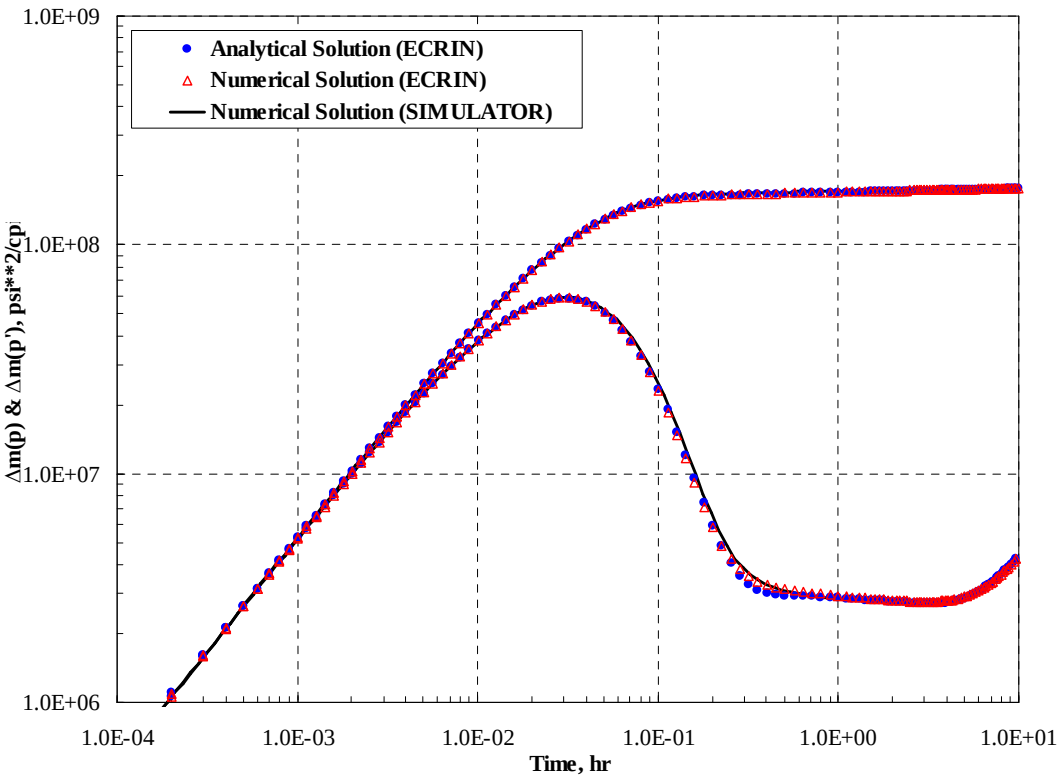

Figure 4.17 : Comparison of results, DD, limited-entry with WBS and skin.

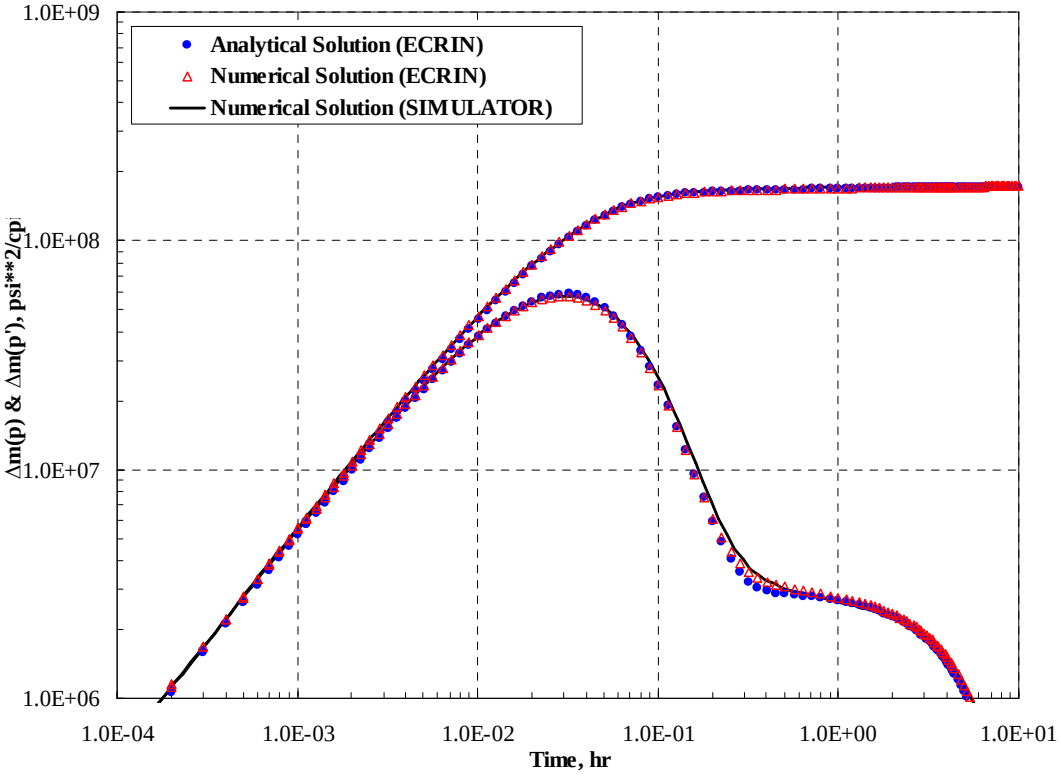

Figure 4.18 : Comparison of results, BU, limited-entry with WBS and skin.

The agreement between the responses is very good and identical, capturing all the flow regimes; wellbore storage flow regime (unit-slope line on the derivative data),

pseudo-radial flow (zero slope on the derivative) due to total no-flow top and bottom boundaries, and finally the pseudo-state state flow (unit-slope line) due to no-flow boundaries. In this case, spherical flow regime (-1/2 slope line on derivative data) due to limited-entry is obscured due to wellbore storage effects. Pressure change between simulator computation and analytical solution of ECRIN is slightly different (about 7.8 psi maximum, at the end of production period) whereas pressure change between numerical and analytical solution of ECRIN is also slightly different (about 3.1 psi maximum, at the end of production period) for the time values at the production period. Both numerical solutions at buildup period compare quite well with the analytical solution (maximum difference is 0.04 psi).

4.5 Case 5: Limited-Entry with Injection

Injection case as well as the negative skin for a single limited-entry well case are investigated here. Here, we also consider the same data as given in Table 4.1. The test sequence considered is shown in **Figure 4.19**. Note that the total duration of the simulation is 20 hr with 10 hr duration of an injection period followed by a 10 hr falloff period. Flow rate during the injection period is 10000 *MSCF/D*. The location of the open interval is quite close to the bottom boundary (2 ft between the bottom of open interval and reservoir) as given in the configuration of the well sketch in **Figure 4.20** whereas open interval length which has logarithmic refinement near the well-block is changed to 3 ft, while thickness remain the same. In order to verify results with ECRIN, wellbore storage coefficient is treated as constant, C=0.001*bbl/psi*, in the simulator and skin is performed the way ECRIN uses but negative at this case and it is chosen as -0.5. **Figures 4.21** and **Figure 4.22** show the comparison of the pressure change and its Bourdet's derivative solutions for injection and falloff periods respectively obtained from the analytical and numerical solution methods in ECRIN and from the simulator for the grid system of N=100 and M=100. The agreement between the responses is very good and identical, capturing all the flow regimes; wellbore storage flow regime (unit-slope line on the derivative data), pseudo-radial flow (zero slope on the derivative) due to total no-flow top and bottom boundaries, and finally the pseudo-state state flow (unit-slope line) due to no-flow boundaries. The spherical flow regime (-1/2 slope line on derivative data) due to limited-entry is obscured due to large wellbore storage effects. Pressure change

between simulator computation and analytical solution of ECRIN is slightly different (about 1.4 psi maximum, at the end of production period) whereas pressure change between numerical and analytical solution of ECRIN is considerably different (about 22.6 psi maximum, at the end of production period) for the time points at the entire production period. Both numerical solutions at buildup period compare quite well with the analytical solution (maximum difference is 0.1 psi).

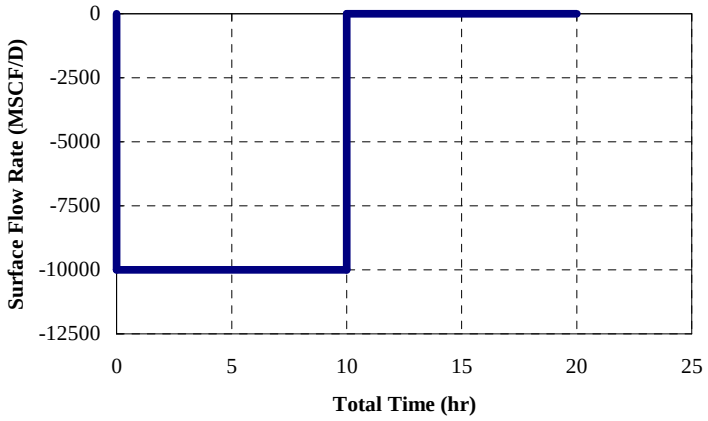

Figure 4.19 : Flow rate history at the tested well, limited-entry with injection.

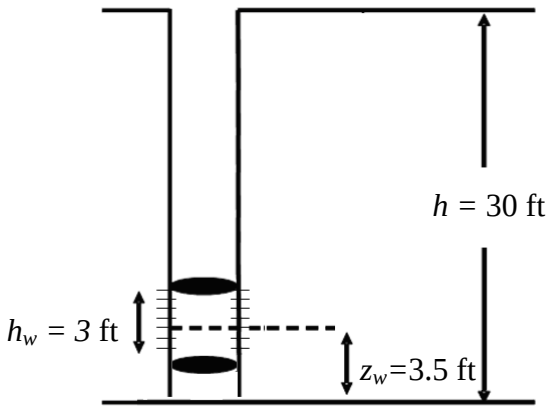

Figure 4.20 : Configuration of limited-entry with injection.

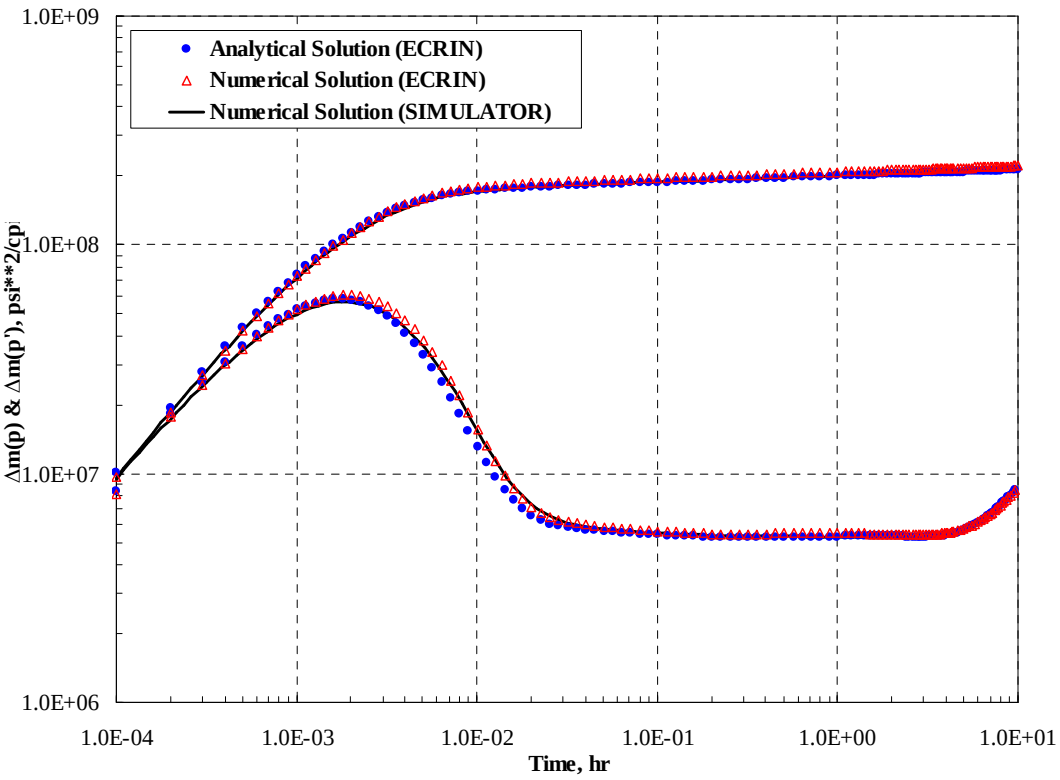

Figure 4.21 : Comparison of results, DD, limited-entry with injection.

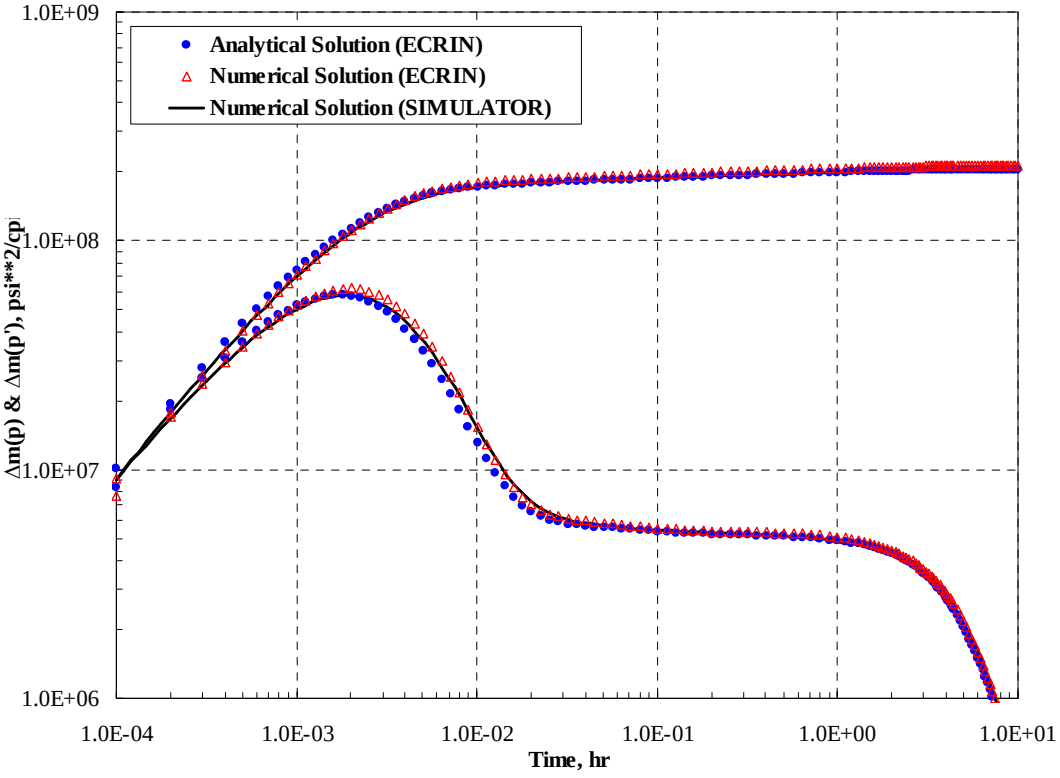

Figure 4.22 : Comparison of results, BU, limited-entry with injection.

4.6 Case 6: Limited-Entry with Multiple Production

Multiple production as well as anisotropy (the ratio between permeability in *r*-direction and *z*-direction is defined as k_z/k_r=0.1) are investigated while both of wellbore storage with pre-defined wellbore volume and non-Darcy flow effects (not constant, unlike ECRIN's treatment) by finite difference method in the simulator are introduced as well into this case where the input data to describe the reservoir is given in Table 4.6, and time step points per each log cycle described in the first case are considered while the length of the open interval which has logarithmic refinement near the well-block is 15 ft as shown in the configuration of the well sketch in **Figure 4.24** in which bottom of the open interval is 10 ft away from the bottom of the reservoir while thickness remains the same.

Table 4.6 : Input Parameters for limited-entry with multiple production.

Parameters	Values
r_w (ft)	0.33
r_e (ft)	2000
h (ft)	30
p_i (psi)	5000
T (^{o}F)	195
Gas gravity	0.7
k_r (mD)	100
k_z (mD)	10
First time step (Days)	1×10^{-4}
c_r (psi^{-1})	3.0×10^{-6}
ϕ (fraction)	0.2

The total duration of the simulation is 80 hr as can be seen from **Figure 4.23**. The duration of the each production period is 10 hr, while the duration of the buildup period is 40 hr. Flow rate during the production periods, respectively, are 2500, 5000, 7500 and 10000 MSCF/D. Skin is chosen as 5 and treated with Hawkins procedure for this case, since finite difference method only allows that. For wellbore storage calculations, wellbore volume is calculated ($V_w = \pi\, r_w^2\, h$ = 201.4 bbls) from the bottom of the wellbore to the surface equipment which is given as 4000 ft in the sketch.

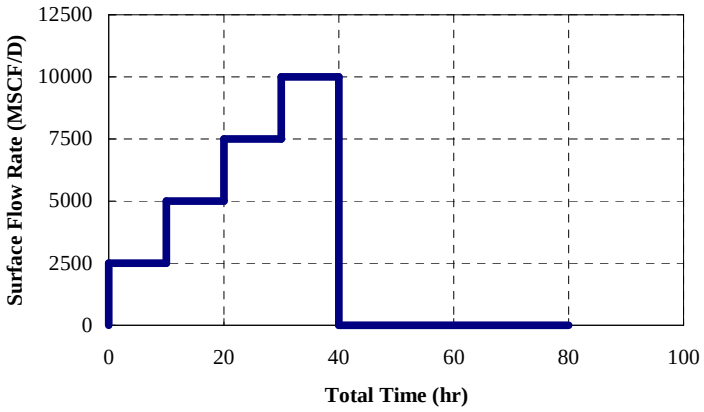

Figure 4.23 : Flow rate history at the tested well, case #6.

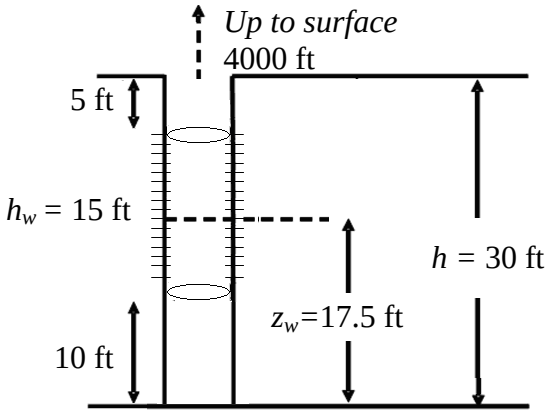

Figure 4.24 : Configuration of limited-entry with multiple production.

In order to perform verification for the case considered here with ECRIN, the model is initially run in the simulator with finite difference method, and then, further implemented its pressure responses and flow rate history to ECRIN for performing data interpretation in order to compute wellbore storage coefficient (which is considered as a constant in ECRIN) from buildup and non-Darcy flow coefficient, *D*, and mechanical skin factor by the use of Eq. 2.94. Data are analyzed for each of production pressure data pertinent to the total three production periods to determine the total skin factor and plotted as a function of the flow rate q_{sc} proceeding each production period as shown in **Figure 4.25** in which the best straight line is fitted (based on Eq. 3.12) through the three data points to determine the value of mechanical skin from the intercept and the non-Darcy coefficient. The value of skin is computed as *S*=5.07, whereas the non-Darcy coefficient *D* is computed as

D=6.61×10^{-5} (MSCF/D)$^{-1}$. Skin is found to have a relative difference of 1.4% between finite difference method (with Hawkins Method) and ECRIN treatment.

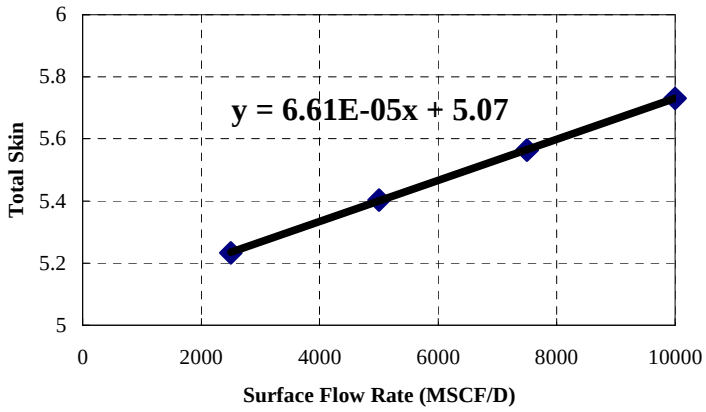

Figure 4.25 : Total skin and flow rate for limited-entry with multiple production.

From buildup analysis in ECRIN, total skin, constant wellbore storage and constant non-Darcy flow coefficient is approximated, respectively as S=5.08, C=0.0263 and D=6.83×10^{-5} (MSCF/D)$^{-1}$. Skin and non-Darcy flow coefficient are quite similar to the ones obtained form simulator. Now that wellbore storage coefficient, C from the simulator results is also obtained, verification can be performed by using S and D values (obtained from **Figure 4.25**) as well as C (obtained from buildup analysis in ECRIN) to run a new the model in ECRIN and comparing its results with the one which was run in finite difference method at the first place. **Figure 4.26** and **Figure 4.27** shows the comparison of the pressure change and its Bourdet's derivative solutions for the buildup period obtained from the analytical and numerical solution methods in ECRIN and from the simulator for the grid system of N=100 and M=100. The agreement between the responses is very good and identical, capturing all the flow regimes; wellbore storage flow regime (unit-slope line on the derivative data), pseudo-radial flow (zero slope on the derivative) due to total no-flow top and bottom boundaries, and finally the pseudo-state state flow (unit-slope line) due to no-flow boundaries. The spherical flow regime (-1/2 slope line on derivative data) due to limited-entry is obscured due to wellbore storage. Pressure change between simulator computation and analytical solution of ECRIN is slightly different (about 1.75 psi maximum, at the end of last production period) whereas pressure change between numerical and analytical solution of ECRIN is also different (about 12.1 psi maximum, at the end of production period) for the time points at the entire

production period shown in **Figure 4.25**. Both numerical solutions at buildup period compare quite well with the analytical solution (maximum difference is 0.03 psi).

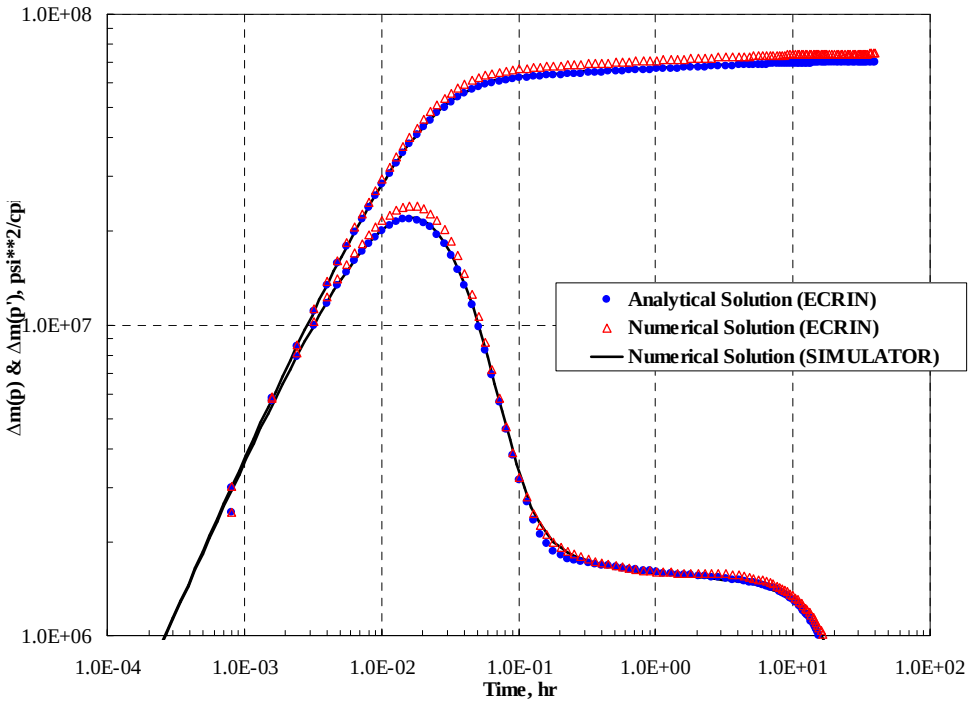

Figure 4.26 : Comparison of results, BU, limited-entry with multiple production.

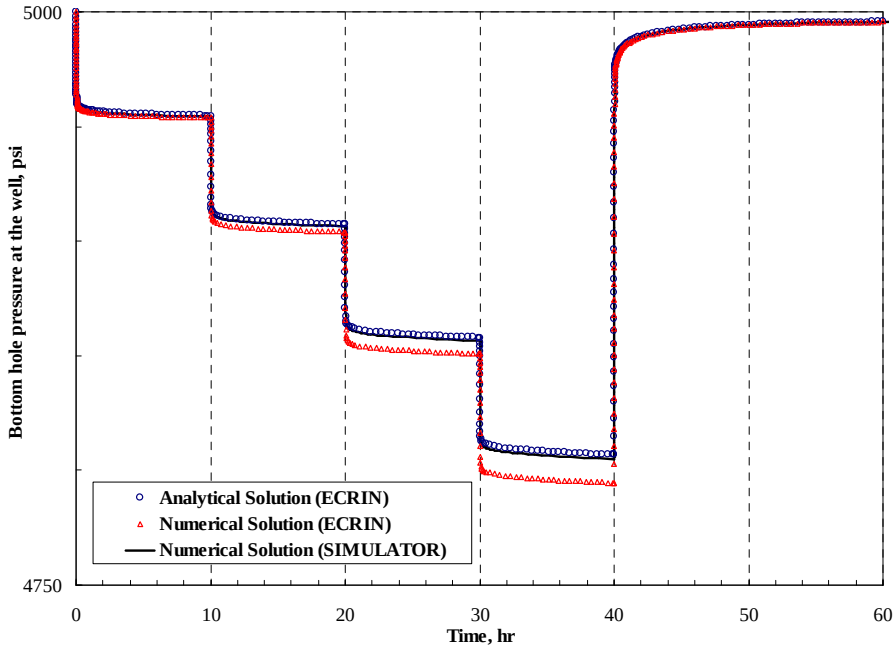

Figure 4.27 : Comparison of pressures for the entire flow rate history, case #6.

5. APPLICATIONS

There are three synthetic example applications considered in this chapter in order to show the usage of the simulator developed in this project so that solutions may be provided for real field applications in the industry.

5.1 Modified Isochronal Test with Full Penetration and Single-Layer

This application designed to perform a modified isochronal test for a fully penetrating well in a homogeneous and isotropic cylindrical reservoir with wellbore storage, skin and non-Darcy flow effects. The modified isochronal testing is used to construct the IPR curve as well as to determine the reservoir parameters such as permeability, skin, and non-Darcy flow coefficient. Input data for the cases considered given in Table 5.1.

Table 5.1 : Input parameters for modified isochronal test.

Parameters	Values
r_w (ft)	0.354
r_e (ft)	1500
h (ft)	98
p_i (psi)	1700
T (^{o}F)	122
Gas gravity	0.6
$k_r = k_z$ (mD)	100
Wellbore Volume (bbl)	210.2
S	10
c_r (psi^{-1})	3.0×10^{-6}
ϕ (fraction)	0.1

The total duration of the simulation is 40 hr as can be seen from **Figure 5.1**. Note that the test sequence contains four buildup periods; all buildup periods respectively are from 2 to 4 hr, from 6 to 8 hr, from 10 to 12 hr and from 18 to 40 hr following production periods respectively from 0 to 2 hr, from 4 to 6 hr, from 8 to 10 hr, from 12 to 14 and from 14 to 18 hr. The last production period is called as extended flow

period and used in constructing IPR curve. Wellbore volume is calculated from calculated ($V_w = \pi\, r_w^2\, h$ = 201.2 bbls) as the depth from surface to the bottom of the reservoir is assumed to be 4000 ft.

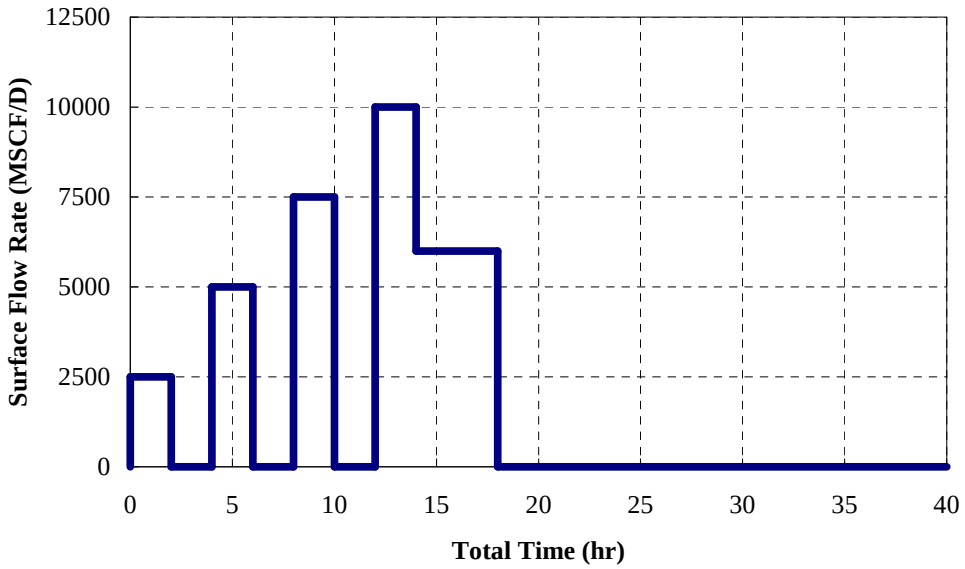

Figure 5.1 : Flow rate at the tested well for modified isochoronal test.

Pressure responses and flow rate history data is analyzed for each of production pressure data pertinent to the total four production periods to determine the total skin factor and plotted as a function of the flow rate q_{sc} proceeding each production period as shown in **Figure 3.5.** The best straight line is fitted (based on Eq. 2.94) through the four data points to determine the value of mechanical skin from the intercept and the non-Darcy coefficient. The value of skin is computed as S=9.83, whereas the non-Darcy coefficient D is computed as D=1.12×10^{-5} (MSCF/D)$^{-1}$. Skin is found to have a relative difference of 1.7% between finite difference (Hawkins Method) and ECRIN treatment. From the last and the longest buildup analysis in ECRIN, constant wellbore storage is approximated as C=0.138*bbl/psi*.

All flow regimes are captured; wellbore storage flow regime (unit-slope line on the derivative data), pseudo-radial flow (zero slope on the derivative) due to total no-flow top and bottom boundaries, and finally the pseudo-state state flow (unit-slope line) due to no-flow boundaries as can be seen in **Figure 5.3** which shows the pressure change and its Bourdet's derivative solutions for the last and the longest buildup period whereas **Figure 5.4** shows pressure responses for the entire flow history of the grid system of N=100 and M=1.

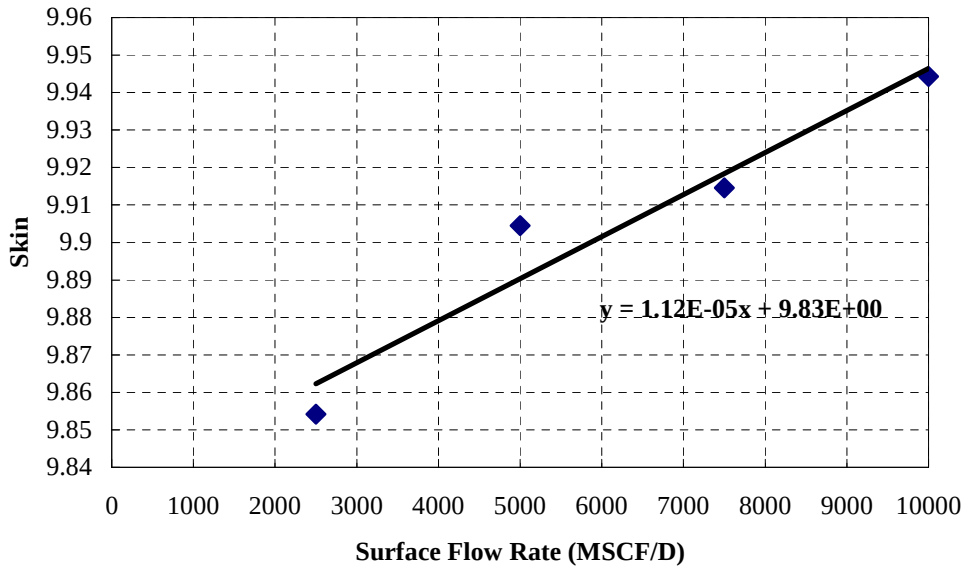

Figure 5.2 : Total skin and flow rate for modified isochronal test.

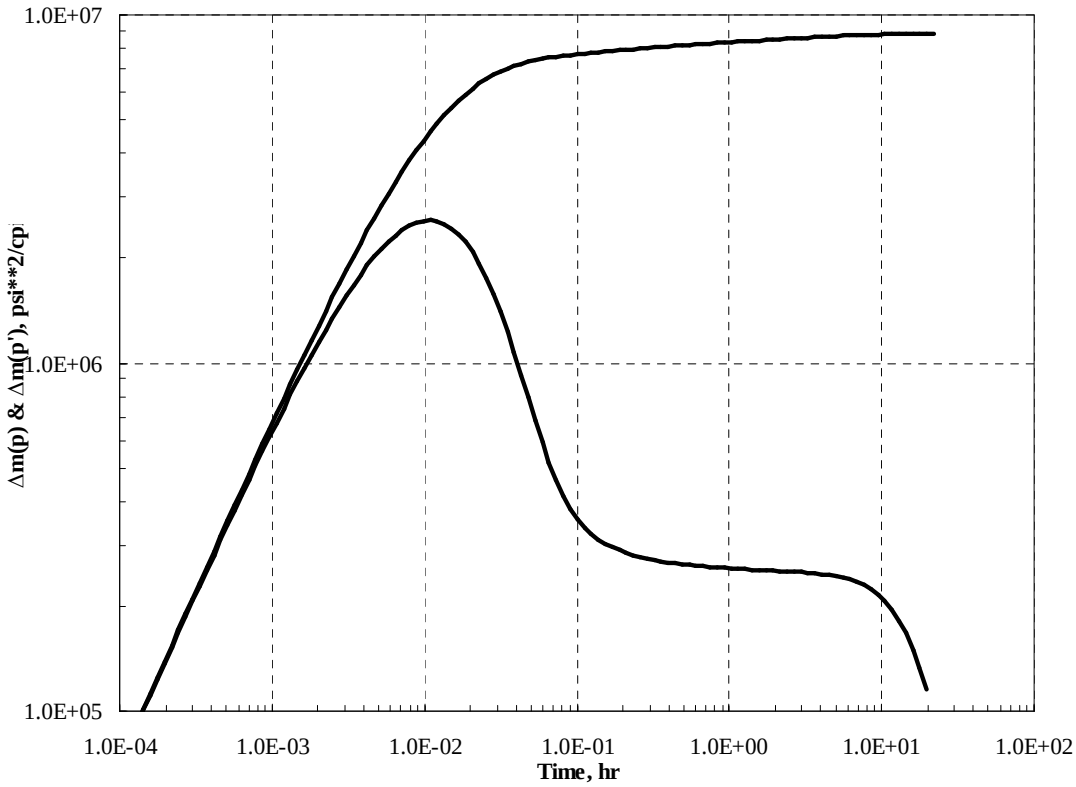

Figure 5.3 : Results, extended BU, modified isochronal test.

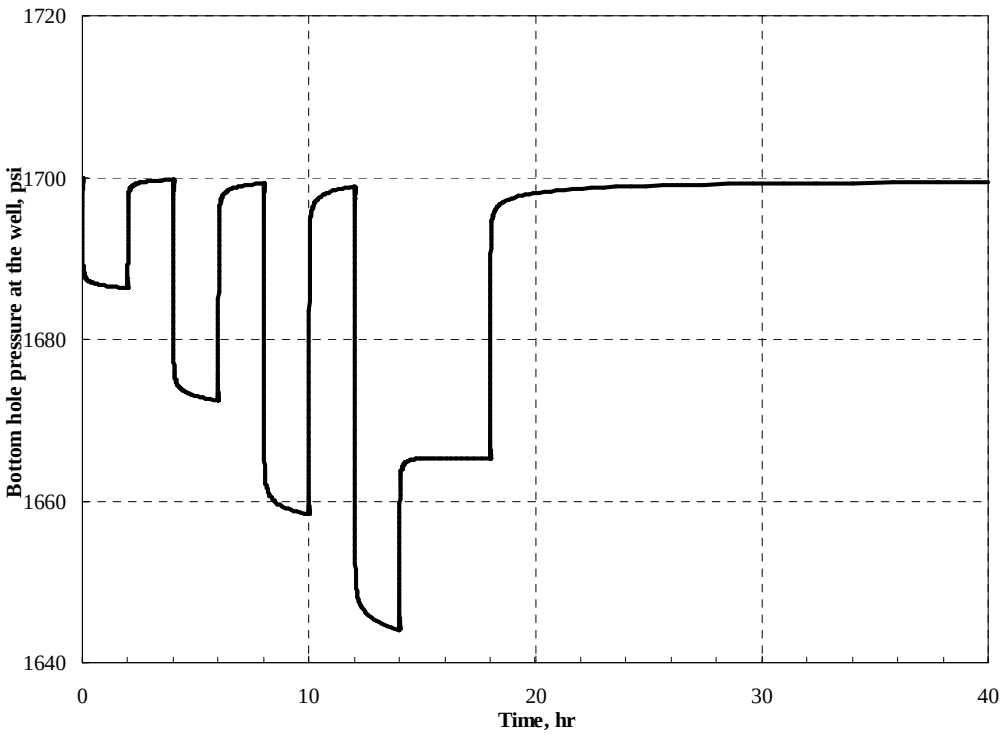

Figure 5.4 : Pressures at tested well for the entire flow rate history, application #1.

5.2 Packer-Probe Test with Single-Layer

This application designed to perform a synthetic interval pressure transient test (IPTT) sequence for a vertical gas well in a single-layer system, where pressure data acquired both at the straddle packer location and the vertical observation probe (see **Figure 5.6** for the configuration). The objectives of IPTT tests are to determine horizontal and vertical permeability and the flow barriers or high permeability streaks along the wellbore (Kuchuk et al., 2010). The basic input model parameters for this example are given in Table 5.2.

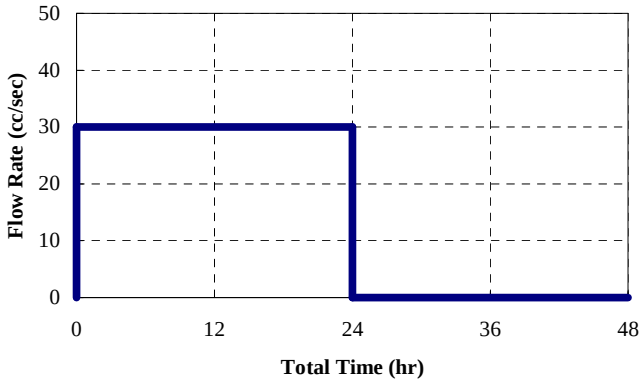

Figure 5.5 : Flow rate at tested well for packer-probe test.

Table 5.2 : Input parameters for packer-probe test.

Parameters	Values
r_w (ft)	0.354
r_e (ft)	5000
h (ft)	40
p_i (psi)	1700
T (^{o}F)	122
Gas gravity	0.6
k_r (mD)	10
k_z (mD)	1
C (bbl/psi)	0.0001
c_r (psi^{-1})	3.0×10^{-6}
ϕ (fraction)	0.1

The test sequence is shown in **Figure 5.5** where can be seen the total duration of the test is about 48 hours and the test sequence contains one production and one buildup periods with equal time durations.

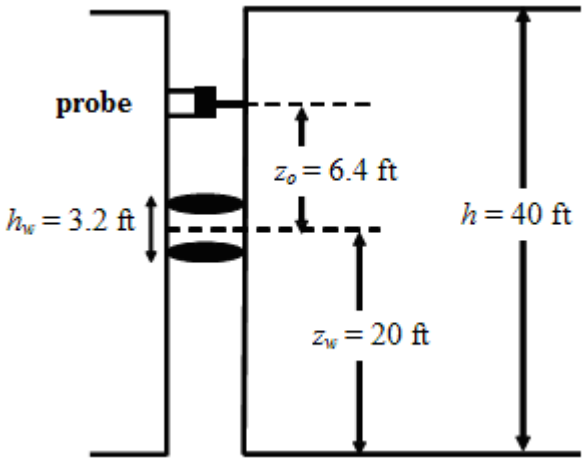

Figure 5.6 : Configuration of packer-probe test, case #1.

Firstly, gridding issues are investigated in this case where 100 gridblocks are always used in *r*-direction. Results presented in **Figure 5.7** and **Figure 5.8** without any skin and non-Darcy flow effects in three ways such as with logarithmic refinement near the open interval and the observation probe by using 175 gridblocks (as described in detail in the case 2 of previous chapter); with uniform gridblocks throughout the reservoir by using 25 gridblocks and finally with minimum amount of non-uniform gridblocks by using only 5 gridblocks only. As mentioned earlier that the vertical grid has a definite effect on the pressure response for limited-entry vertical wells.

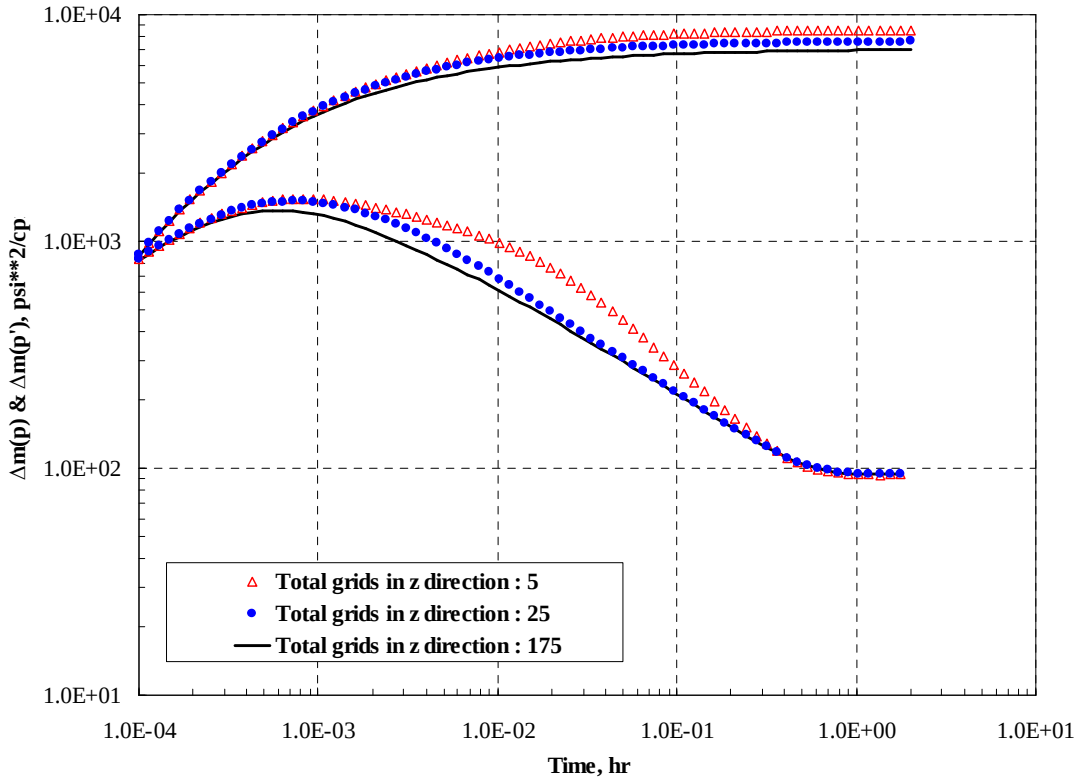

Figure 5.7 : Results, BU, at tested well, without skin and without non-Darcy,case #1.

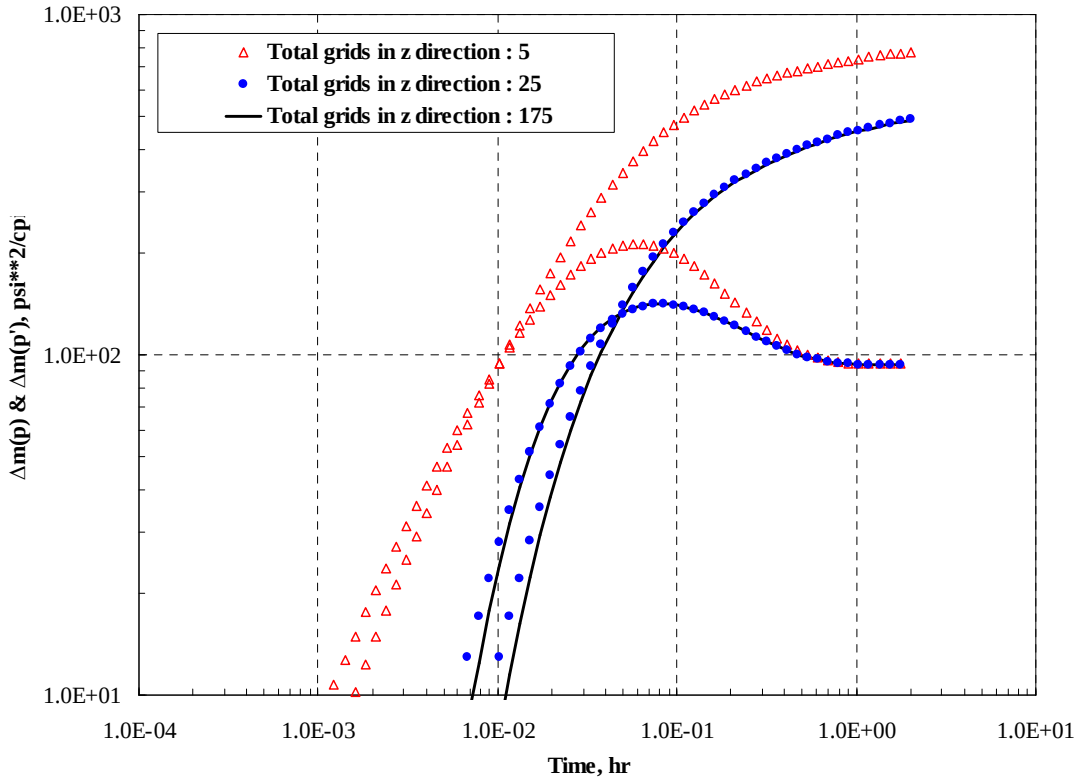

Figure 5.8 : Results, BU, at the probe, without skin and without non-Darcy, case #1.

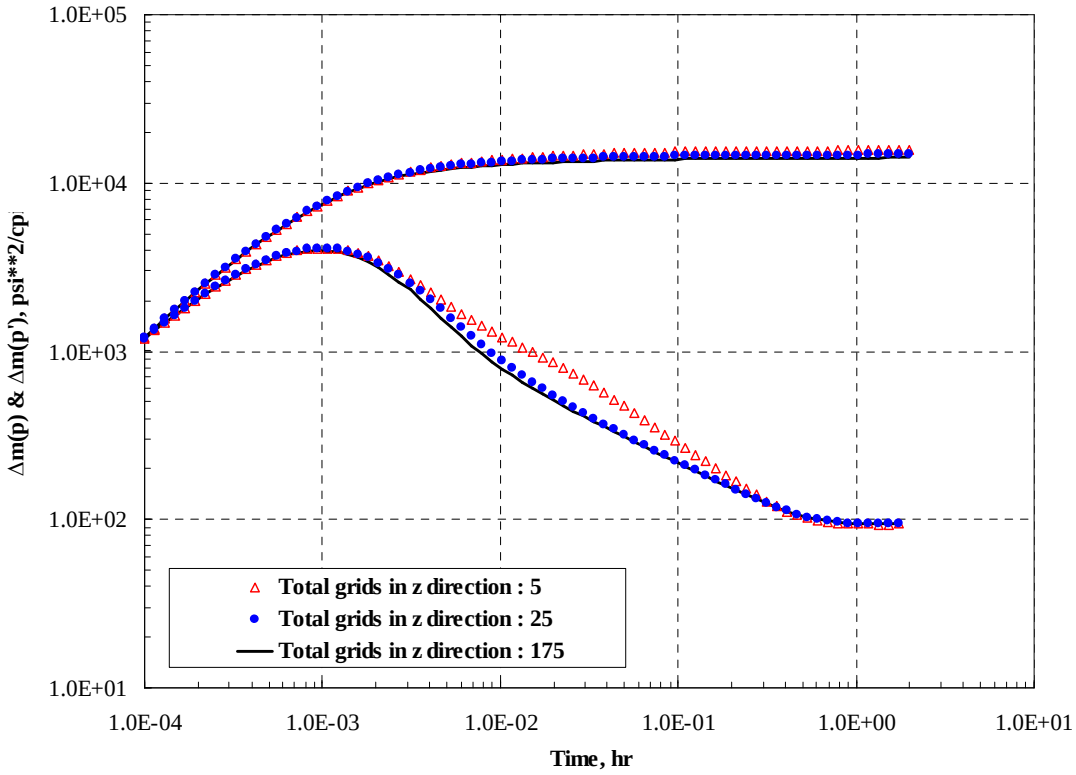

Figure 5.9 : Results, BU, at tested well, with skin=3 and non-Darcy, case #1.

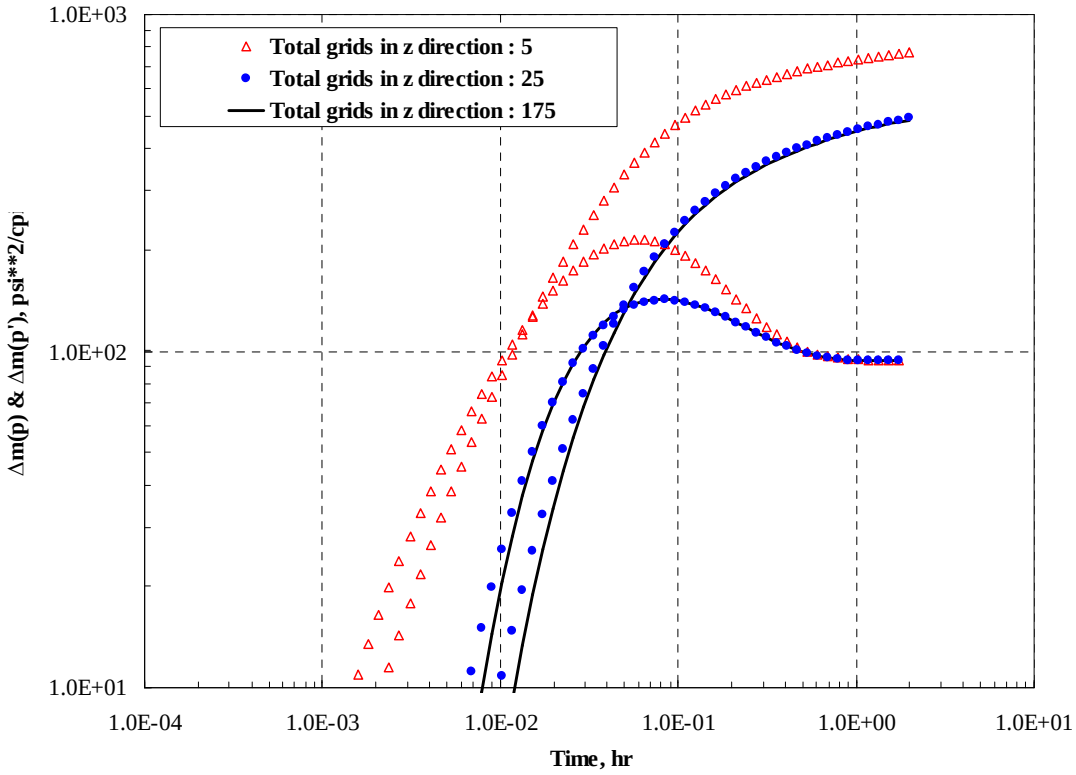

Figure 5.10 : Results, BU, at the probe, with skin=3 and non-Darcy, case #1.

However, for the case considered, solution does not improve significantly between first two approaches whereas the last approach differs considerably from others. Pressure derivative responses from each approach in **Figure 5.3** indentify first spherical flow occurring around dual-packer interval, and then the radial flow based on the no-flow top and bottom boundaries.

Secondly, skin and non-Darcy flow effects are investigated. Results presented in **Figure 5.9** and **Figure 5.10** with the first approach where 175 gridblocks are considered as previously explained. It is believed to have enough accuracy for engineering purposes for this case since gridding issues are already discussed beforehand. Pressure and pressure derivative responses are plotted in **Figure 5.11** and **Figure 5.12** where can be seen that non-Darcy flow effects do not affect the solutions for IPTT tests significantly and can be neglected.

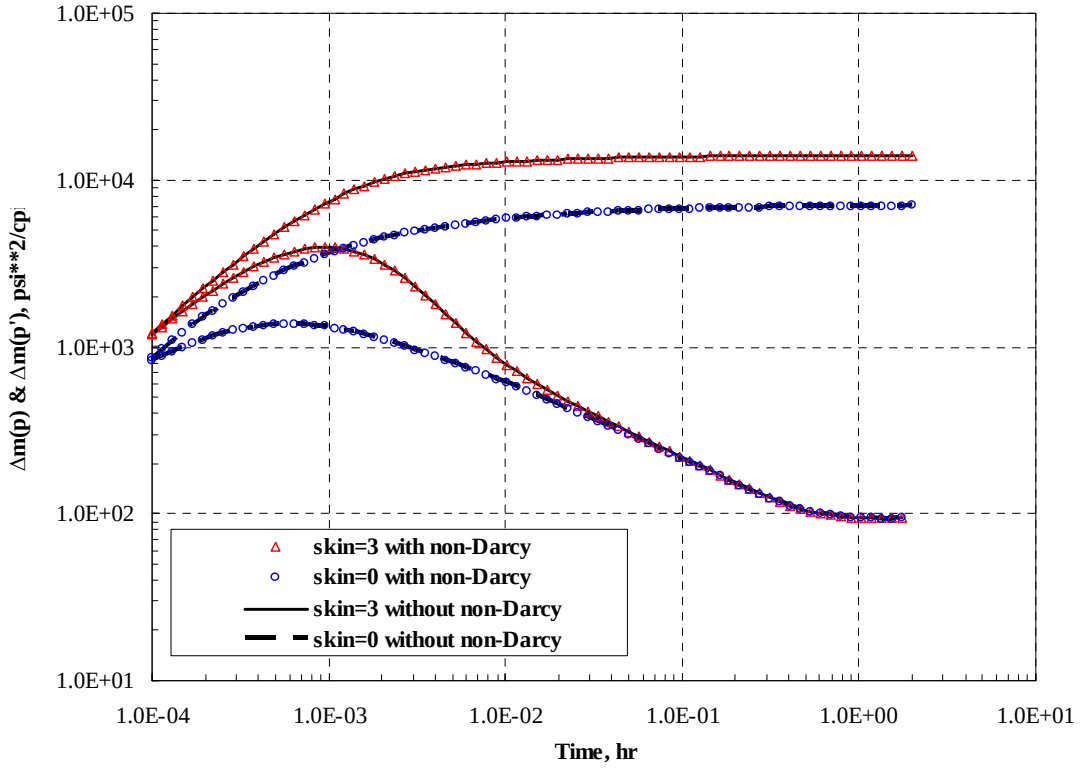

Figure 5.11 : Comparison of results, BU, at tested well, case #1.

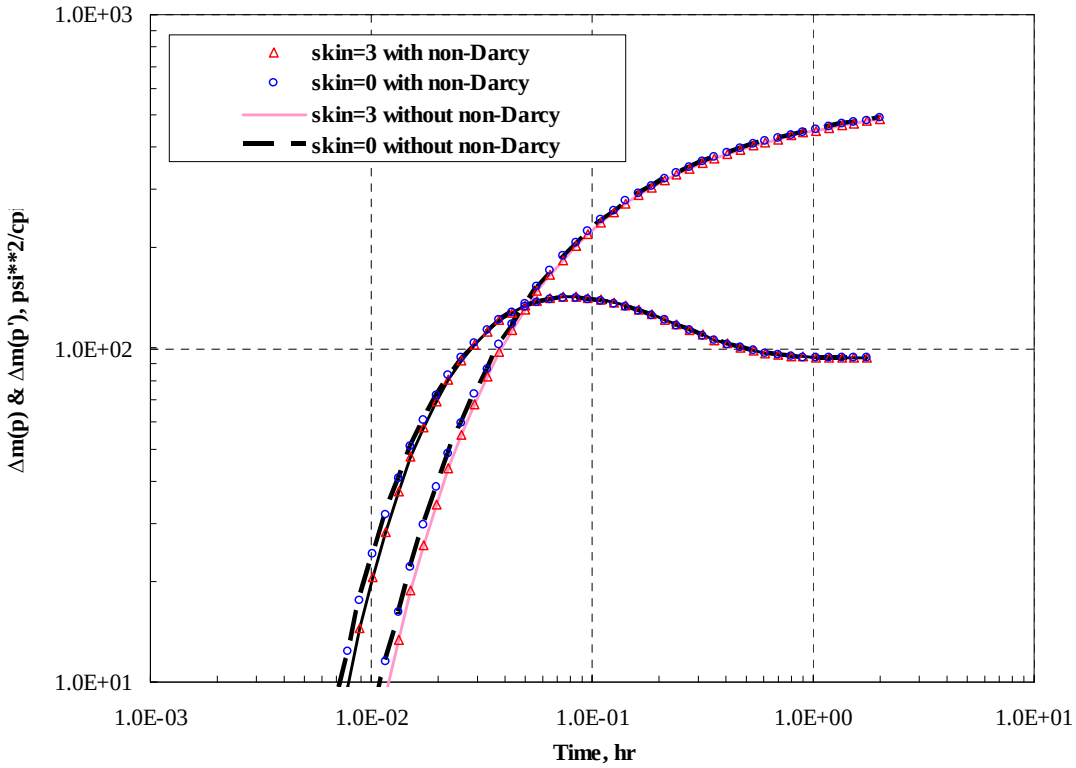

Figure 5.12 : Comparison of results, BU, at the probe, case #1.

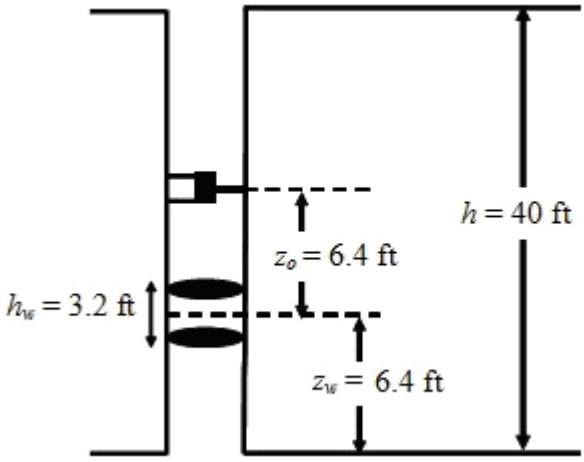

Figure 5.13 : Configuration of packer-probe test, case #2.

Furthermore, in order to introduce hemi-spherical flow regime as well as confirm the conclusions made earlier for simulation of this kind of tests, another configuration is considered as shown in **Figure 5.13** where only the location of the open interval is changed with moving downwards by 6.4 ft. Results presented in **Figure 5.14** and **Figure 5.15** without any skin and any non-Darcy flow effects as well as with skin (S=3) and non-Darcy flow effects in **Figure 5.16** and **Figure 5.17** while having the same amount of gridblocks as respectively 175, 25 and 5 in z-direction. Pressure

derivative responses for each approach in **Figure 5.14** as well as **Figure 5.16** indentify first spherical flow occurring around dual-packer interval, then the hemi-spherical flow due to no-flow bottom boundary, and then the radial flow based on the no-flow top and bottom boundaries.

In addition, skin and non-Darcy flow effects are investigated. Pressure and pressure derivative responses (using 175 gridblocks in *z*-direction) are plotted in **Figure 5.18** and **Figure 5.19** where can be seen that non-Darcy flow effects still do not affect the solutions for IPTT tests significantly and can be neglected.

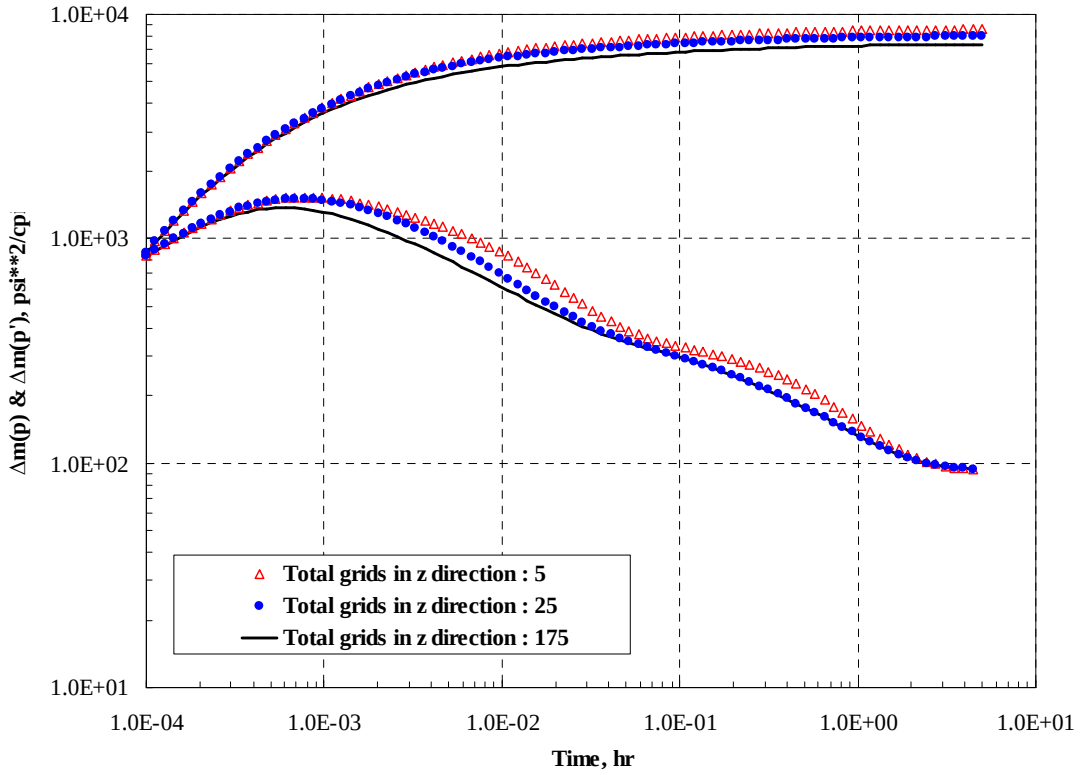

Figure 5.14 : Results, BU, at tested well without skin and without non-Darcy,case#2.

Figure 5.20 is the pressure distribution for the system in vertical axis at early times and late times for the entire flow rate history. User can see how the pressure propagates near the wellbore over both space and time. Simulator provides pressure distribution illustration with respect to time. User can select from a track bar which represents all time steps taken in the simulation for illustration to view the pressure distribution corresponding to that time point. Wide range of color scale helps to determine the regions where pressure values are represented contrasty. Blue represents highest pressure at corresponding time step whereas yellow represents lowest pressure in the color scale. Diagram of reservoir cross section (also shown in

Figure 2.1) illustrated at each screenshot in **Figure 5.20** are already discussed in Chapter 2.

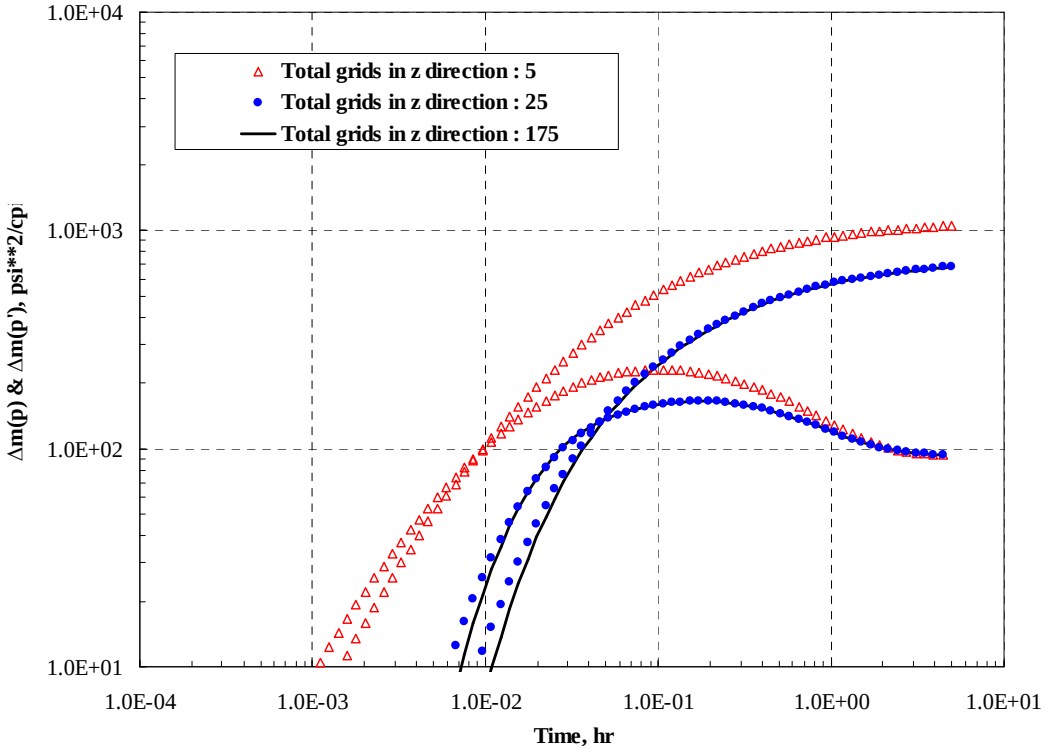

Figure 5.15 : Results, BU, at the probe, without skin and without non-Darcy, case#2.

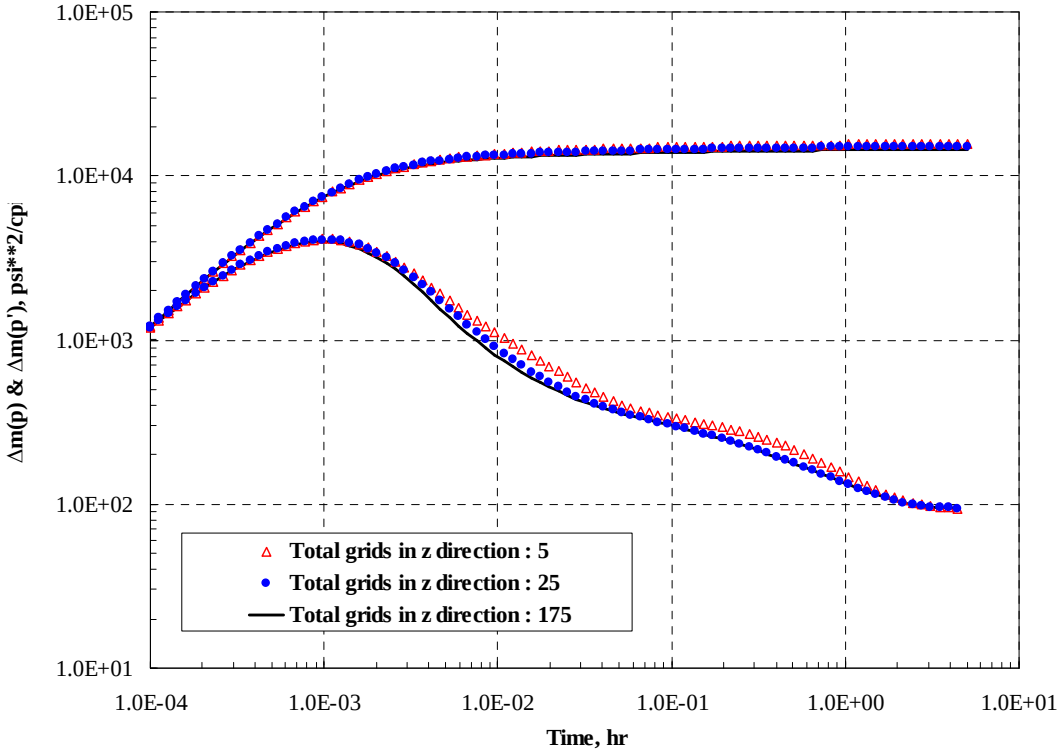

Figure 5.16 : Results, BU, at tested well, with skin=3 and non-Darcy, case #2.

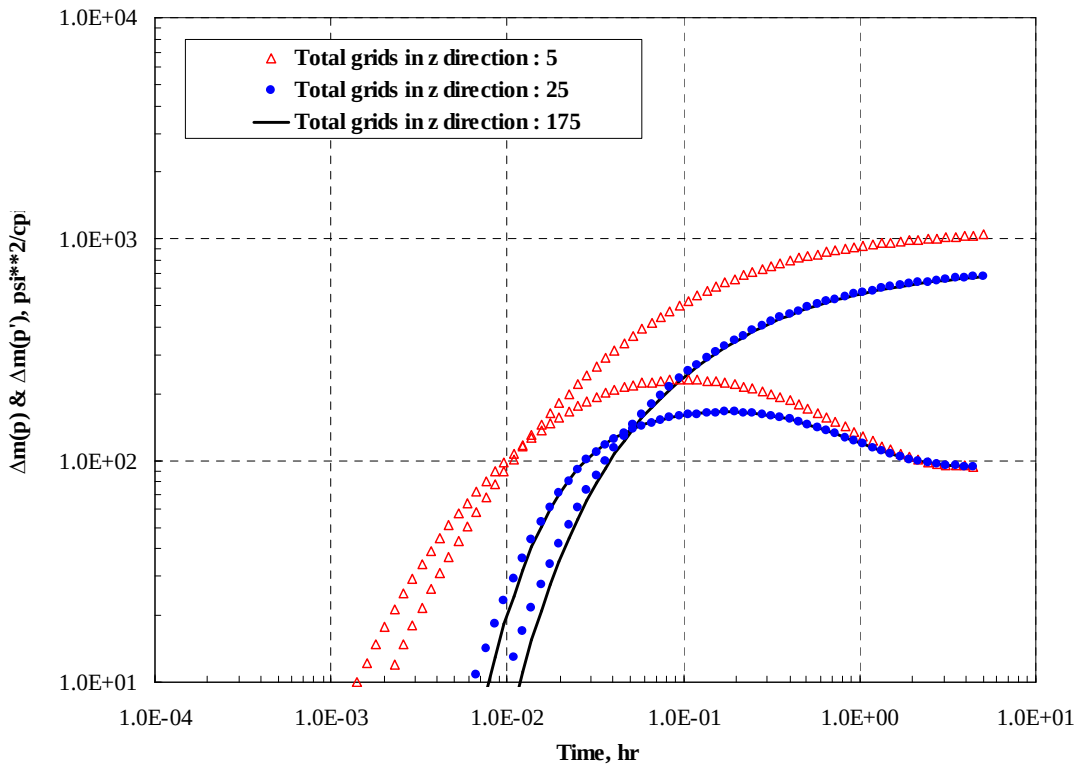

Figure 5.17 : Results, BU, at the probe, with skin=3 and non-Darcy, case #2.

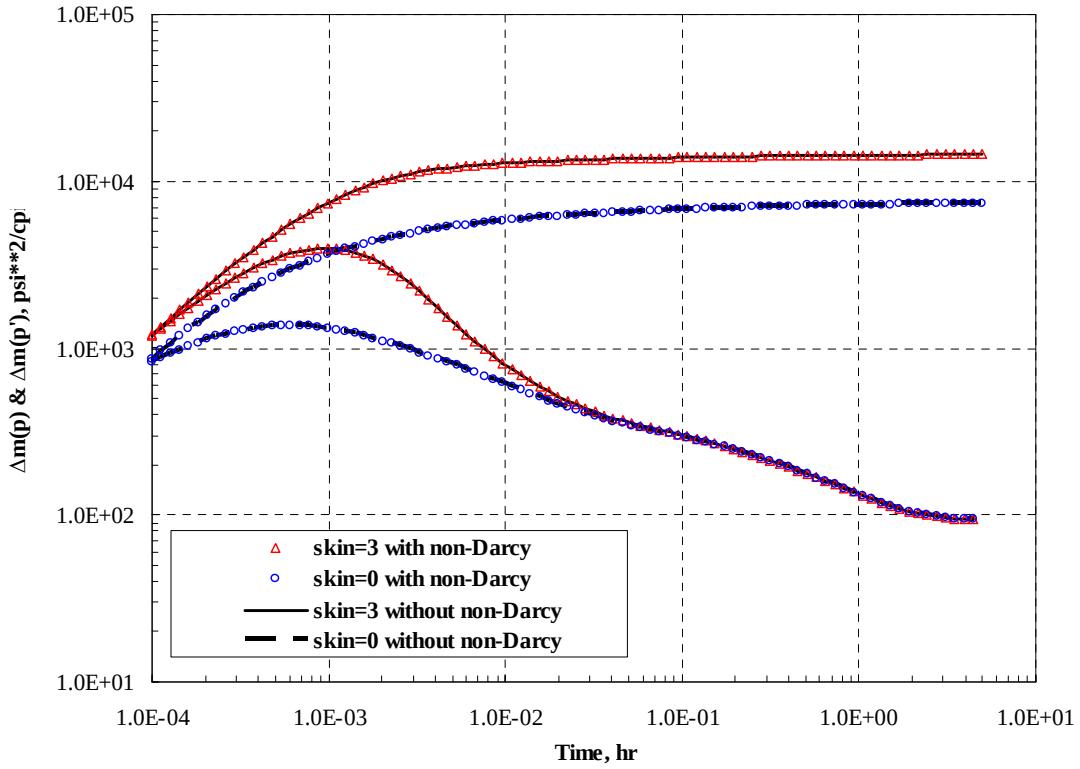

Figure 5.18 : Comparison of results, BU, at tested well, case #2.

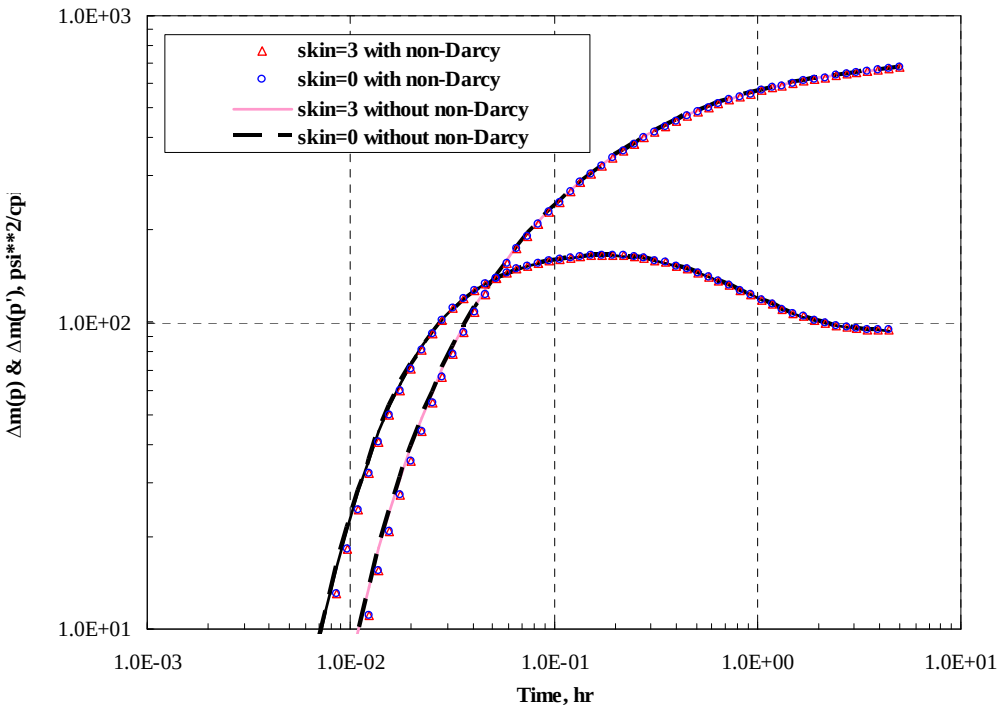

Figure 5.19 : Comparison of results, BU, at the probe, case #2.

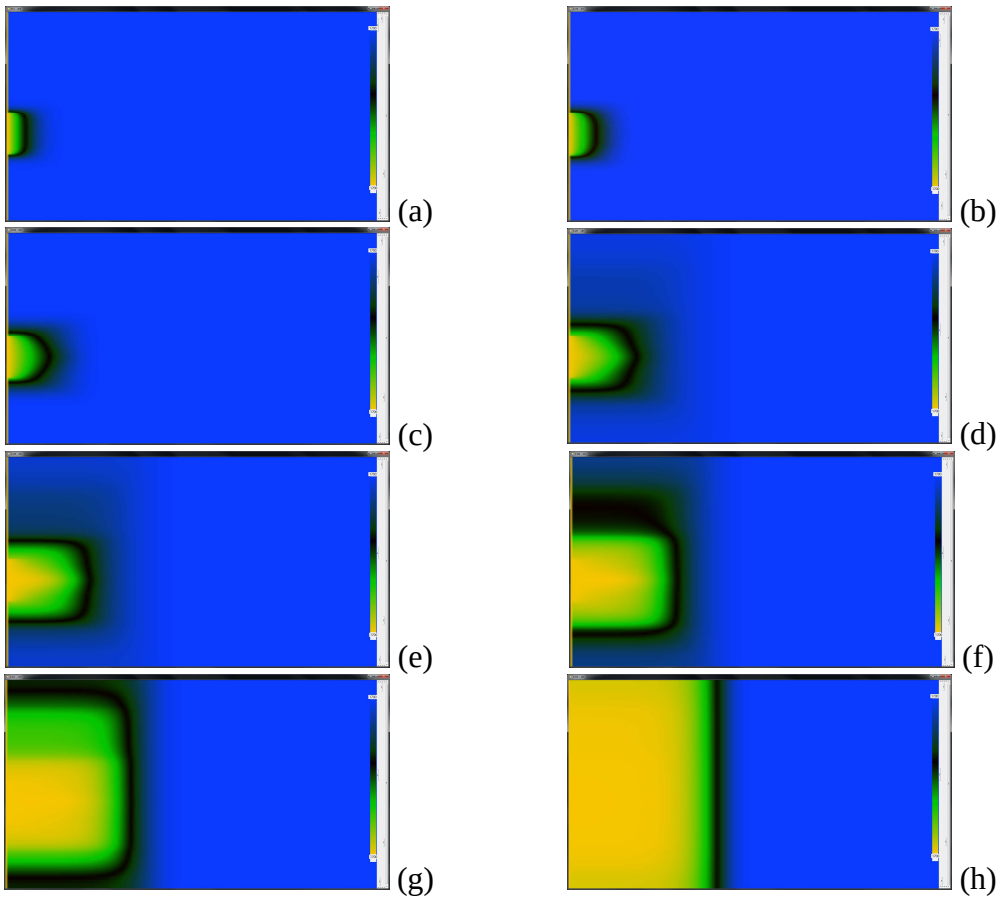

Figure 5.20 : Screenshots of pressure distributions from GUI of simulator, with skin=3 and non-Darcy flow effects, packer-probe test #1.

5.3 Multi-layers

This application designed to perform a pressure transient test sequence for a vertical gas well in a multi-layered system, in which all layers act individually while only having the same homogeneity and anisotropy (k_z/k_r=0.2). All layers have its own thickness, permeability, porosity and skin values as shown in the configuration (**Figure 5.21**) where pressure data acquired from three different production scenarios, containing either a fully penetrated well or partially penetrated well from two different places independently.

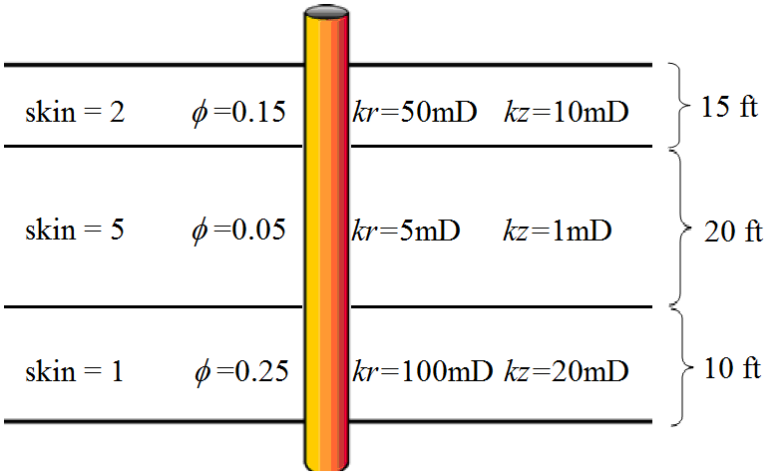

Figure 5.21 : Configuration of multi-layers test.

The basic input model parameters are given in Table 5.3 for all cases in this application. The flow rate history for the fully penetrated case when all layers are open to flow and for the partially penetrated case where only top and bottom layers are open to follow is given by **Figure 5.22** whereas the last case in which partially penetrated well producing from an open interval that is adjacent to the middle and the bottom layers is given by **Figure 5.24**. Note that for the last case described, wellbore storage is taken by the open interval's wellbore volume and calculated as $V_w = \pi\ r_w^2\ h$ = 0.9 bbls whereas for the other cases it is constant and taken as C=0.01*bbl/psi*. Non-Darcy flow effects from finite difference formulation is considered in all cases and can be either approximated from the Eq. 2.93 or by using non-linear regression software by interpreting the pressure solutions from simulator.

Table 5.3 : Input parameters for multi-layers test.

Parameters	Values
r_w (ft)	0.3
r_e (ft)	1250
h (ft)	45
p_i (psi)	5000
T (^{o}F)	212
Gas gravity	0.7
c_r (psi^{-1})	3.0×10^{-6}

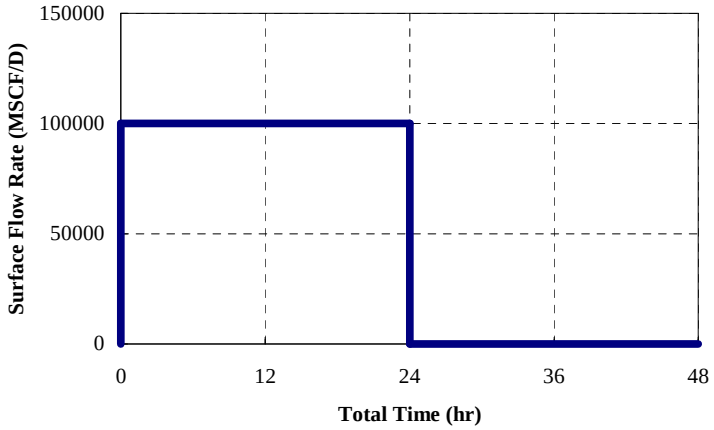

Figure 5.22 : Flow rate history at tested well for case #1 and #2 for multi-layers test.

The height of the layers from top to bottom, respectively are 15 ft, 20 ft, and 10 ft. Skin values assigned for each layer respectively with the same order are 2, 5, and 1 while porosity values are 0.15, 0.05, and 0.25. All layers have the permeability values on the *r*-direction respectively 50 mD, 5 mD, and 100 mD. This case may represent a real field application where the reservoir contains several different layers with individual properties. Such a system is not possible to be solved with an analytical approach. Therefore, it is a good application of numerical simulator presented here with GUI in order to observe pressure transients throughout the simulation.

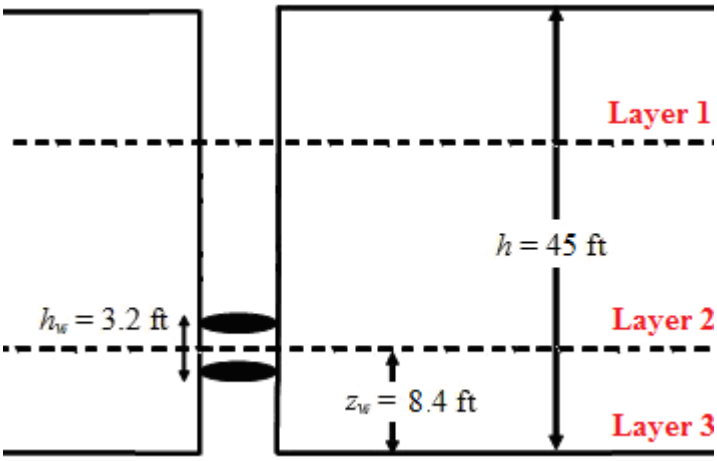

Figure 5.23 : Configuration of case #3 for multi-layers test.

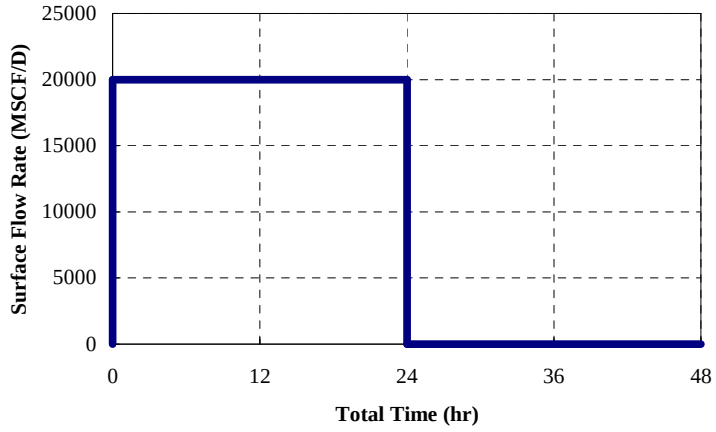

Figure 5.24 : Flow rate history at tested well for case #3 in multi-layers test.

Firstly, the gridding issues are investigated in this application and results presented in the figures in three ways such as with logarithmic refinement near the each boundary of layers, as well as the open interval by using 168 gridblocks; with uniform gridblocks throughout the reservoir by using 27 gridblocks and finally with minimum amount of non-uniform gridblocks by using only 5 gridblocks only. As mentioned earlier that the vertical grid has a definite effect on the pressure response for limited-entry vertical wells. Hence, for the limited-entry well case, there is a considerable improvement as can be seen in **Figure 5.26** for buildup, **Figure 5.27** for drawdown and **Figure 5.25** for the entire flow rate history. However, pressure derivatives do not improve at all for the other two cases where the well is either fully open to all layers or producing from top and bottom layers only. Similar pressure derivative responses in all figures presented in this application are already discussed in other applications as well as in the verification cases.

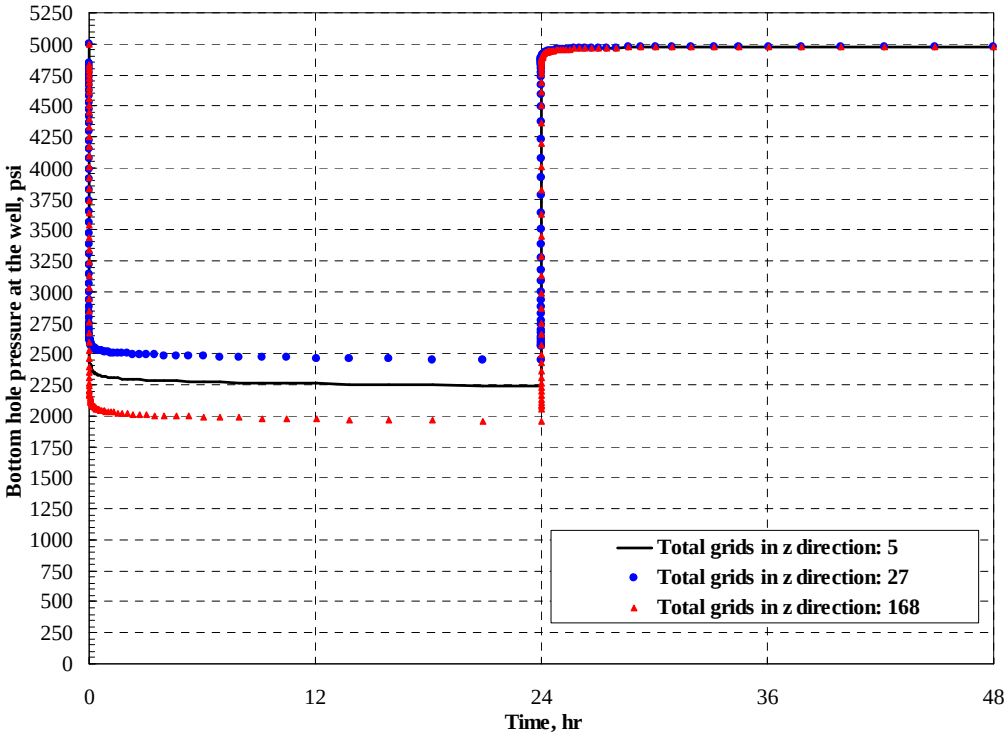

Figure 5.25 : Pressures for the entire flow rate history, limited-entry case.

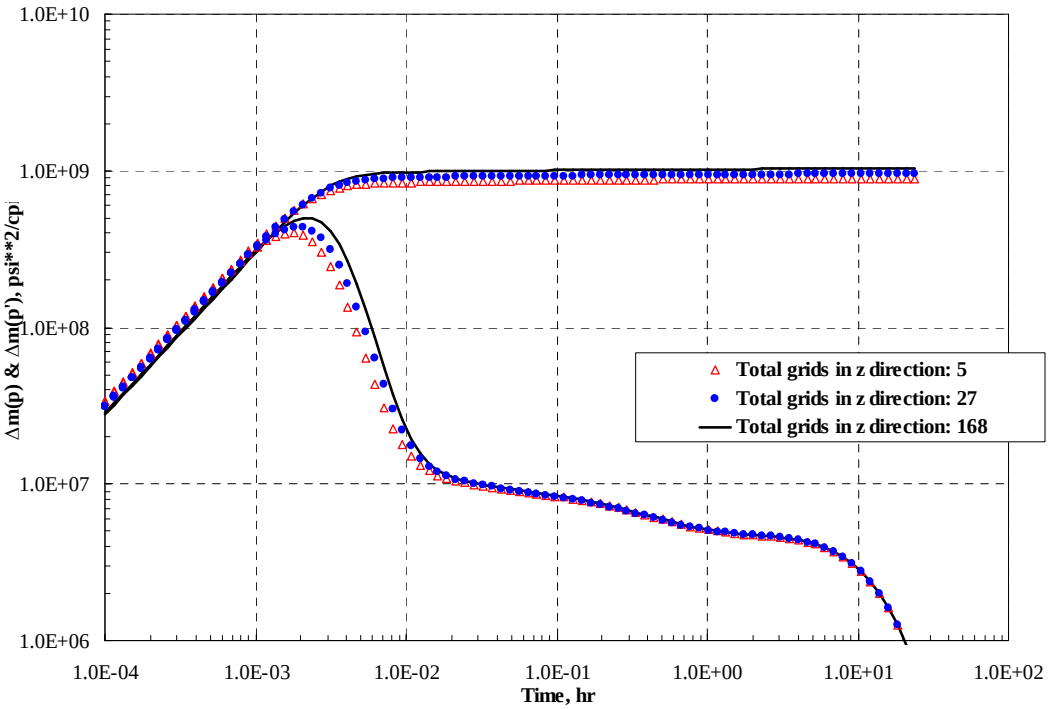

Figure 5.26 : Comparison of results, BU, limited-entry case in multi-layers test.

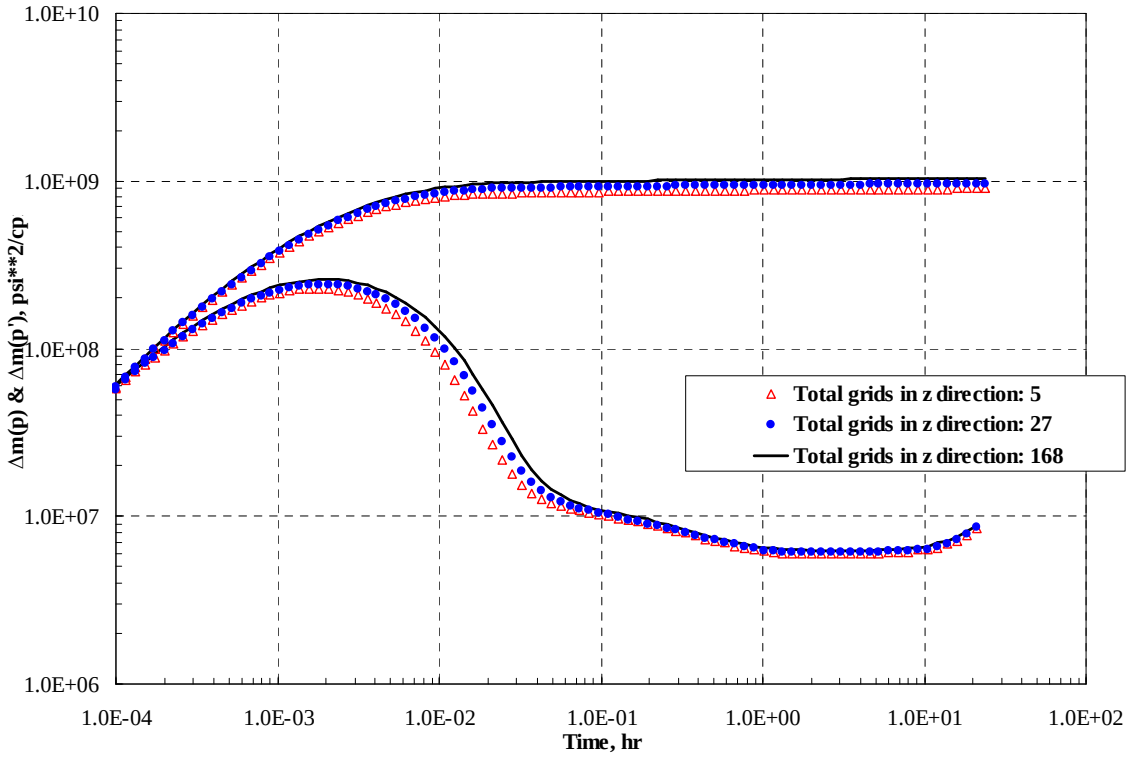

Figure 5.27 : Comparison of results, DD, limited-entry case in multi-layers test.

Figure 5.26 and **Figure 5.27** show the comparison of the pressure change and its Bourdet's derivative solutions for both drawdown and buildup periods respectively obtained from the fully penetrated and partially penetrated cases of multi-layers test application with different amount of gridblocks usage described earlier. As mentioned earlier in this application, logarithmic refinement on vertical axis does not help to improve solutions at all for pressure derivative solutions. However, there is considerable pressure difference between two cases as shown in **Figure 5.28** and **Figure 5.29** although derivatives look identical to each other as shown in **Figure 5.30**, **Figure 5.31**, **Figure 5.32** and **Figure 5.33**. Maximum pressure differences between the cases where maximum gridblock with logarithmic refinement used and the minimum gridblock used are tabulated in Table 5.4 at the end of production period where we expect highest different if exists.

Pressure responses for the entire flow rate history with the maximum amount of gridblocks used in vertical direction as 168 in all cases plotted in **Figure 5.34**. Thus, although the well is producing with less amount of flow rate in the limited-entry case, pressure drop in the wellbore is significantly drops compared to other two cases. Hence, this shows the importance of completion of a well prior to design the surface production facilities.

Table 5.4 : Pressures at end of production for case #1 & #2 for multi-layers test.

Cases	5 grids used	27 grids used	168 grids used
Fully penetration	3049.050	3050.38	3023.96
Partially penetration	3025.691	3028.75	3001.44

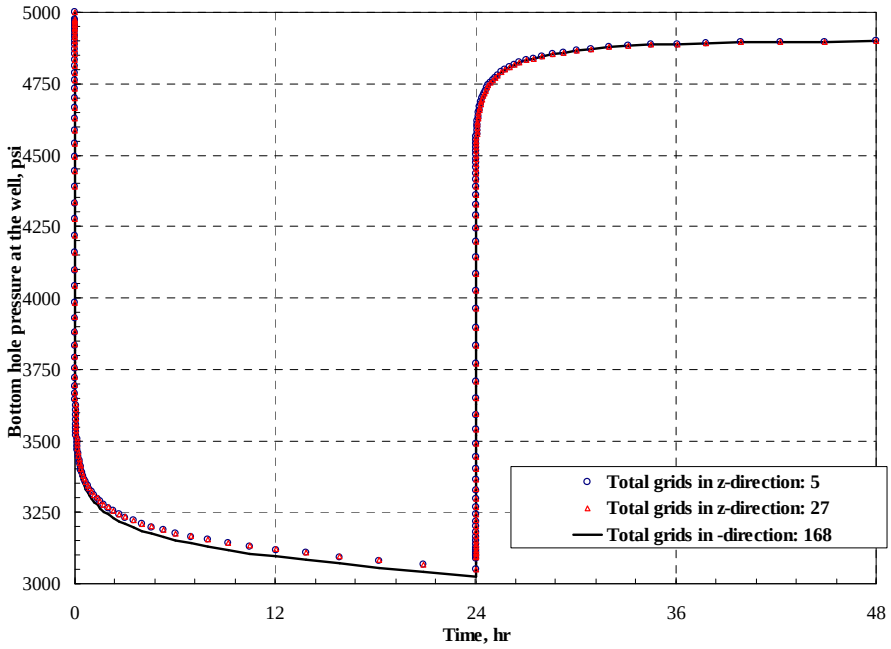

Figure 5.28 : Pressures for the entire flow rate history, fully penetrated case.

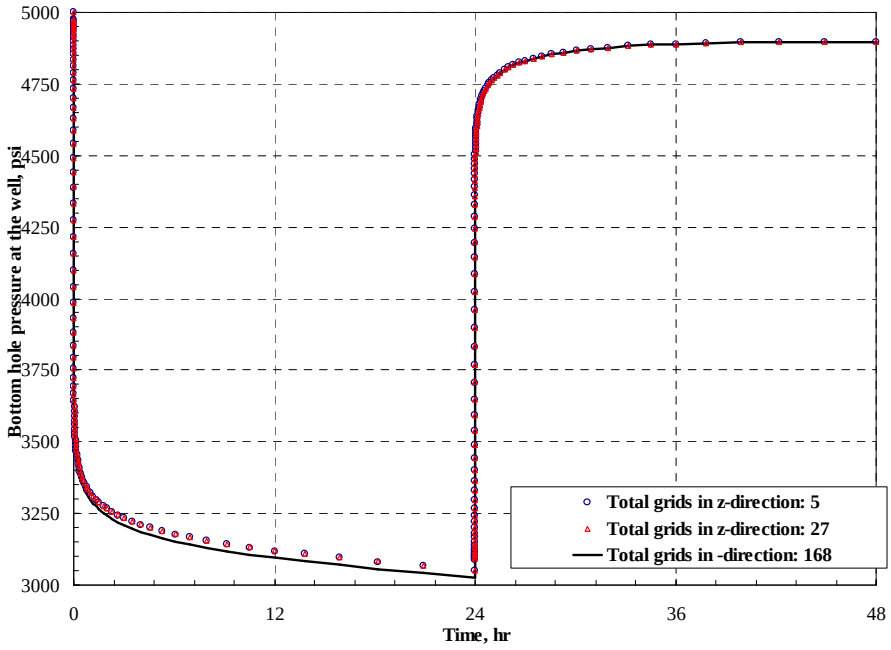

Figure 5.29 : Pressures for the entire flow rate history, partially penetrated case.

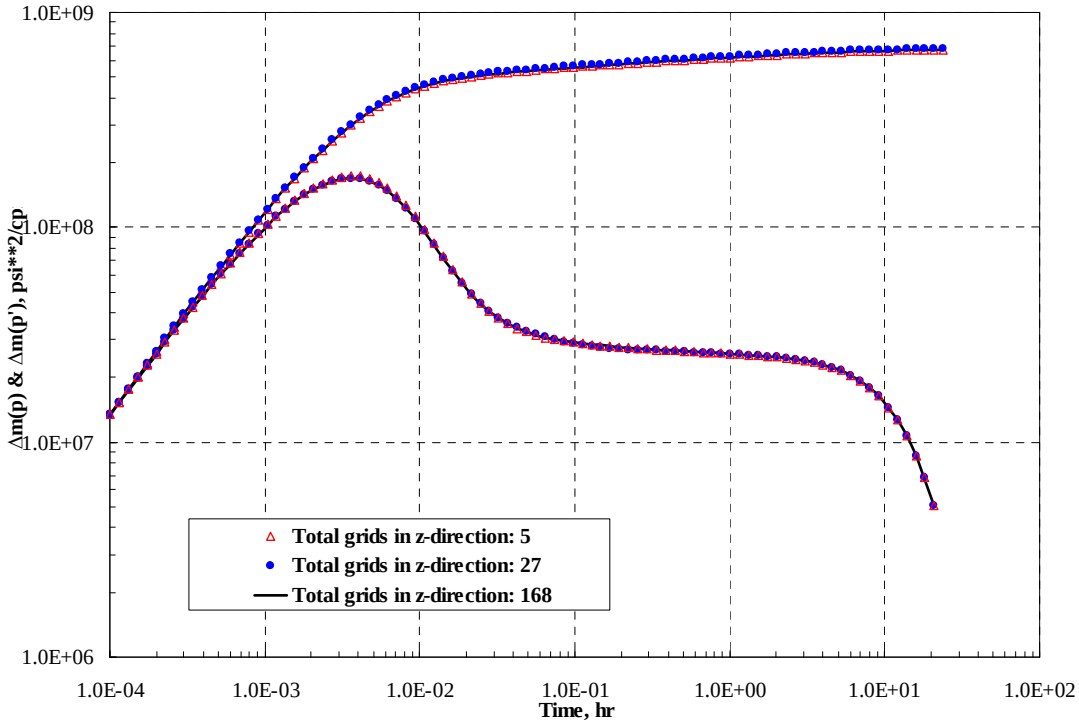

Figure 5.30 : Comparison of results, BU, fully penetrated case.

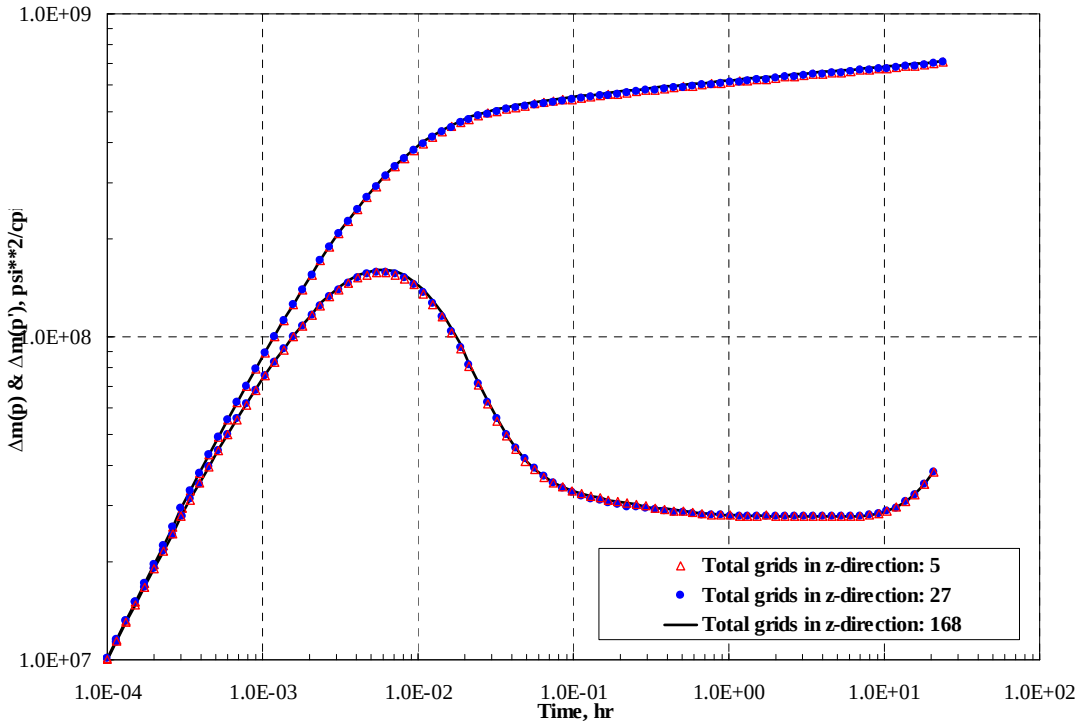

Figure 5.31 : Comparison of results, DD, fully penetrated case.

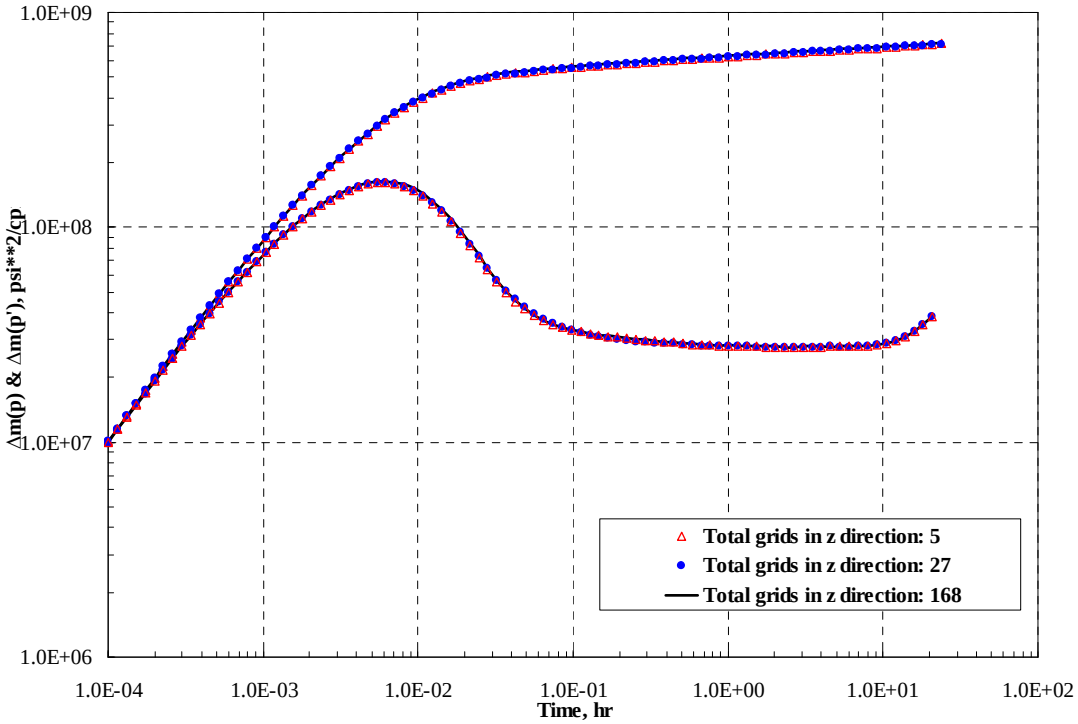

Figure 5.32 : Comparison of results, DD, partially penetrated from top and bottom.

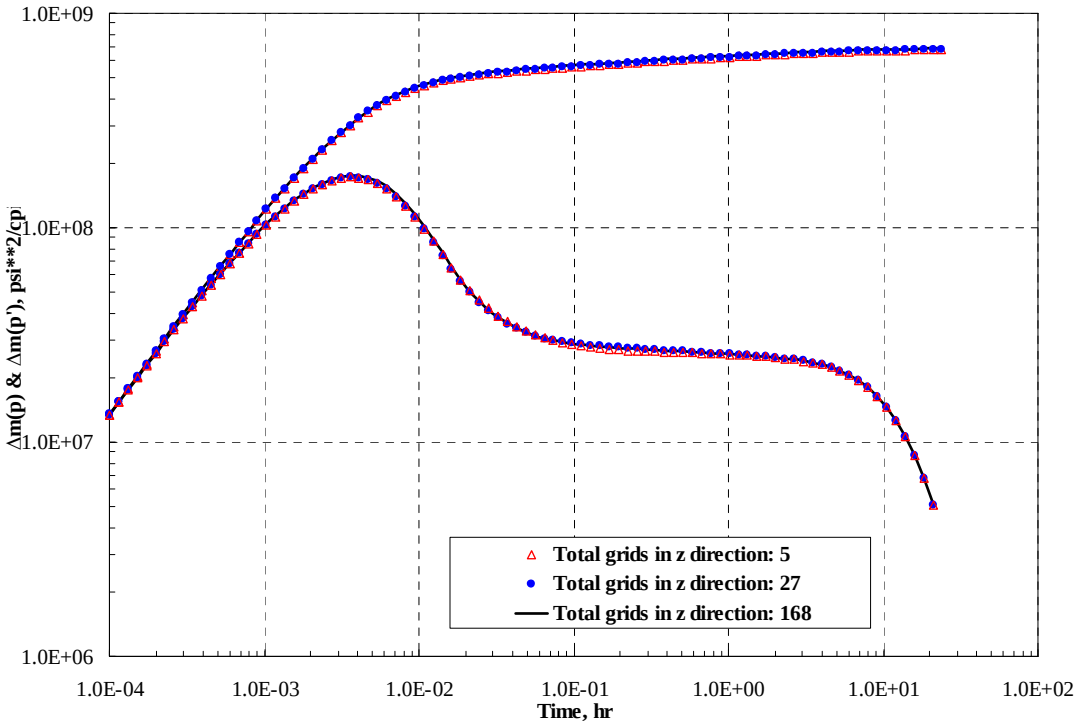

Figure 5.33 : Comparison of results, BU, partially penetrated from top and bottom.

The pressure distributions are also provided for the system in vertical axis at early times and late times for the entire flow rate history in **Figure 5.35**. Color scale is the similar with the one discussed earlier in **Figure 5.20** whereas the highest pressure is

taken constant in this case which is equal to the reservoir initial pressure in order to see the effects of buildup more clear in the screenshots.

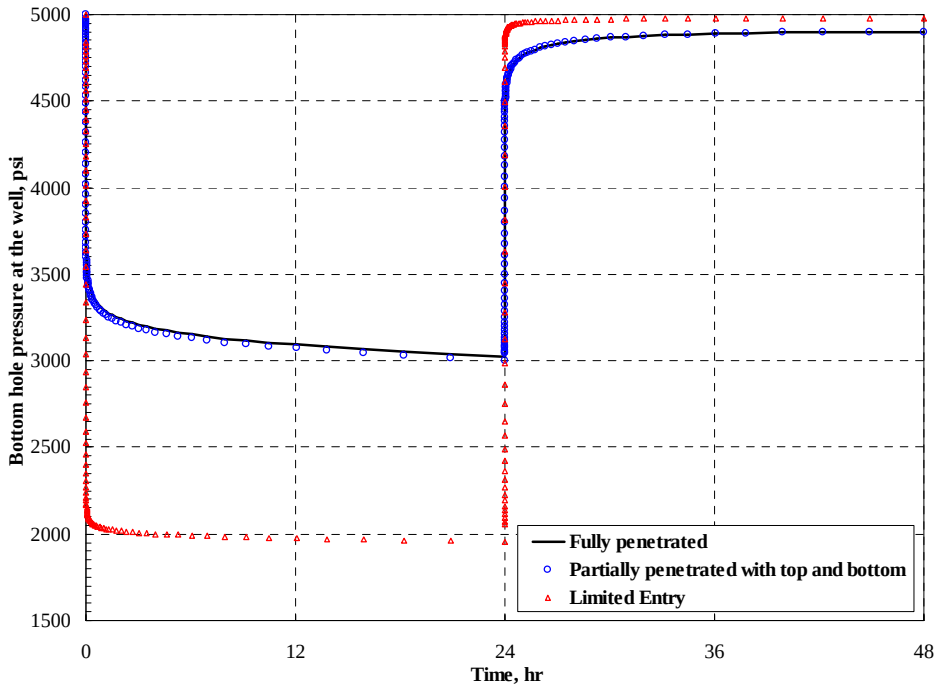

Figure 5.34 : Comparison of pressures in all cases for the entire flow rate history.

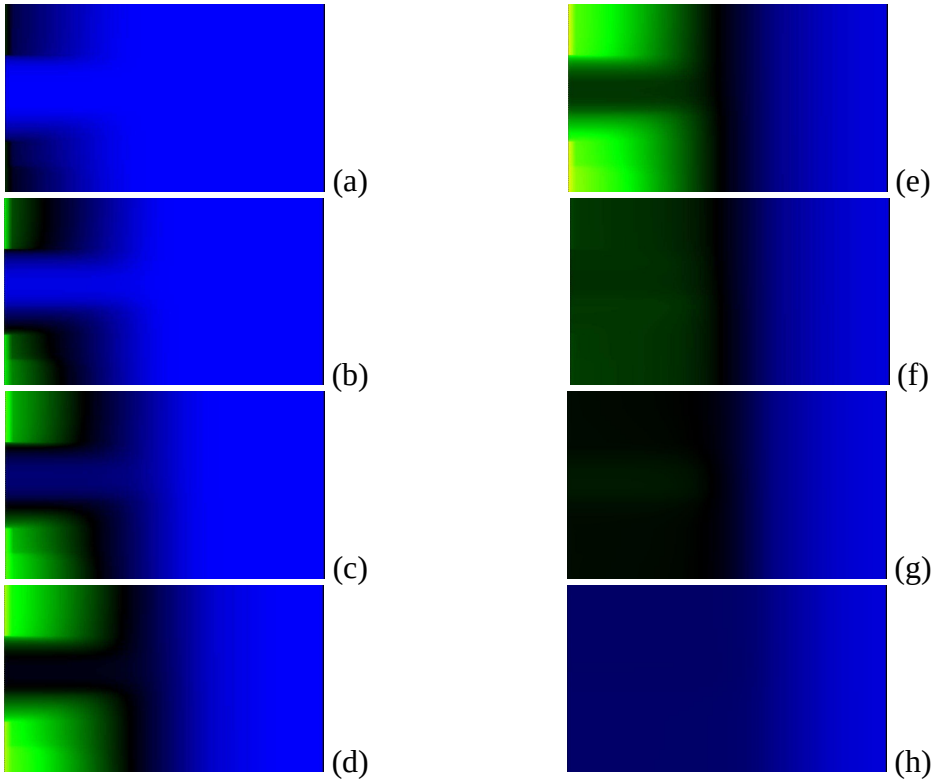

Figure 5.35 : Screenshots of pressure distributions from GUI of simulator, partially penetrated from top and bottom case in multi-layers test.

5.4 Determination of Non-Darcy Flow Region

This application is designed to give a different approach to the calculation of the non-Darcy flow effects and it can be applied to all cases described. Specifically, a non-Darcy flow region (similar to a skin region described by Hawkins) is intended to be represented as a zone (adjacent to the producing interval) of altered beta term in the correction factor (δ) of finite difference equations for non-Darcy flow effects. It is believed that non-Darcy flow effects no longer exists after a such distance which can not be calculated since no such formulation in literature exists but can be approximated by plotting the pressure solutions (with and without non-Darcy flow effects) of all gridblocks versus the corresponding exact locations throughout the reservoir at a specific given time of (usually in the middle of) each flow regime that occurs during the simulation. Only after that, a distance which commonly occurs in each flow regime at the same time point can be observed and approximated by length to represent as the radius of the non-Darcy flow region. Such distance can be well-used in the Eq. 5.1 and Eq. 5.2 to do a better estimation of the non-Darcy flow coefficient, *D*, which is a constant value and usually calculated by a non-linear regression software in the result of well test data interpretation.

Another approximation to calculate *D* is also introduced in Eq. 2.93 and it is well-used in the literature. Therefore, in order to calculate *D*, the comparison of two techniques from Eq. 5.1 or Eq. 5.2, and Eq. 2.93 and also Eq. 2.94 (in the case of multiple production) and finally approximated value from non-linear regression is discussed in this application along with the the absence of skin effects which would dominate the flow regime represented by the pressure derivative when exists with non-Darcy flow effects. The basic input model parameters for this example application are given in Table 5.5. The well is producing from a fully penetrated single-layer homogeneous and isotropic reservoir. Since non-Darcy flow effects are investigated in *r*-direction, only 1 gridblock is used in *z*-direction whereas 1000 gridblocks are used in the *r*-direction for this example application. The test sequence is shown in **Figure 5.36** where the well is produced at a constant rate of 20000 MSCF/D for 1000 hours, and shut in for 1000 hours for buildup.

Table 5.5 : Input parameters for non-Darcy flow region test.

Parameters	Values
r_w (ft)	0.3
r_e (ft)	5000
h (ft)	30
p_i (psi)	5000
T (^{o}F)	212
Gas gravity	0.7
$k_r = k_z$ (mD)	30
C (bbl/psi)	0.01
c_r (psi^{-1})	3.0×10^{-6}
ϕ (fraction)	0.1

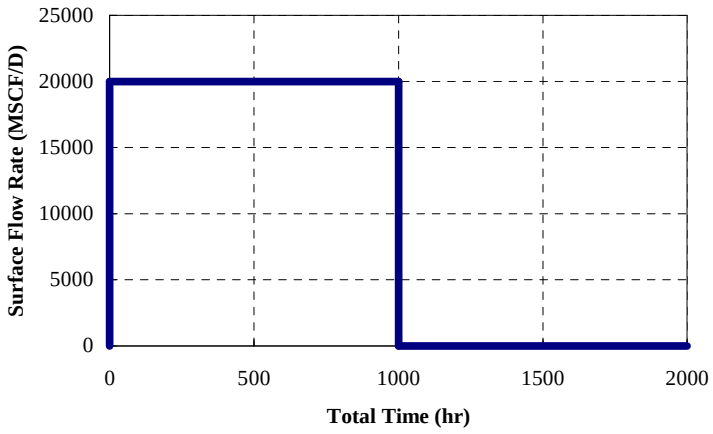

Figure 5.36 : Flow rate history at tested well for non-Darcy region test.

Pressure responses for the entire flow rate history is plotted in **Figure 5.39** while **Figure 5.37** and **Figure 5.38** show the comparison of the pressure change and its Bourdet's derivative solutions for drawdown and buildup periods respectively with non-Darcy flow effects and without non-Darcy flow effects in order to identify flow regimes and select one specific time corresponding to each of them.

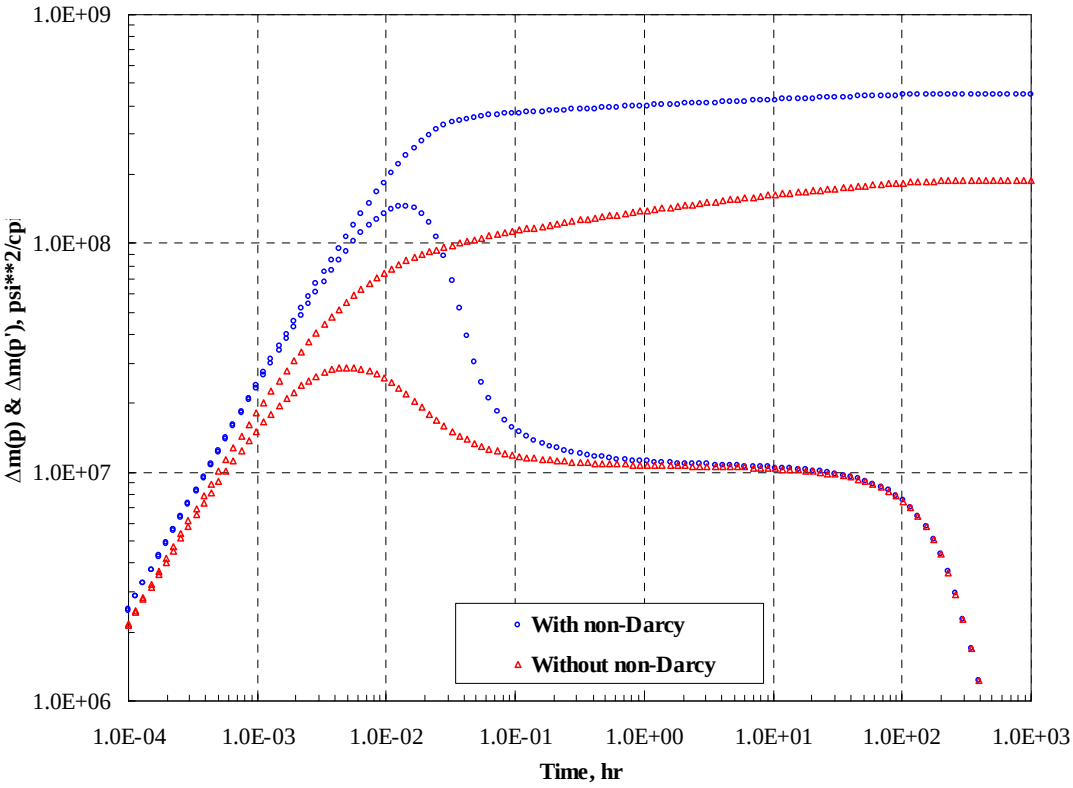

Figure 5.37 : Comparison of results, BU, non-Darcy flow region test.

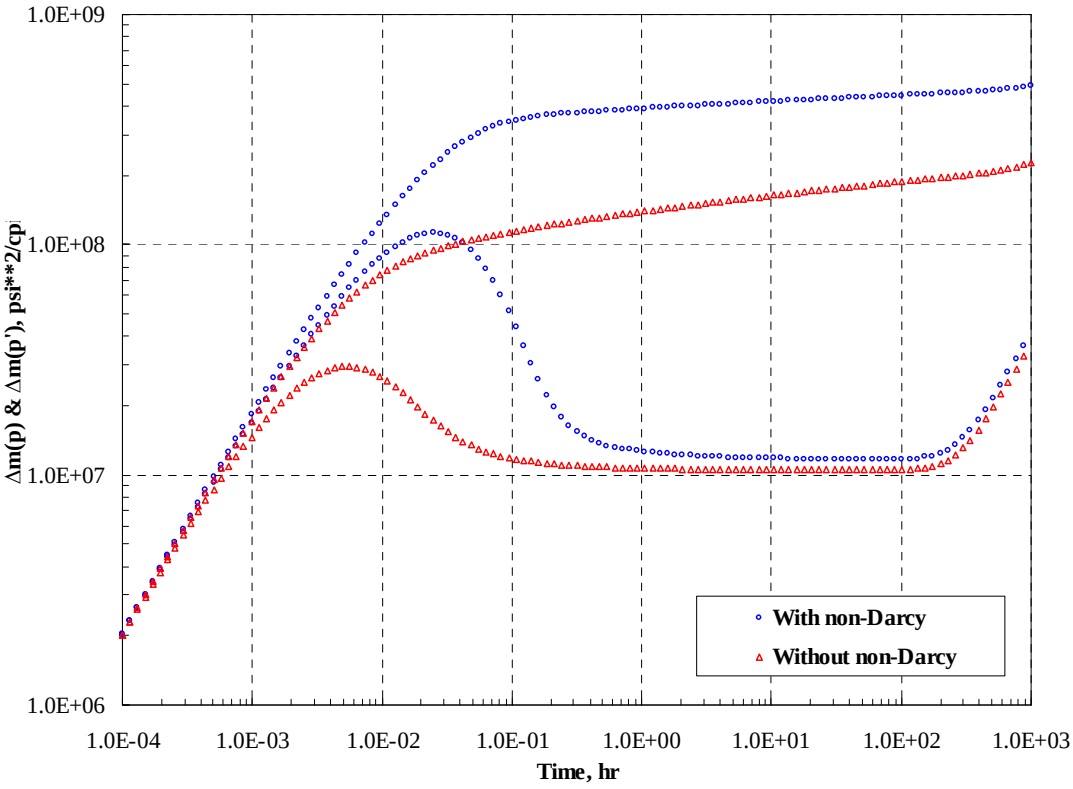

Figure 5.38 : Comparison of results, DD, non-Darcy flow region test.

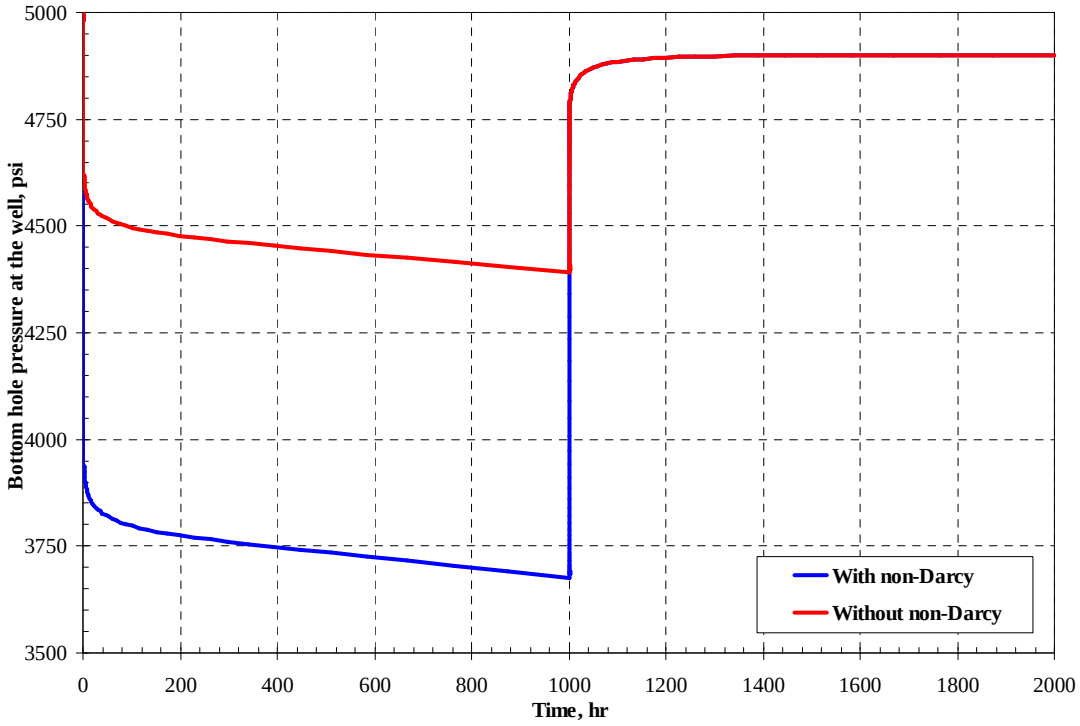

Figure 5.39 : Comparison of pressures for the entire flow rate history.

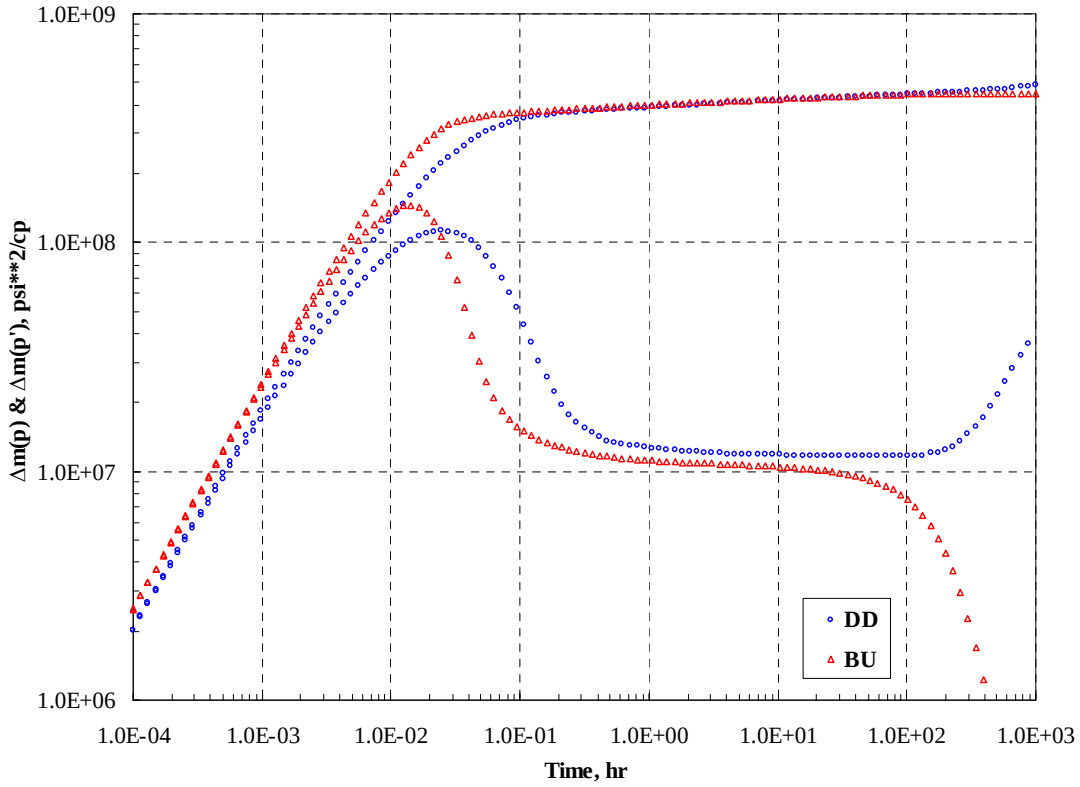

Figure 5.40 : Comparison of results, DD and BU, with non-Darcy flow effects.

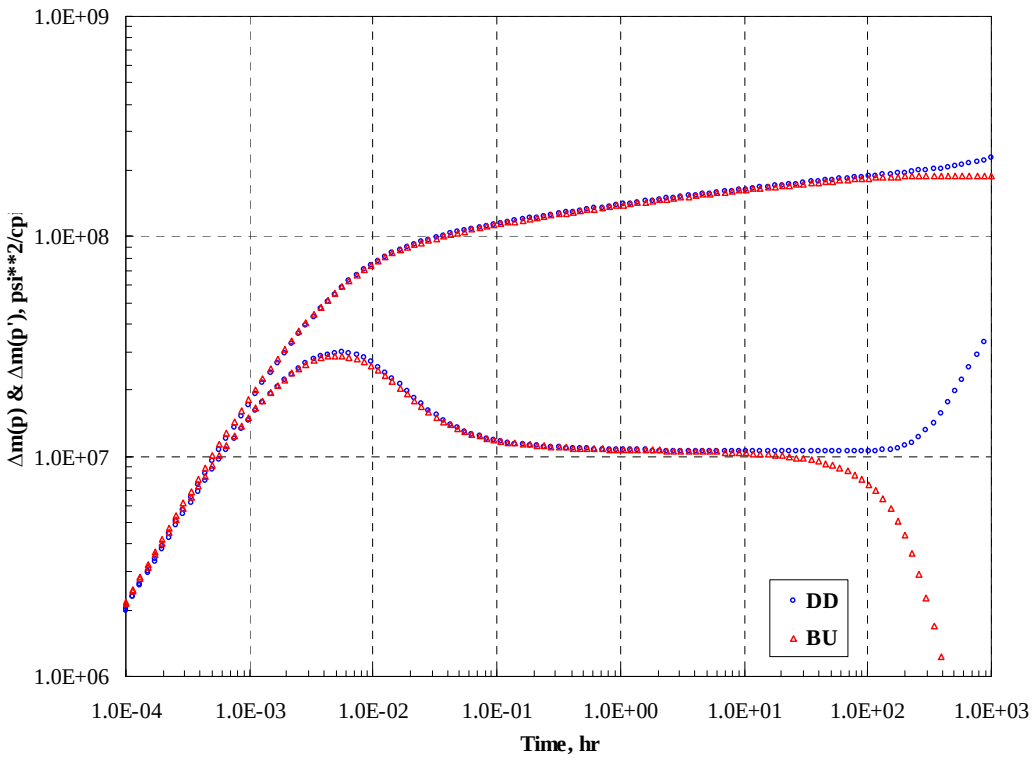

Figure 5.41 : Comparison of results, DD and BU, without non-Darcy flow effects.

We also compare the buildup and drawdown log-log plots of real gas pseudo pressures and its Bourdet's derivatives with non-Darcy flow effects. This comparison is shown in **Figure 5.40**. It is clear that the drawdown and buildup responses are not exactly overlay, mainly due to different change of compressibilities with decreasing (during DD) and increasing (during BU) pressures. On the other hand, a comparison of DD and BU responses without non-Darcy (**Figure 5.41**) indicates that when there is no non-Darcy flow effects, the BU and DD responses during radial flow (zero slope line on derivative data) are identical.

Next, we investigate the effect of non-Darcy flow inside the reservoir. It should be noted that there are three flow regimes which are wellbore storage dominated, radial flow and pseudo-steady state flow occurs respectively in this example application. As mentioned earlier, at least one time point is selected from each flow regime for both buildup and drawdown periods and plotted all gridblock centered locations versus corresponding pressure values calculated at the corresponding time for both with non-Darcy flow effects and without non-Darcy flow effects in **Figure 5.42** and in **Figure 5.43**. As can be seen from the figure, approximately around 100 ft, both pressure solutions for each specific time selected earlier almost becomes equal.

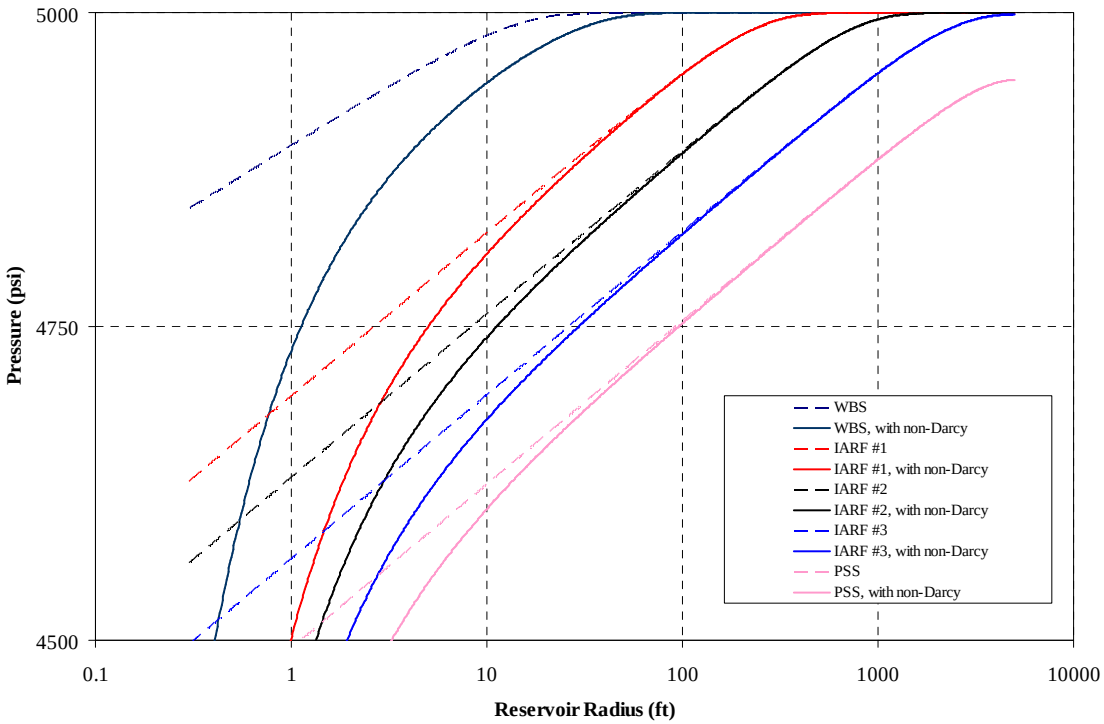

Figure 5.42 : Investigation of non-Darcy flow region, DD.

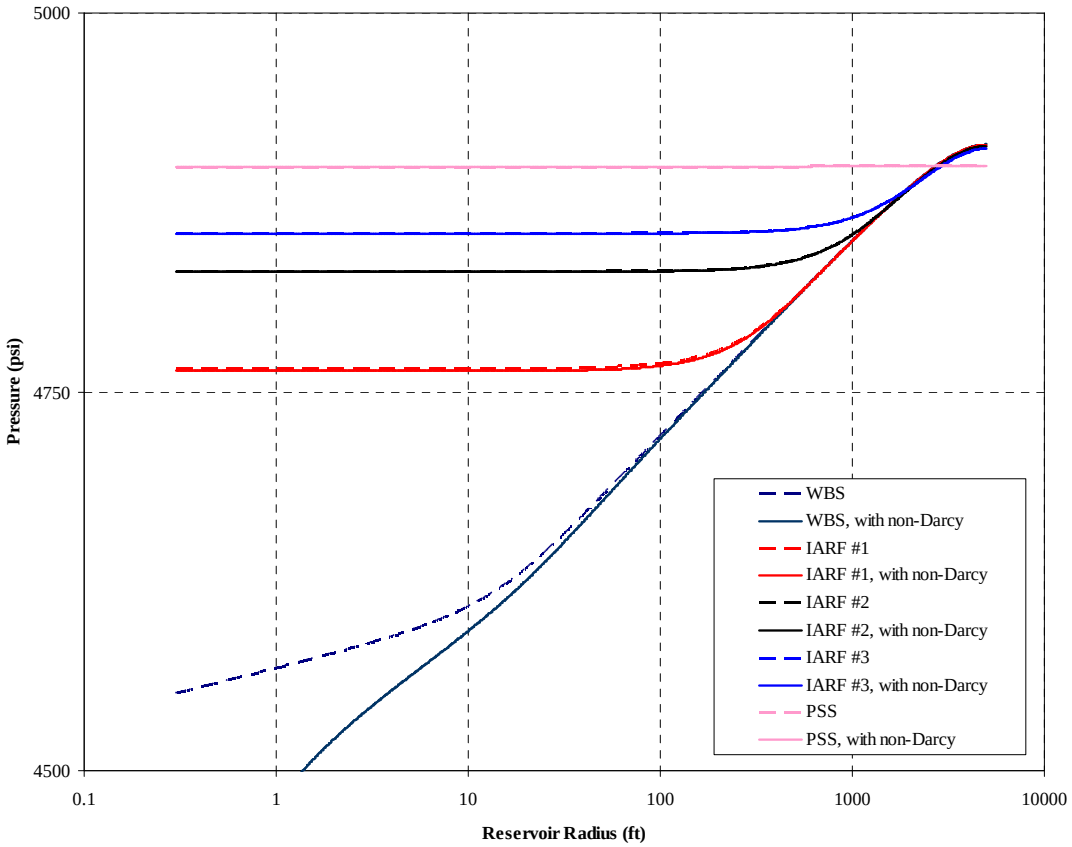

Figure 5.43 : Investigation of non-Darcy flow region, BU.

From both plots, non-Darcy flow region may not be represented exactly. Therefore, further investigation is performed in order to see the effect of the size of non-Darcy flow region and also to validate it. Here, r_n denotes the radius of the non-Darcy flow region; that is, non-Darcy flow occurs only in the region $r_w < r < r_n$. We would like to run our simulator by assigning a value of β for the region $r_w < r < r_n$ and setting $\beta_r = 0$ for $r > r_n$. Note that results are obtained from infinite acting radial flow region. With this regards, as also mentioned earlier, we would like to find such a non-Darcy region, r_n to obtain the same solution with when $r_n = r_e$ (i.e., without any definition of non-Darcy region). Certainly, such a radius for non-Darcy region never exists since pressure solutions in each gridblock uses non-Darcy flow terms and can not equal to the case when non-Darcy flow terms are negligible for the corresponding gridblocks. Therefore, we would like to calculate the relative difference between the pressure solutions in each time step point for a chosen value of r_n and when $r_n = r_e$. After non-Darcy flow region is approximated, Eq. 5.2 should be used to calculate *D* in which the viscosity term evaluation at which pressure becomes another issue. Ding discussed how to evaluate viscosity in detail, however, we provide in Table 5.2 calculation of *D* only when viscosity is taken as constant either at the initial condition or at the end of production period where it's expected to be the lowest flowing pressure during drawdown.

$$D = 2.223\times10^{-15}\ \frac{k_r\gamma_g}{\mu h}\ \left[\beta_r\left(\frac{1}{r_w}-\frac{1}{r_n}\right)\right] \qquad \textbf{(5.1)}$$

Eq. 5.2 is modified in the presence of skin effects as:

$$D = 2.223\times10^{-15}\ \frac{k_r\gamma_g}{\mu h}\ \left[\beta_s\left(\frac{1}{r_w}-\frac{1}{r_s}\right)+\beta_r\left(\frac{1}{r_s}-\frac{1}{r_n}\right)\right] \qquad \textbf{(5.2)}$$

where β_s is the calculation of beta term while considering altered permeability after Hawkins method applied to the permeability distribution of the skin zone.

Table 5.6 : Investigation of non-Darcy flow region.

Gridblock number in the *r*-direction considered for r_n	Exact location of the gridblock (ft)	Maximum relative difference (%)	Lowest flowing pressure at the tested well (psi)	*D* (when viscosity evaluated at lowest flowing pressure)	*D* (when viscosity evaluated at initial pressure)
50	0.480706	**12.4057**	4133	2.31E-04	2.07E-04
100	0.781577	**7.7338**	3962	3.88E-04	3.39E-04
200	2.066125	**2.9543**	3786	5.53E-04	4.71E-04
300	5.46187	**1.1152**	3718	6.17E-04	5.21E-04
400	14.43864	**0.4177**	3693	6.42E-04	5.39E-04
500	38.16903	**0.1547**	3683	6.51E-04	5.47E-04
600	100.9011	**0.0565**	3679	6.55E-04	5.49E-04
700	266.7355	**0.0188**	3678	6.56E-04	5.50E-04
750	433.6839	**0.0102**	3678	6.56E-04	5.51E-04
800	705.1244	**0.0051**	3677	6.57E-04	5.51E-04

Pressure solutions at the tested well are shown in **Figure 5.44**. As can be seen, after 600 gridblocks (100.9011 ft) pressure solutions become almost identical where the maximum relative difference can be read from Table 5.5 as 0.0565%. Note that from **Figure 5.42** and **Figure 5.43**, a distance close to 100 ft was observed as well. We would like to show another fact when non-Darcy flow region is considered at the calculations, that is non-Darcy flow region changes with respect to time. Let's continue with our assumption in this example application for non-Darcy flow region which is 100.9011 ft. We would like to take the maximum relative difference which is read from Table 5.5 earlier and calculate for each time step point for the entire flow rate history, the difference between the solutions when non-Darcy flow effects exist and when non-Darcy flow effects do not exist throughout the reservoir. When the difference which we calculate continuously for a time step point is less than our maximum relative difference, we will consider that distance as the corresponding non-Darcy flow region for that specific time step point and plot for the entire flow rate history as shown in **Figure 5.45**.

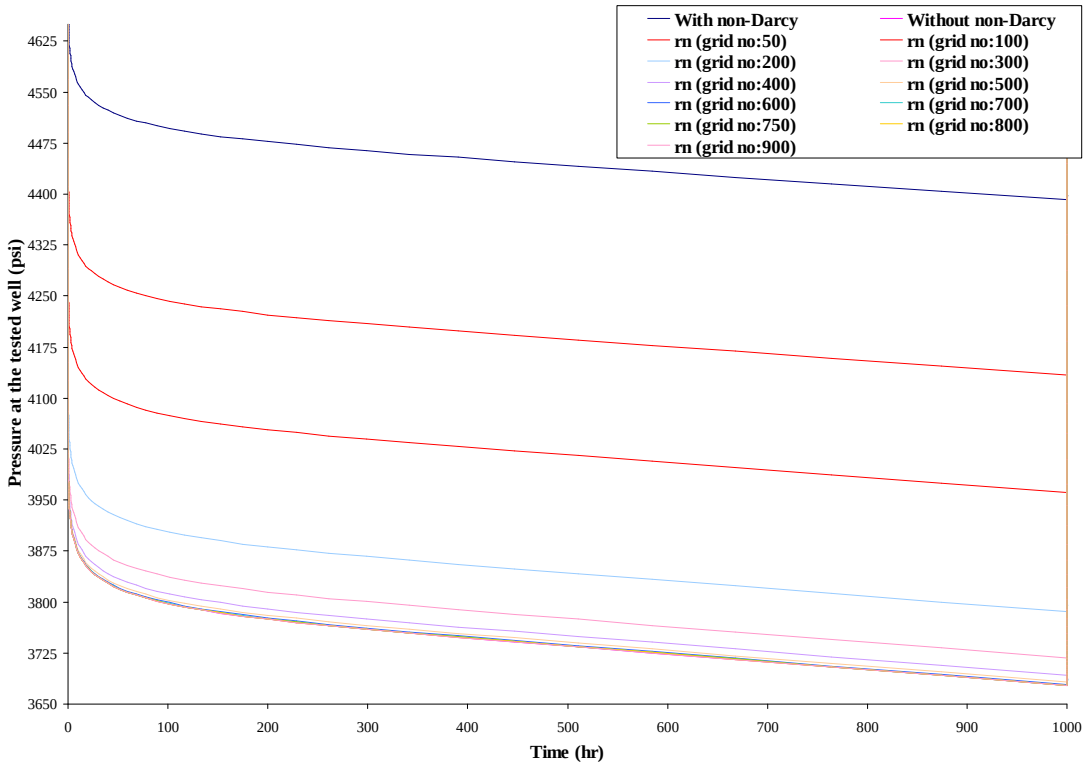

Figure 5.44 : Pressures at the tested well, DD, for different non-Darcy flow regions.

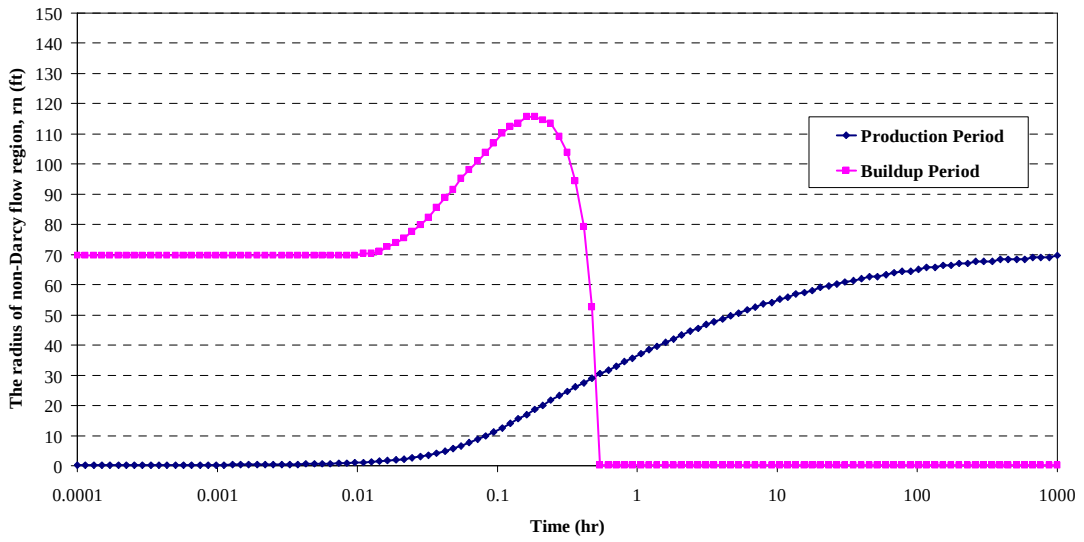

Figure 5.45 : Non-Darcy flow region for the entire flow rate history vs. time.

Figure 5.45 shows the change in non-Darcy flow region when we select our maximum difference between solutions with non-Darcy and without non-Darcy flow effects in each time step point is around %0.05. Further investigations on this graph need to be studied. However, for our interest, we can still prove our conclusions as non-Darcy flow region is not easy to calculate since there should be several different simulations need to done for the same model. Even if it's believed to be assumed

good enough, non-Darcy flow region will change with respect to time as shown in **Figure 5.45**. However, a good estimate of non-Darcy flow region for this application does not misrepresent non-Darcy flow coefficient which is approximated in the data interpretation software (ECRIN) as D=5.83×10^{-4} *MSCF/D*$^{-1}$. We also calculated non-Darcy flow coefficient from well-known equation in literature (Eq. 2.93) and found as D=5.5×10^{-4} *MSCF/D*$^{-1}$ when initial condition is considered for calculation of viscosity since it provided better results during the comparison of all method solutions with each other. Although we provided three different calculations for non-Darcy flow coefficient in Table 5.7, we would recommend choosing the approach based on multirate transient drawdown tests when it is applicable.

Table 5.7 : Comparison of results for non-Darcy flow coefficient.

	Non-Darcy flow coefficient, D, *MSCF/D*$^{-1}$
ECRIN	5.83×10^{-4}
Non-Darcy flow region method (r_n = 100.9 ft)	5.49×10^{-4}
Well known equation from literature (Eq. 2.93)	5.50×10^{-4}

Finally, we provide the plot in **Figure 5.46** in which the maximum difference in pressure solutions (on the left axis) between the case with non-Darcy and without non-Darcy for the entire flow rate history and calculated non-Darcy flow coefficient (on the right axis) versus non-Darcy flow region radius.

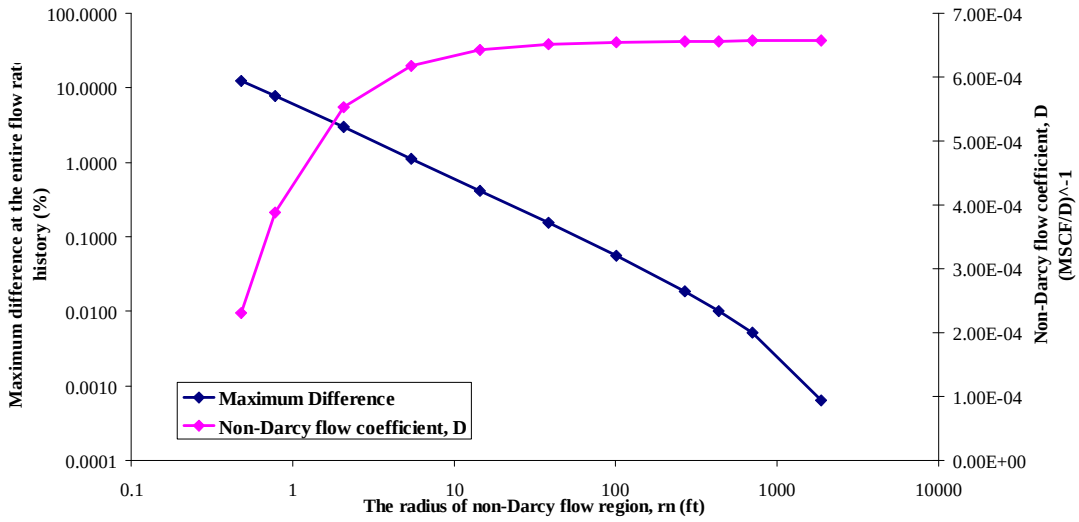

Figure 5.46 : Non-Darcy flow properties vs. time for entire flow rate history.

6. CONCLUSIONS AND RECOMMENDATIONS

A 2-D (*r*-*z*) numerical flow simulation package has been developed with following capabilities:

- Numerical flow simulation
- Graphical well test analysis output
- Graphical User Interface

Applying these techniques and the applications discussed in the study to various reservoir models with different flow rate histories is an excellent educational experience for petroleum engineers to have a better insight into how pressure transients move in a reservoir due to various parameters and multiple observation points in homogeneous reservoirs as well as heterogeneous.

Specific conclusions obtained from this can be summarized as:

- The functional iteration technique (FIT) and the NW technique give identical pressure responses.
- Selection of the time steps (especially the first time step) is critical to observe the early time behavior of pressure results in terms of accuracy.
- In limited-entry problems, logarithmic refinement is compulsory in order to have a correct solution.
- The number of grid blocks in the *r*-direction does not have a significant effect on the pressure solutions unless it is not less than sufficient amount of gridblocks (i.e., 25)
- YALE provides an excellent source for solving the symmetric and nonsymmetric sparse matrices arising from the nonlinear real-gas flow problem studied here. With Yale, we are able to simulate a grid system with as high as 250,000 grid blocks in total. Although the iterative SSIP method provides solutions for larger than 250,000 grid blocks, but it is quite slower. For the same size problems, Yale is computationally superior.

There are numerous conclusions and concerns stated under each verification and application cases which may be used for more advanced studies on some recommendations outlined below as:

- Simulator may be improved further to obtain pressure solutions for three dimensional problems by adding the flow in the theta (θ) direction. In such case, packer-probe and probe-probe IPTT tests (see Kuchuk et al. 2010 for details) would be modeled entirely.
- In addition to the discussion about non-Darcy flow effects, it would be further investigated to account in consideration of viscosity term in the non-Darcy flow coefficient terms (Eq. 2.93 and Eq. 5.1 or Eq. 5.2).
- Non-Darcy flow effects on *z*-direction would be investigated especially in the case of limited-entry wells.
- Since simulator seems to be working fine in all cases, history matching problems would be studied.
- Heterogeneity would be modeled in *r*-*z* cylindrical reservoirs and investigate the pressure propagations throughout the reservoir.

REFERENCES

Aziz, K., and Settari, A. (1979). *Petroleum Reservoir Simulation*. Applied Science Publ., Wilmmette, IL.

Bratvold, R. B. (1984). A Simulation Study of Gas Wells Under Radial Flow Conditions, *M.S. Thesis*, the University of Tulsa, Tulsa, OK.

Bilhartz, H. L. Jr., and Ramey, H. J. Jr. (1977). The Combined Effects of Storage, Skin, and Partial Penetration on Well Test Analysis. *SPE Annual Technical Conference and Exhibition*, Denver, USA, October 9-12.

Bourdet, D., Ayoub, J. A., and Pirard, Y. M. (1989). Use of Pressure Derivative in Well Test Interpretation. *SPE Form. Eval.*, **4** (2), 293–302; *Trans.*, AIME, **287**.

Dalton R., and Mattax, C. (1990). *Reservoir Simulation Monography Vol. 13*. SPE Henry L. Doherty Series, Richardson, Texas, USA., p.p. 1-5, 133-139.

Ding, W. (1984). Gas Well Test Analysis, *M.S. Thesis*, the University of Tulsa, Tulsa, OK.

Ecrin v4.12.02 (2009). Integrated Software Platform for Dynamic Flow Analysis, Sophia Antipolis, France: Kappa Engineering.

Eisenstat, S. C., Gursky, M. C., Schultz, M. H., and Sherman, A. H. (1979). Yale Sparse Matrix Package I, The symmetric Codes. Yale University, Department of Computer Science, Technical Report #112.

Eisenstat, S. C., Gursky, M. C., Schultz, M. H., and Sherman, A. H. (1979). Yale Sparse Matrix Package II, The Nonsymmetric Codes. Yale University, Department of Computer Science, Technical Report #114.

Ertekin, T., Abou-Kassem, J. H., and King, G. R. (2001). *Basic Applied Reservoir Simulation*. Richardson, TX.

Esmail, M. N. (1985). Problems In Numerical Simulation Of Heavy Oil Reservoirs. *Journal of Canadian Petroleum Technology*, Volume 24, Number 3, May-Jun.

Forchheimer, P. (1781). Wasserbewegung durch Boden, Zeitz. Ver. Deutch Ing., Berlin (1901) 45.

Hawkins, M. F. Jr. (1956). A note on the Skin Effect. *SPE Technical Note*, December.

Horne, R. N, and Kuchuk, F. (1988). Use of Simultaneous Flow-Rate and Pressure Measurements To Replace Isochronal Gas Well Tests. *SPE Formation Evaluation*, Volume 3, Number 2.

Kabir, C.S. (2006). What is the Real Measure of Gas Well Deliverability? *SPEREE*, April, pp. 126-134; SPE-84469-PA.

Kuchuk, F. J., Onur, M., and Hollaender, F. (2010). *Pressure Transient Formation and Well Testing: Convolution, Deconvolution and Nonlinear Estimation*. No. 57, Amsterdam, Developments in Petroleum Science, Elsevier.

Onur, M. (1997). *Simulation of Geosystems*. PET428E Course Notes, ITU, Faculty of Mines, Petroleum and Natural Gas Engineering, Istanbul, Turkey.

Tureyen, O.I., Satman, A., and Onur, M. (2000). Determination of Formation Properties From Stabilized and Unstabilized Gas-Well-Test Data. *SPE Annual Technical Conference and Exhibition*, Dallas, Texas, 1–4 October.

Wattanberger, R. A., and Ramey, H. J. Jr. (1968). Gas Well Testing With Turbulence, Damage and Wellbore Storge. *JPT*, August, 887.

APPENDICES

APPENDIX A : Real Gas Properties
APPENDIX B : Derivative terms

APPENDIX A

Real gas properties are changed by pressure and temperature such as compressibility, gas deviation factor and viscosity. In this study, isothermal temperature case is considered only. Therefore, definition of the compressibility, c_g is given by:

$$c_g = -\frac{1}{V}\left(\frac{\partial V}{\partial p}\right)_T = -\frac{1}{B}\left(\frac{\partial B}{\partial p}\right)_T = \frac{1}{\rho}\left(\frac{\partial \rho}{\partial p}\right)_T \quad \textbf{(A.1)}$$

For a real gas, the equation of state (EOS) defined as:

$$PV = ZnRT \quad \textbf{(A.2)}$$

Here Z is the gas deviation factor, if we combine Eq. A.1, the derivative of Eq. 1.1 with respect to pressure at constant temperature, and Eq. A.2; we can express the compressibility of gas in terms of the gas deviation factor as:

$$c_g = \frac{1}{p} - \frac{1}{Z}\left(\frac{\partial Z}{\partial p}\right)_T \quad \textbf{(A.3)}$$

There are numerous correlations expressed in the literature to determine the gas viscosity which depends on the pressure. In this study, we used Lee et al. correlations to find viscosity. The correlation is:

$$\mu = K\ e^{\left(X\ \rho^{y}\right)} \quad \textbf{(A.4)}$$

where μ is in g/cm^3, M is the molecular weight, T is the temperature in ^oR and K, X and y are given by:

$$\begin{aligned} K &= \frac{10^{-4}\left(9.4 + 0.02M\right)T^{1.5}}{209 + 19M + T} \\ X &= 3.5 + \frac{986}{T} + 0.01M \\ y &= 2.4 - 0.2X \end{aligned} \quad \textbf{(A.5)}$$

APPENDIX B

1) Viscosity: Simulator uses Lee et al. correlation given by Eq. A.4, and its derivative is defined as:

$$\frac{\partial \mu}{\partial p} = \left(Ke^{X\rho^y} \right) \frac{\partial \left(X\rho^y \right)}{\partial p} = \left(Ke^{X\rho^y} \right) \left[\frac{\partial X}{\partial p} \rho^y + X \frac{\partial \rho^y}{\partial p} \right]. \\ = \left(Ke^{X\rho^y} \right) \left[Xy\rho^{y-1} \frac{\partial \rho}{\partial p} \right] \quad \textbf{(B.1)}$$

2) Formation Volume Factor:

$$\frac{\partial B}{\partial p} = \frac{p_{sc}}{T_{sc}} T \left[\frac{\partial Z}{\partial p} \frac{1}{p} - \frac{Z}{p^2} \right] \quad \textbf{(B.2)}$$

3) Density:

$$\frac{\partial \rho}{\partial p} = \frac{M}{RT} \left[\frac{1}{Z} - p \frac{1}{Z^2} \frac{\partial Z}{\partial p} \right] \quad \textbf{(B.3)}$$

4) Gas Compressibility:

$$\frac{\partial c_g}{\partial p} = -\left[-\frac{1}{B^2} \frac{\partial B}{\partial p} \left(\frac{\partial B}{\partial p} \right) + \frac{1}{B} \frac{\partial \left(\frac{\partial B}{\partial p} \right)}{\partial p} \right] \quad \textbf{(B.4)}$$

CURRICULUM VITAE

Name Surname: **Cihan Alan**

Place and Date of Birth: **Izmir, 1984**

Address: **ITU Ayazağa Kampüsü**

Maden Fakültesi Petrol Bölümü

Maslak / Istanbul

E-Mail: **calan @itu.edu.tr**

B.Sc.: **Petroleum Engineering**

Istanbul Technical University

Professional Experience and Rewards:

Schlumberger, Middle East experienced, Field Engineer for 3 years

SPE European Student Paper/Presentation Contest Undergraduate & Masters Division, 2006, Second Place Winner, Intelligent Energy (IE) Conference and Exhibition, Amsterdam, HOLLAND

Microsoft Certified Solution Developer (MCSD.NET), 2005

Microsoft Certified Application Developer (MCAD.NET), 2005

Microsoft Certified Professional (MCP), 2005